EFFECT OF PHASE TRANSFORMATION ON STRESS REDISTRIBUTION AND DAMAGE

EVOLUTION DURING ACTUATION FATIGUE IN SHAPE MEMORY ALLOYS

A Dissertation

by

FRANCIS RANDALL PHILLIPS

Submitted to the Office of Graduate and Professional Studies of
Texas A&M University
in partial fulfillment of the requirements for the degree of

DOCTOR OF PHILOSOPHY

Chair of Committee,	Dimitris C. Lagoudas
Committee Members,	Ibrahim Karaman
	Darren J. Hartl
	Amine Benzerga
Head of Department,	Rodney Bowersox

August 2018

Major Subject: Aerospace Engineering

ABSTRACT

Shape Memory Alloys (SMAs) are a unique type of metallic alloys which exhibit a reversible, crystallographic phase transformation between austenite and martensite. SMAs have found applications in a number of industries, including the biomedical, aerospace, and automotive industries. However most of these applications are either non-critical or the SMAs have been severely overdesigned. Part of the reason for these limitations is due to a lack of understanding in exactly how these materials change throughout their lifetime.

In this work, various aspects related to the change in SMA components are studied throughout their functional lifetime, both with respect to how the material changes within a single phase transformation cycle, as well as how the internal microstructure evolves throughout the entire lifetime of the SMA component. The first part of this work focuses on the effect of phase transformation within a single phase transformation cycle by considering the redistribution of stresses during phase transformation in notched cylindrical SMA bars under both pseudoelastic and thermal actuation loading paths. These notches are tailored to achieve stress concentrations of varying magnitude in order to see how different stress concentrations affect the phase transformation within a single phase transformation cycle. The results indicate that the size of the notches have a direct impact on the evolution of the phase transformation, changing from a linear propagation for shallow notches to a spherical propagation for sharp notches. Furthermore, for notch sizes in which both phase transformation propagation patterns exist, numerical results indicate that the stress redistribution may lead to phase transformation reversal. Experimental efforts show general agreement in terms of both surface level measurements as well as fracture surface analysis. In addition, neutron diffraction experiments provide an additional level of validation for the numerical results due to the ability to monitor the crystal structure of the experimental specimens during testing.

Beyond studying the effect of the phase transformation in a single cycle for a SMA with a stress concentration, it is also necessary to consider the effect of the phase transformation throughout the lifetime of a SMA actuator. In the second portion of this work, SMA actuators are analyzed using

X-Ray Computed MicroTomography in order to determine the evolution of internal damage as a function of actuation fatigue life. The data shows that the internal damage evolves in a non-linear manner, with a rapid nucleation of damage at the beginning of the fatigue life, followed by a slow growth until close to the end of life, when damage coalesces and starts to grow exponentially. The captured internal damage evolution behavior has been introduced into a SMA constitutive model and results are presented showing that the proposed internal damage accumulation model is able to capture the evolution of internal damage well throughout the fatigue lifetime, as well as predict the cycles to failure for a SMA actuator. Based on an understanding of how internal damage nucleates and grows throughout the actuation fatigue lifetime of a SMA component, it is in turn possible to link this damage growth back to stress concentrations and therefore utilize this knowledge to understand how stress will redistribute within each thermal actuation cycle for a SMA actuator.

DEDICATION

To my wife, Melissa, and children, William, Robert, Hannah, and Andrew

as making sure that all requirements needed to complete this work were satisfied was invaluable. I would also like to acknowledge Sherilyn Fields for her help in coordinating activities and calendars to ensure availability and enable communication. The help provided by Rodney Inmon has also been invaluable in running and collecting the experimental data.

Finally, I would like to acknowledge the help and support from my family. Coming back to school after working for five years is an uncommon career path, and I could not have done it without their support. To my wife, Melissa, thank you for believing in me and believing that we could do this. To my children, William, Robert, Hannah, and Andrew, thank you for this time and for understanding when I had to leave to go work. To my parents and extended family, thank you for helping to support me and my family during this time.

CONTRIBUTORS AND FUNDING SOURCES

Contributors

Funding Sources

NOMENCLATURE

TAMU	Texas A&M University
ORNL	Oak Ridge National Laboratory
SNS	Spallation Neutron Source
APS	Advanced Photon Source
ANL	Argonne National Laboratory
NOL	Naval Ordnance Laboratory
SMA	Shape Memory Alloy
X-Ray μCT	X-Ray Computed MicroTomography
SEM	Scanning Electron Microscope
SME	Shape Memory Effect
M_S	Martensite Start Temperature
M_F	Martensite Finish Temperature
A_S	Austenite Start Temperature
A_F	Austenite Finish Temperature
σ	Stress
M_S^σ	Martensite Start Temperature at stress level σ
M_F^σ	Martensite Finish Temperature σ
A_S^σ	Austenite Start Temperature σ
A_F^σ	Austenite Finish Temperature σ
TRIP	Transformation Induced Plasticity
ξ	Martensitic Volume Fraction

ξ_{min}	Minimum Martensitic Volume Fraction at a Point during Reverse Phase Transformation Prior to the Start of Forward Phase Transformation
a	Radius of Plane of Minimum Cross-Section
R	Radius of Notch
$\frac{a}{R}$	Notch Acuity Ratio
UMAT	User Material Subroutine
E_A	Elastic Modulus of Austenite
E_M	Elastic Modulus of Martensite
α_A	Coefficient of Thermal Expansion in Austenite
α_M	Coefficient of Thermal Expansion in Martensite
ν	Poisson Ratio
C_M	Stress Influence Coefficient for Martensite
C_A	Stress Influence Coefficient for Austenite
H_{min}	Minimum Transformation Strain
H_{sat}	Maximum Transformation Strain
$\bar{\sigma}_{crit}$	Critical von Mises Equivalent Stress Below Which $H^{cur} = H_{min}$
d	Internal Damage
DIC	Digital Image Correlation
η	Triaxiality Ratio
σ_H	Hydrostatic Stress
$\bar{\sigma}$	Equivalent Stress
VDRIVE	VULCAN Data Reduction and Interactive Visualization software for Event mode neutron diffraction
LVDT	Linear Variable Differential Transformer
d_{crit}	Critical Internal Damage Value at Failure

N_F	Number of Cycles at SMA Actuator Failure due to Actuation Fatigue
$\tilde{N}$	Percentage of Actuation Fatigue Lifetime
$\hat{\Phi}$	Actuation Work Density
C^d, γ_d	Fitting Parameters for Prediction of Actuation Fatigue Cycles to Failure
Λ^t	Transformation Direction Tensor
f^d	Damage Accumulation Function
c_1, c_2, c_3, c_4	Damage Accumulation Function Calibration Terms
G	Gibbs Free Energy
T	Temperature
ϵ^t	Transformation Strain
g^t	Transformation Hardening Energy
$\mathbf{S}$	Compliance Tensor
c	Specific Heat
s_0	Specific Entropy at the Reference State
u_0	Specific Internal Energy at the Reference State
ρ	Density
α	Theremal Expansion Tensor
$\mathbf{q}$	Heat Flux Vector
r	Rate of Internal Heat Generation
u	Mass-specific Internal Energy
s	Mass-specific Entropy
π^t	Total Thermodynamic Force

TABLE OF CONTENTS

LIST OF FIGURES

xvii

LIST OF TABLES

1. INTRODUCTION AND LITERATURE REVIEW

Over the course of human history, the materials used in systems have been in a constant state of change. Indeed entire time periods of history reflect the importance of the changes in materials being used, such as the bronze age, iron age, and copper age. These changes in material "age" can often be ascribed to changes in the way that materials are treated. Many of these changes have been due to alloying and/or changes in the processing of various metals in order to obtain previously unobtainable properties. Through such changes it has been possible to tailor materials in order to obtain desired responses. Furthermore, alloying and processing changes have lead to the discovery of new phenomena in materials which were previously unknown. Such is the case for Shape Memory Alloys.

1.1   Shape Memory Alloy Behavior

Shape Memory Alloys (SMAs) are part of the class of materials known active materials, meaning that these materials can both sense and actuate. As shown in Fig. 1.1, there are a number of materials which fall into this class of materials including piezoelectric ceramics, ionic electroactive polymers, and SMAs, to name a few [2]. In sensing applications, these materials are able sense a mechanical input and generate a non-mechanical output, while in actuation applications a non-mechanical input is converted into a mechanical output. For SMAs, this coupling is between the mechanical and thermal energy of the system, which leads to a reversible, solid-to-solid, diffusionless, crystallographic phase transformation between austenite and martensite [3]. Furthermore, as shown in Fig. 1.1, although SMAs do not have the highest amount of actuation strain, SMAs do have the highest actuation energy density (actuation stress multiplied by actuation strain).

There are multiple loading paths frequently utilized through which the phase transformation in SMAs are utilized. One such loading path can be utilized to effectively describe the shape memory effect (SME), depicted in Fig. 1.2. In this loading path, the SMA starts at a high temperature under zero stress, labeled as point A in Fig. 1.2. Under these thermo-mechanical conditions, the ma-
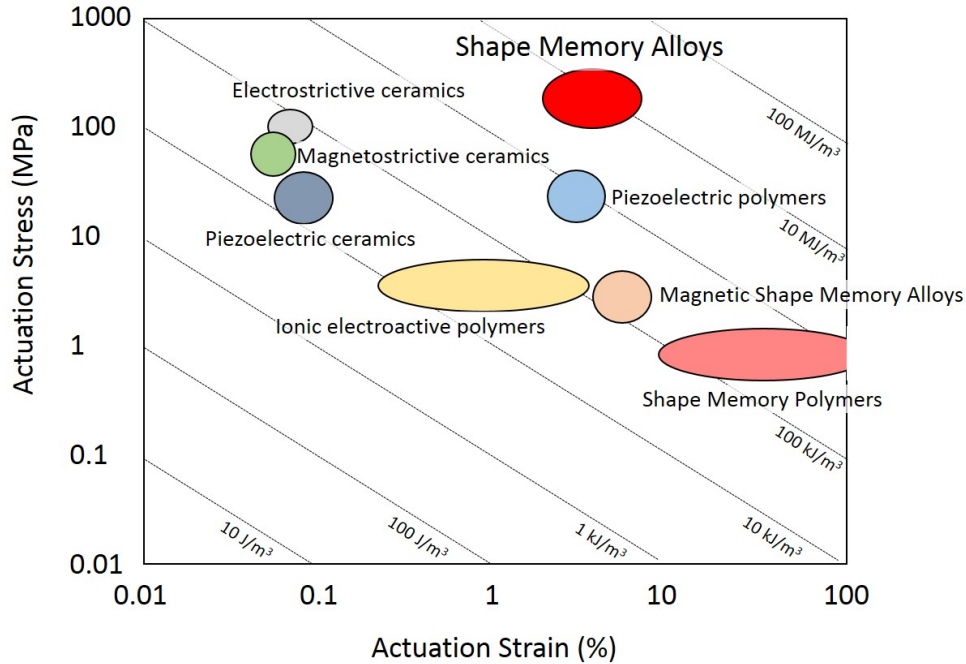
Figure 1.1: Actuation strain v. actuation strain for active materials, with corresponding actuation energy density increasing from bottom left to top right.

terial is in the austenitic phase. Upon cooling through the martensitic Start (M_S) and then below the martensitic Finish (M_F) temperatures while under zero stress, the SMA undergoes the forward phase transformation from austenite into twinned martensite (point B). Once in the twinned martensitic phase, while maintaining a constant temperature, application of a sufficient stress level will lead to detwinning of the crystal structure, resulting in detwinned martensite (point C). During the detwinning process, a significant amount of inelastic strain is introduced into the SMA, such that upon unloading of the material to zero stress this inelastic strain remains in the SMA (point D). However, upon heating of the SMA through the austenite start (A_S) and then through the austenite finish (A_F) temperatures, the inelastic strain can be recovered (point A) [2].

While the SME loading path is a good description of the overall phase transformation behavior of SMAs and is important for historical reasons (which will be addressed in the next section), this loading path is generally not practical in applications. Two more commonly utilized loading paths are the pseudoelastic (isothermal) and the thermal actuation (isobaric) loading paths. In the
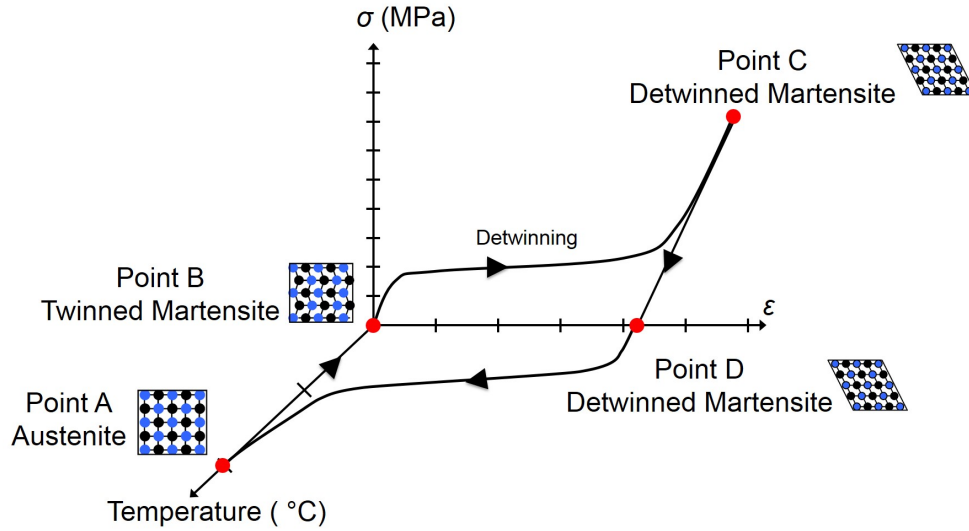
Figure 1.2: Thermomechanical path depicting the Shape Memory Effect in 3D space.

thermal actuation loading path, the SMA is loaded to a fixed stress level while at a temperature well above A_F (in order to ensure the SMA is fully austenitic). The temperature is then reduced, inducing the forward transformation and leading to the formation of actuation strain. The forward phase transformation is noted experimentally to start at a temperature corresponding to point 1 in Fig. 1.3 and to complete at point 2. Upon heating the SMA back to the original temperature, the actuation strain can be recovered. The recovery of the actuation strain is found to begin at a temperature corresponding to point 3 in Fig. 1.3 and complete at the temperature corresponding to point 4. Such a thermal actuation loading path is shown in Fig. 1.4 for a SMA composed of $Ni_{50.3}Ti_{29.7}Hf_{20}$ which has been loaded in tension to 300 MPa. It should be noted, however, that the transformation temperatures while under stress are higher than the transformation temperatures at zero stress. As such the transformation temperatures at stress level σ can be written as M_S^σ, M_F^σ, A_S^σ, and A_F^σ. Performing such thermal actuation loading paths at multiple different load levels and plotting the evolution of M_S^σ, M_F^σ, A_S^σ, and A_F^σ as a function of these stress levels leads to the generation of a phase diagram as shown in Fig. 1.3. The lines coming from the zero stress transformation temperature are referred to as the Clasius-Clapeyron curves and show the effect of stress on the phase transformation temperatures.
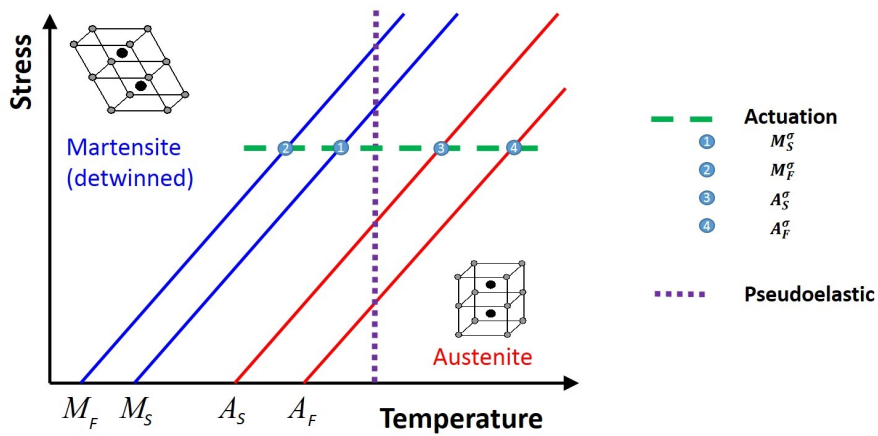
Figure 1.3: Phase Diagram for $Ni_{50.3}Ti_{29.7}Hf_{20}$.
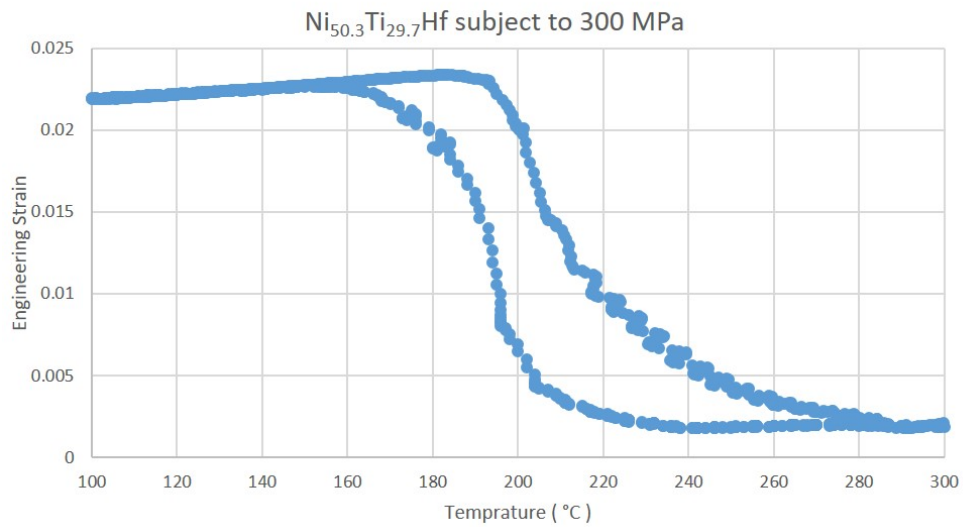
Figure 1.4: Actuation loading for $Ni_{50.3}Ti_{29.7}Hf_{20}$ under 300 MPa.

Given the phase diagram for a SMA, it is frequently possible to find some temperature close to A_F for which application of stress to the SMA, while maintaining a constant temperature, will lead to forward transformation into martensite. Furthermore, since this is done above A_F, removal of the stress will return the SMA into the austenitic phase. Such a loading path is known as the pseudoelastic loading path. Many additional loading paths are available within the stress/temperature

4

space and have lead to the utilization of SMAs in a variety of different applications.

1.2   Shape Memory Alloy History and Applications

As mentioned in the previous section, much interest has been generated in SMAs due to their reversible martensitic phase transformation. Such a solid to solid phase transformation has been known to exist for various alloys since 1932, when Ölander determined that gold-cadmium alloys which, when deformed plastically while cool, could recover their original shape when heated [4]. There were a few more alloys discovered in the 1930s - 1950s which also exhibited SME behavior including copper-zinc and copper-tin [5], indium-thallium, and copper-aluminum-nickel, as well as some additional works attempting to describe the fundamental phenomenon for the SME [6, 7].

In spite of this prior work exhibiting the SME in a variety of alloys, the big breakthrough for SMAs came from William Buehler and co-workers at the Naval Ordnance Laboratory (NOL) in the late 1950s and early 1960s [8, 9]. In 1958, Buehler was attempting to find a metallic alloy which could withstand the high temperature rigors of a missile re-entry nose cone. While searching for materials that could potentially satisfy the requirements, Buehler selected equiatomic nickel-titanium (NiTi) as a system for further investigation. As part of their studies, Buehler and co-workers tested the relative brittleness of the various alloys they were considering. As they were testing equiatomic NiTi, it was found that at a temperature above room temperature, the alloy rang brilliantly when struck, however sounded leaden-like when cooled below room temperature. This acoustic difference lead the team to pursue research into NiTi further. Then, as a demonstration of the fatigue resistance in NiTi, Buehler brought a strip of NiTi bent into an accordion shape to a NOL management meeting. During the meeting, Dr. David Muzzey applied heat from his pipe lighter to the strip and immediately the strip extended with considerable force. This was definitive proof of the SME in NiTi, and since this time the term NiTiNOL has been used extensively as an acknowledgment of this work conducted on nickel-titanium at the Naval Ordnance Laboratory.

Since the discovery of SME in NiTiNOL by Buehler and co-workers, much additional work has been performed to both understand and exploit the unique properties of SMAs. The first commercially successful use of a SMA was the Raychem Corporation CryoFit pipe coupler for

the F-14 jet fighter aircraft [10]. Numerous additional applications have been found for SMAs in a variety of industries [11], including consumer products [12, 13], automotive [14, 15], aerospace [16–18], robotics [19, 20], biomedical [21–23], and even fashion [24]. Looking more closely at the aerospace industry, Hartl and Lagoudas put out a nice review of some of the existing work utilizing SMAs [25], including applications work done as part of the Smart Wing program [26–29] in which the goal was to develop and demonstrate the use of active materials to optimize the performance of lifting bodies. Many additional applications are also reviewed including the SAMPSON project to reconfigure the shape of a jet engine inlet [30], variable geometry chevrons for balancing between noise mitigation and drag reduction [31–35], and rotorblade angle twist [36, 37].

Clearly a number of current applications exist for utilizing SMAs across a number of industries, and more potential applications are under development. However it should be noted that in most of these applications, either the SMAs are utilized in non-critical applications or the SMA components are severely overdesigned. One of the primary reasons why SMAs are limited to such design methods is due to a lack of understanding of the fatigue behavior of these alloys. In order to enable the future use of SMAs, it is therefore of critical importance to understand how the phase transformation in SMAs evolves, both within a single cycle as well as throughout their fatigue lifetime.

1.3   Stress Redistribution during Phase Transformation in Shape Memory Alloys

Much work has been done in SMAs in terms of trying to understand the phase transformation. It is generally well understood that, for NiTi based alloys and their associated tertiary alloys (in which a third element is added, such as Hf, Pd, Pt, Zr, etc.), the austenite phase has a highly symmetric B2 crystal structure, while the martensite phase is composed of the monoclinic B19' crystal structure [3, 38]. Furthermore, the phase transformation is known to propagate along a habit plane, effectively separating the regions of the crystal structure containing the B2 and the B19' crystal structures. Additionally, as mentioned in Sec. 1.1, the martensitic phase can exist either in a twinned or detwinned crystal structure, depending on the loading history of the material. Therefore, due to the physical reorientation of atoms, it is also known that the phase transformation

6

and detwinning process lead to a stress redistribution.

In addition, as shown in Fig. 1.3, the phase transformation is affected by the local stress state of the material. The local stress state of the material is known to be affected by a combination of various local stress concentrators, including grain boundaries [39–41], precipitates [42–44], and geometrical features. Many of these stress concentration sources will exist in SMA components as they are introduced into applications. Therefore understanding how a stress concentration will affect the phase transformation and the associated stress redistribution is critical.

It has also been shown that stress concentrations can have a profound impact on the fracture of SMAs, particularly during phase transformation. Gollerthan et al. experimentally showed that in compact tension specimens, pseudoelastic experiments indicate the formation of martensite around the crack tip prior to failure of the specimens [45]. Similarly, Baxevanis et al. [46] showed that in double notched plate specimens, the presence of these stress concentrations during forward transformation may lead to failure during forward phase transformation while the specimen is subjected to loads as low as 60% of the ultimate tensile stress for the same specimen while in either austenite or martensite(in this study, they used notches on a flat plate to induce the stress concentration). The failure during forward transformation under loads well below the ultimate tensile load was further explored by Jape et al. [47], in which they found that martensite formation near the crack tip in compact tension specimens during cooling under isobaric conditions tends to drive the crack propagation due to an increase in the critical energy release rate as the SMA transforms from austenite into martensite. It is therefore necessary to understand the effect of stress concentrations during phase transformation in order to utilize SMAs safely.

One method which has been utilized extensively to study the effect of stress concentrations is through the use of notched cylindrical specimens. This method of utilizing notched cylinders is frequently used across a number of materials in order to induce as triaxial state of stress [48–52]. By varying the size of these notches, it is possible to study a vast array of triaxiality ratios induced by the variation in the stress concentrations. For clarification, the term triaxiality refers to a ratio between the hydrostatic stress at a point versus an equivalent stress (typically the von Mises stress
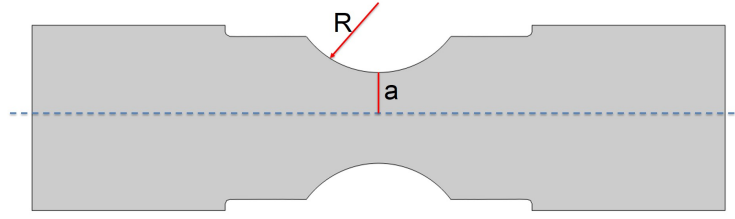
Figure 1.5: Notched cylindrical Specimen with 3.9mm radius notch and 1.95mm radius in plane of minimum cross section, leading to notch acuity of 0.5 ($\frac{a}{R} = 0.5$).

is used as the equivalent stress state) [53]. The triaxiality ratio can be written as

$$\eta = \left(\frac{\sigma_H}{\bar{\sigma}}\right) = \frac{\sigma_1 + \sigma_2 + \sigma_3}{3} + \sqrt{1/2[(\sigma_1 - \sigma_2)^2 + (\sigma_2 - \sigma_3)^2 + (\sigma_3 - \sigma_1)^2]} \qquad (1.1)$$

Use of such specimens can be traced by to Bridgman in 1964 for the purposes of studying fracture [53]. A sample of such a notched specimen is given in Fig. 1.5, in which a notched cylinder is shown with a notch radius, R, of 3.9 mm and a radius for the plane of minimum cross section, a, of 1.95 mm. In keeping with the Bridgman notation as well as with the Code of Practice for Notched Bar Creep Rupture Testing and multiple other studies [54–57], the following document will identify triaxiality specimens using the notch acuity ratio defined as $\frac{a}{R}$.

For SMAs within a single crystallographic phase, the analytical formulas derived by Bridgman in terms of determining the triaxiality ratio are useful. However, when SMAs undergo phase transformation, the analytically determined triaxiality ratios are no longer valid due to the redistribution of stress throughout the SMA. As a function of the phase transformation, and in particular during phase transformation, the hydrostatic stress will change. There has been some prior work by Olsen et al. attempting to study the effect of varying the notch acuity in SMAs [51]. In this study, the authors studied notched cylindrical specimens with 3 notch acuities ($\frac{a}{R} = 0.8, 1, 1.33$) in order to experimentally determine the change in fracture properties due to the variation in specimen geometry. They found that increasing the notch acuity results in a loss of ductility which manifests as a reduction in fracture strain.

Table 1.1: Cycles to failure for SMA applications. Adapted from [1]

Application	Cycles to Failure
Tube Coupling	10^1
Electrical Connectors	10^2
Thermal valve control	10^4
Orthodontic archwires	10^4
Robotic Fingers	10^6
Damping	10^8

1.4 Fatigue in Shape Memory Alloys

The study of the effect of phase transformation in a single cycle is definitely important in order to understand how SMAs behave. However in most practical applications, SMAs will generally not be subject to a single phase transformation cycle and it is therefore necessary not only to understand the behavior of a SMA component within a single phase transformation cycle, but also how the SMA component will evolve throughout its functional lifetime. The term functional lifetime used herein refers to the amount of phase transformation cycles the SMA component can undergo prior to failure. As shown in Table 1.1, although there are some applications for which a SMA component will only be actuated once, most applications require the repeated actuation of SMA components. Therefore, in order to be able to utilize SMAs, it is necessary to understand how SMA components will behave under cyclic phase transformation.

The concept of cyclic phase transformation is analogous to the concept of fatigue. Indeed, in traditional fatigue, a material is subjected to cyclic mechanical loading. As a function of fatigue, various forms of damage will be introduced into the material, including the nucleation of voids, cracks, and other types of damage. These various types of internal damage lead to stress concentrations within the material and eventually materials subjected to fatigue will fail as a result of the internal damage they sustain.

SMAs are also subject to such cyclic mechanical fatigue in a single phase of the material, which will hence forth be referred to as structural fatigue in accordance with the existing literature [58, 59]. The behavior of SMAs under structural fatigue conditions are typical of metals with high

cycle fatigue lifetimes. One of the earliest works on structural fatigue in SMAs was conducted by Melton and Mercier [60] in which they found that the evolution of the stress-strain response in NiTi could be attributed to dislocation activity.

On the other hand, given that dislocation activity is related to the motion of atomic planes through a material, it is therefore no surprise that repeated phase transformation, which is associated with the motion of atoms, would also lead to fatigue. As such, the term functional fatigue has been introduced to describe fatigue due to repeated phase transformation [58, 59]. The area of functional fatigue can be further subdivided into the primary phase transformation inducing mechanisms, that is into pseudoelastic fatigue (due to stress induced phase transformation) or actuation fatigue (due to thermally induced phase transformation). Both of these loading paths are depicted in Fig. 1.3 and extensive research has been done in this area of functional fatigue [42, 59, 61–85]. Much of this research on functional fatigue has been focused on pseudoelastic fatigue due to the use of SMAs in various biomedical related applications. It has been shown that for such pseudoelastic loading paths, the SMA components being utilized are able to sustain over 10^7 transformation cycles prior to failure in cases where the maximum strain is less than 1% but may be as small as 10^3 for actuation strains exceeding 3% [86]. In these studies, the pseudoelastic actuation fatigue lifetime is typically dictated by the alloy under consideration, the processing parameters (heat treatment, hot/cold working, etc), the surface finish (as cast, machined, polished, etc), amount of transformation, and maximum applied load [42, 70–72, 74–78, 80, 85].

Compared to pseudelastic fatigue, the area of actuation fatigue has received relatively less attention. One of the reasons for such a discrepancy in the amount of research conducted on actuation fatigue is due to the time requirement needed to conduct such fatigue experiments [87]. In contrast to pseudoelastic fatigue, where transformation cycles can be completed as quickly as the load can be cycled, actuation fatigue requires that thermal energy be introduced and removed from the SMA in order to complete a phase transformation cycle. During actuation fatigue, preliminary cycling will lead to the rapid accumulation of some level of irrecoverable strain, which is commonly referred to as transformation induced plasticity (TRIP). This preliminary cycling period is
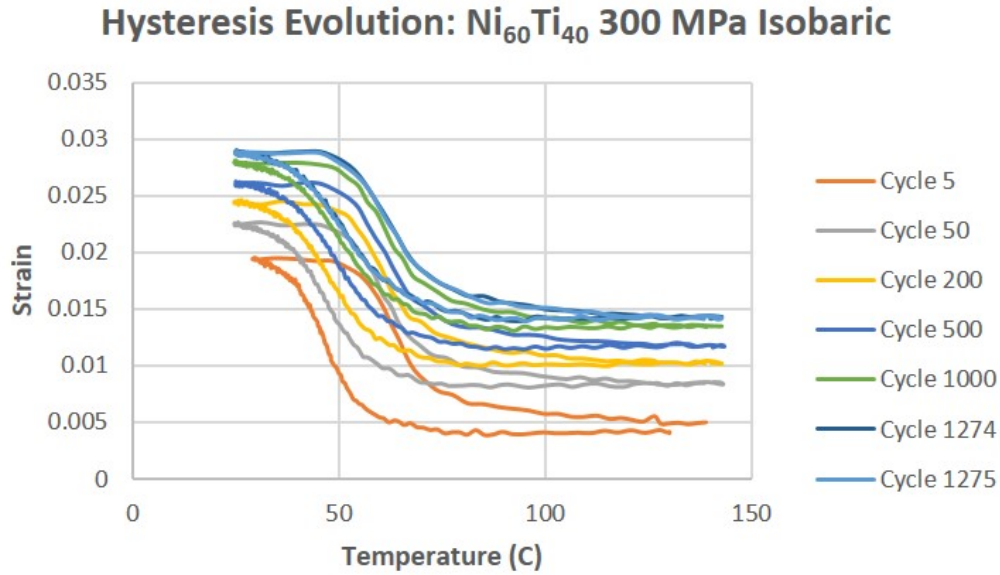
Figure 1.6: Cyclic evolution of hysteresis due to phase transformation in $Ni_{60}Ti_{40}$ subject to a tensile load of 300 MPa.

known as training and is used to stabilize the elastic and transformation properties of the SMA. Such evolution in TRIP is evident due to incomplete closure of the hysteresis loops as shown in Fig. 1.6. The evolution of TRIP during actuation fatigue can be determined by monitoring the evolution of strain at the highest temperature. Therefore, based on the hysteresis plot as shown in Fig. 1.6, it is possible to define the strain at the highest temperature as the austenite strain, the strain at the lowest temperature as the martensite strain, and the difference between these values as the Actuation strain. Such definitions allow for monitoring the evolution of the strain behavior throughout the actuation fatigue life as shown in Fig. 1.7. Based on Fig. 1.7, this initial evolution of irrecoverable strain, which corresponds to the austenite strain curve, increases quickly at the beginning of life but then the accumulation of irrecoverable strain either slows or stops through the rest of the actuation fatigue lifetime.

The first study on actuation fatigue up to failure, published by Bigeon and Morin, found a strong relation between applied stress and cycles to failure [74]. Also, in contrast to structural fatigue which is similar to high cycle fatigue, it was found that SMAs under actuation fatigue

11
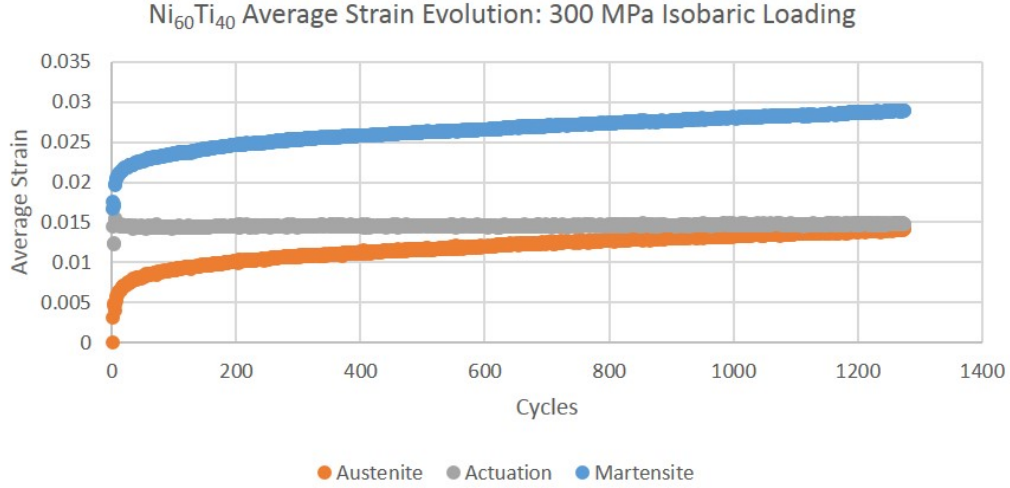
Figure 1.7: Evolution of austenite strain, martensite strain and Actuation strain throughout actuation fatigue lifetime in $Ni_{60}Ti_{40}$ subject to a tensile load of 300 MPa.

are subject to low cycle fatigue. Much additional work has been performed since on the subject of actuation fatigue [58, 61, 65–68, 79, 81–84, 88–90]. Some specific work of interest for the following discussion was conducted by Mammano and Dragoni which also found a correlation between applied stress and cycles to failure [68], similar to the results of Bigeon and Morin. Others have found a stronger relation between irrecoverable strain and cycles to failure [81, 91]. In the works of Calhoun [92] and Agboola et al. [61], where Ni-rich SMAs were studied, precipitation hardened NiTi alloys subjected to constant load conditions were studied and it was found that a power-law relationship existed between the cycles to failure and the actuation work, that is the actuation stress multiplied by actuation strain. This power-law relationship was built as shown in Eq. 1.2, where the terms C^d and γ_d are calibration parameters based on a series of uniaxial test results.

$$N_f = (\frac{\sigma \epsilon^t}{C^d})^{\gamma_d} \tag{1.2}$$

Building on this observation, Calhoun et al. [67] developed a fatigue life prediction tool based on the Smith, Watson, Topper critical plane model [93]. A further work of interest was conducted

by Schick [84] who conducted the first actuation fatigue experiments on plate actuators and examined the effect of the high volume fraction of Ni in $Ni_{60}Ti_{40}$ on the lifetime of these plates under constant load. Based on both the works of Calhoun et al. and Schick, Wheeler et al. [87] introduced an integral formulation for the actuation work in order to account for partial transformation cycles, as well as variable loading.

Several studies have also attempted to look at various aspects related to failure due to functional fatigue. In the work by Karhu and Lindroos [78], they utilized optical microscopy to observe the surface of SMA wires under actuation fatigue and found that although some surface cracks were detected during the actuation fatigue lifetime, the largest detected surface crack did not correspond to the location of the failure. They also obtained some scanning electron microscope (SEM) images in order to observe the fracture surface and found that multiple distinct zones existed on the fracture surface, from smooth to rough, indicating transitions between crack propagation and ductile overload. In the work by Bertacchini et al. [88], the post portem surface of SMA wires were examined using SEM and they found that surface cracks on the SMA wires were periodic. SEM images were also taken of the fracture surfaces and the influence of corrosion on the fatigue life was discussed. In the works by Schick [84] and Calhoun [67], various additional surface level observations of cracks were taken and correlated back to the presence of Ni-rich precipitates in the matrix. In the work by Eggeler et al. [58], SMA wires were subjected to pseudoelastic fatigue and the authors propose a mechanism for failure due to rotation of the wires. This proposed failure mode is a direct result of post mortem SEM analysis of the fracture surface rather than basd on determination of in-situ damage accumulation observations. From a modeling perspective, Chemisky et al. [94] developed a damage accumulation model which assumes a linear relationship between the accumulation of damage and the number of cycles to failure under actuation fatigue.

1.5 Goals and Objectives

In order to examine the effect of phase transformation in SMAs throughout the entire lifetime of a SMA actuator, it is necessary to understand the effect of the phase transformation within a single phase transformation cycle as well as during repeated cycling. As has been stated in

13

Sec. 1.4, the formation of damage due to fatigue is directly linked with the formation of stress concentrations. To this end, there are two primary goals for this work, one studying the effect of stress concentrations on the phase transformation within a single phase transformation cycle, and the second goal looking at the evolution of damage within a SMA actuator due to cyclic phase transformation. The study of each of these goals will be performed both numerically and experimentally, leading to 4 individual sections which will constitute the body chapters of this dissertation.

1.5.1 Stress Redistribution Due to Phase Transformation

As stated previously, during phase transformation, the atoms locally move due to the crystallographic reconfiguration. This crystallographic reconfiguration leads to a redistribution in the stress throughout the specimen. Therefore, it is imperative to understand the interaction between phase transformation and stress redistribution within a single phase transformation cycle in order to understand how each phase transformation cycle will affect the stress throughout the entire lifetime of a SMA actuator.

1.5.1.1 Simulation of Stress Redistribution in Notched Cylindrical Shape Memory Alloys

By simulating the phase transformation in a number of notched cylinders with different notch acuity ratios, it is possible to investigate the effect of different stress concentrations. By coupling the magnitude of the stress concentration to the phase transformation, it is therefore possible to investigate how the various stress concentrations affect the stress redistribution in a SMA specimen due to phase transformation. Therefore, it is a primary goal of this work to analyze how the stress concentrations due to the notches in notched cylindrical SMA bars lead to variation in the phase transformation due to stress redistribution. Both thermal actuation and pseudoelastic loading paths will be considered. A spectrum of notched cylindrical SMA bars are used, ranging in notch acuity from 0.2 to 50. Utilization of numerical simulations across this range of notch acuities allows for a number of different and interesting phenomena to be investigated.

1.5.1.2   Experimental Validation of Thermal Actuation Simulations in Notched Cylindrical Shape
Memory Alloy Bars.

The results of the simulations provide some interesting perspectives on the effect of stress redistribution in SMA components. In order to validate these results, a number of experiments were also conducted, using both $Ni_{50.8}Ti_{49.2}$ as well as $Ni_{50.3}Ti_{29.7}Hf_{20}$. Experiments at TAMU were able to capture overall surface strain behavior. Additional experiments utilizing neutron diffraction performed at Oak Ridge National Lab provide further experimental insight into the phase transformation of the material through quantitative analysis of the crystal structure of the material as a function of temperature. Furthermore, it is the goal of this dissertation to show a correlation between the numerical and experimental results, and utilize the numerical results to help explain the difference in crack initiation and propagation.

1.5.2   Damage Evolution in a Shape Memory Alloys undergoing Phase Transformation via Thermal Actuation

As stated previously, SMA actuators will generally be utilized through multiple actuation cycles. Therefore in order to understand the effect of phase transformation in a SMA from a damage perspective, it is necessary to not only analyze the effect of stress concentrations within a single cycle, but also to understand how these stress concentrations nucleate and evolve throughout the actuation fatigue lifetime.

1.5.2.1   Characterization of Damage Evolution

Surface cracks are known to nucleate and evolve during the actuation fatigue lifetime. However it is unclear how internal damage evolves during the actuation fatigue lifetime of SMA components. It is therefore a goal of this dissertation to determine how internal damage forms and evolves during the actuation fatigue lifetime. The primary method for this analysis is through the use of X-ray computed microtomography as a non-destructive method to evaluate local areas within the SMA actuators that present cracks. All SMA specimens are fatigued utilizing previously established actuation fatigue testing methods [87]. The experimental technique used allowed for monitoring

of both the local and global strain evolution. Additional testing was performed in order to monitor the evolution of the effective elastic modulus throughout the actuation fatigue lifetime.

1.5.2.2 *Actuation Fatigue Damage Evolution Model Refinement*

Based on the damage evolution characterization results, it is found that damage evolves in SMA actuators in a non-linear fashion. Therefore it is a further goal of this work to refine existing actuation fatigue damage evolution models by introducing these non-linear effects. As will be shown in Ch. 4, three distinct phases of damage evolution can be obtained from the damage evolution characterization. As such, a linear decomposition is introduced to account for these differences in damage evolution. The initial damage evolution is shown to follow the evolution of irrecoverable strain, giving some credence to the actuation fatigue lifetime models based on irrecoverable strain. However the later damage evolution is shown to be exponential, in accordance with typical fatigue models. Therefore, an exponential term is also utilized to capture the damage evolution with a particular focus on damage growth and coalescence near the end of fatigue life. The proposed damage evolution model is introduced into a thermodynamically consistent phenomenological modeling framework and then implemented in order to show the applicability of the damage model to predict the accumulation of damage throughout the actuation fatigue lifetime, as well as enable the predication of the actuation fatigue lifetime under arbitrary loading conditions.

2. SIMULATION OF STRESS REDISTRIBUTION IN NOTCHED CYLINDRICAL SHAPE MEMORY ALLOYS [1]

Throughout the functional life of a SMA, it will undergo numerous phase transformations. As mentioned in Ch. 1, each time a SMA undergoes a phase transformation, the atoms will physically move, leading to a redistribution in the stress field inside the SMA member. Furthermore, as SMA members are attached and/or embedded within structures, they will necessarily be subjected to various stress concentrators, either due to the attachment points themselves or due to the introduction of damage as the SMAs undergo fatigue. Therefore, the following chapters will focus on how stress concentrations affect the phase transformation through the use of notched cylindrical SMA bars. Furthermore, as will be discussed in Ch. 4 and Ch. 5, the size of stress concentrations within SMAs undergoing repeated phase transformation will tend to increase. Therefore, it is useful to study the effect of stress concentrations of various sizes within a single phase transformation cycle in order to develop a better understanding of how the stress field within a SMA component will change over the course of the lifetime of the SMA component.

The balanced use of both numerics and experiments is useful in order to be able to explore a wide scope of parameters, while at the same time ensure physically obtainable behavior. To that end, both numerical and experimental results were obtained in the following study. The numerical results allow for a large range of notch acuities to be explored, while the experimental results are utilized to ensure the numerical results can be physically realized. In this chapter, various notched cylindrical SMA bars will be simulated in order to determine the effect of stress redistribution during phase transformation, while the experimental results will be presented in the following chapter. There are three main sections to this chapter. First, the approaches utilized for the numerical anal-

ysis of the impact of phase transformation on stress redistribution in pseudoelastic and thermal actuation loading paths are discussed. Then the results for notched cylindrical SMA bars subjected to pseudoelastic loading will be presented. Such pseudoelastic loading provides some interesting insight on how stress redistributes during transformation due to the fact that such loading utilizes stress to induce phase transformation. Section 2.3 then presents simulations on notched cylindrical SMA bars subjected to thermal actuation loading paths. These thermal actuation simulations highlight the importance of the stress redistribution further since, as will be shown through these simulations under constant load, the stress redistribution can have a profound impact on the evolution of the phase transformation.

2.1 Numerical Approach

As stated in Sec. 1.3, a number of previous studies exist which utilized notched cylindrical bars in order to explore the effect of stress concentrations on a variety of materials and under a number of conditions [48–53]. The use of such notched cylindrical bars allows for the application of stress along the primary axis of revolution of the cylinder, while geometric effects due to the notch induce a triaxial state of stress. Therefore, it was decided to use such notched cylindrical bars to investigate the effect of the stress concentration induced by the notches to explore the resulting behavior in SMAs.

In order to determine the effect of notch acuity on the stress redistribution for a wider range of stress concentrations then would be possible experimentally, a number of test specimens were generated. These specimens range in notch acuity, $\frac{a}{R}$, from 0.2 to 50, in addition to a nominally smooth cylindrical dogbone specimen to use for verification of model calibration (see Fig. 2.1). By utilizing this range of notch acuities, it is possible to account for a wide variation in stress concentrations which may be found in practical applications where a cylindrical member is held in place through a circular hole. Due to the symmetry of the cylindrical specimens, only a quarter of the specimens was utilized for the simulations. For all simulations in this chapter, 4-node thermally coupled tetrahedrons were used as meshing elements. Two sizes of mesh were utilized throughout the specimens: a coarse mesh in the grip region and a fine mesh starting half way into the region

with the initial radius reduction and going through the notched portion of the specimen. A sample of how the specimens were meshed is shown in Fig. 2.2 for the $\frac{a}{R} = 1$ specimen.
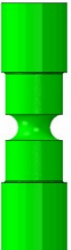
Notch Acuity, $\frac{a}{R}$	50	10	1.25	0.2	Smooth
Geometry					

Figure 2.1: Notched cylindrical bars with corresponding notch acuity.
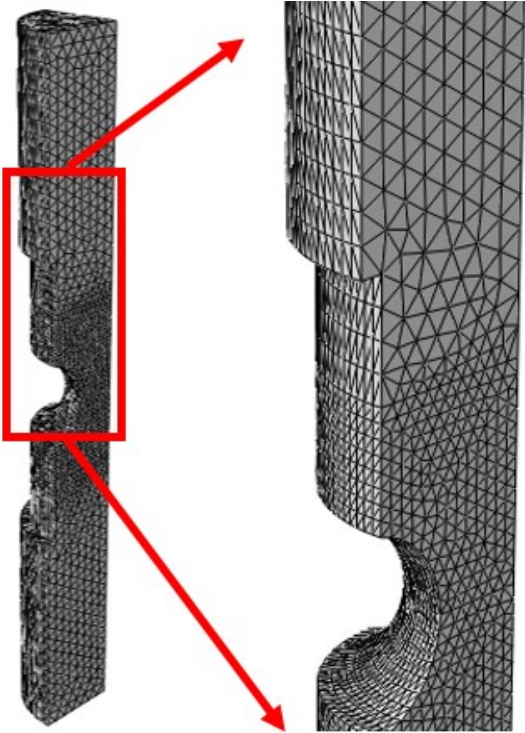
Figure 2.2: Mesh for the $\frac{a}{R} = 1$ specimen.

In order to simulate the SMA constitutive response, the SMA constitutive model of Lagoudas et al.[95] was utilized via implementation of the consitutive model into a user material subroutine (UMAT) in ABAQUS. The model utilizes a J_2 plasticity type phase transformation surface based on the deviatoric von Mises stress in order to determine the pointwise behavior throughout the material. The constitutive model material parameters used for all simulations are given in Table 2.1 and are based on experimental results for the smooth cylindrical dogbone using experimental specimens and setup as described in Ch. 3. Further information on the model parameter characterization procedure can be found in the work by Hartl and Lagoudas [34].

Property	Value
A_S	262 K
A_F	274 K
M_S	255 K
M_F	247 K
E_A	56 GPa
E_M	50 GPa
α_A	$2.5x10^{-5} \frac{1}{K}$
α_M	$2.5x10^{-5} \frac{1}{K}$
ν	0.33
C_M	8.5 MPa/K
C_A	8.2 MPa/K
H_{min}	0
H^{max}	0.065

Table 2.1: Material Properties used in SMA Model. Based on experimental results of smooth specimens.

As a preliminary exploratory study of the effect of notch acuity on the phase transformation, a subset of these cylinders were selected for investigation utilizing the pseudoelastic loading path, matching the notched cylindrical SMA bars used experimentally. For these simulations, the smooth, $\frac{a}{R} = 0.5$, and $\frac{a}{R} = 2.5$ specimens were studied. The bottom of each specimen was fixed and the temperature was held constant at 298 K, thereby mimicking the experimental conditions. The specimens were then loaded to 200 MPa along the top of the specimens (200 MPa selected

due to ability of the load to induce phase transformation in all specimens near the middle of the pseudoelastic loading cycle).

In addition to the pseudoelastic simulations, a larger study was also performed for thermal actuation loading paths under nominally constant force conditions. As such the bottom of each cylinder was fixed, while a uniform initial load of 200 MPa was applied to the top surface. The notched cylinders were initially at 500 K. While maintaining the load constant, the temperature was then reduced to 225 K (below M_F) and subsequently heated back up to 500 K. The temperature is assumed to be uniform throughout the entire specimens. Throughout the thermal actuation path, the stress, strain, and martensitic volume fraction are monitored in order to determine the effect of the thermal actuation loading path on these parameters.

In addition to the thermal actuation simulations performed as described above, additional thermal actuation simulations were conducted in order to compare with experimental results. These simulations for experimental comparison were performed in the same manner as described previously for the $\frac{a}{R} = 0.5$ and $\frac{a}{R} = 2.5$ specimens, however the temperature was cycled from 500 K to 310 K in accordance with the experimentally achievable minimum temperature as described below. Also, for experimental comparison purposes, notch axial extension was obtained by comparing the distance between nodes at the top and bottom of notch. Similarly, notch radial extension was obtained by monitoring the radial position of two points on the outside edge of the plan of minimum cross section. The results of these simulations for use as comparison to the experimental results will be saved for discussion in Sec. 3.3 after the experimental results are presented.

2.2   Pseudoelasticity in Notched Cylindrical Shape Memory Alloy Bars

A good place to start the analysis of the impact of stress concentrations on the phase transformation in SMAs is through loading paths directly related to the stress in a SMA since, as shown in Fig. 1.3, the phase transformation in SMAs is directly related to the stress level in the material. Therefore, the pseudoelastic loading path is first considered for notched cylindrical SMA bars.

In attempting to understand how a stress concentration affects the phase transformation and associated stress redistribution, it is informative to first consider the evolution of the martensitic

volume fraction is considered during a pseudoelastic test. As shown in Fig. 2.3, the forward transformation initiates at the notches for the $\frac{a}{R} = 2.5$ and $\frac{a}{R} = 0.5$ specimens, as expected due to the presence of the stress concentration. For the smooth specimen, the transformation initiates throughout the center of the specimen, as expected since no distinct stress concentrations are present. for the smooth specimen, the phase transformation then spreads above/below this point of initiation as indicated in Fig. 2.4. However, as the transformation progresses in the $\frac{a}{R} = 0.5$ and $\frac{a}{R} = 2.5$ specimens, the propagation of the transformation front is different, as also shown in Fig. 2.4. For the $\frac{a}{R} = 0.5$ specimen the transformation goes through the center of the specimen first, and then propagates above and below this region of minimum cross-section. On the other hand, for the $\frac{a}{R} = 2.5$, the transformation bands propagate around the center of the specimen in a spherical pattern, meaning that regions along the central axis above and below the plane of minimum cross-section transform prior to the region along the central axis on the plane of minimum cross-section. This is a very interesting result which leads to a number of other interesting phenomena which shall be discussed further below.

Another interesting aspect which bears investigation due to the difference in how the phase transformation propagates based on the various notches is the distribution of stress in the specimens, especially considering that the phase transformation in a SMA is directly impacted by the local state of stress. As shown in Fig. 2.5 (taken at the same time step as used in Fig. 2.4), the areas of highest stress correlate exactly with the distribution of the martensitic volume fraction. In other words, for the smooth and $\frac{a}{R} = 0.5$ specimens, the areas of highest stress are in the planes of minimum cross-section. However, for the $\frac{a}{R} = 2.5$ specimen, the stress propagates in a circular pattern from the notches to regions above/below the area along the central axis of the plane of minimum cross-section.

Furthermore, in order to help with the discussion on the difference in strain behavior between axial and radial as mentioned in the experimental results, the strain results based on the numerical simulations are now presented. The axial strain results show a similar distribution as shown in the martensitic volume fraction and stress distribution figures and are not presented below. It is worth

(a)

(b)

(c)
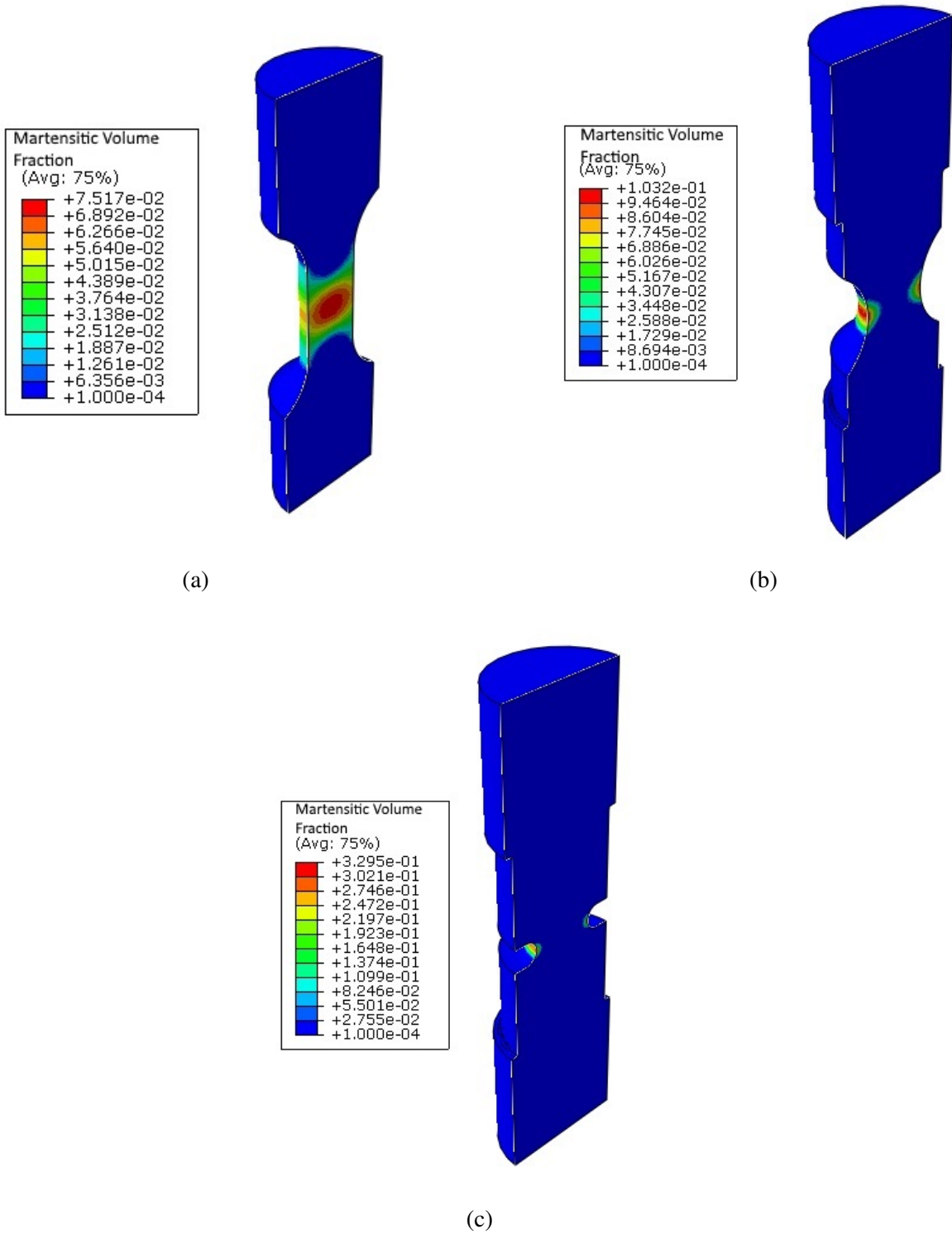
Figure 2.3: Cross-sectional view of martensitic volume fraction at initiation of forward transformation for (a) smooth; (b) $\frac{a}{R} = 0.5$; and (c) $\frac{a}{R} = 2.5$.
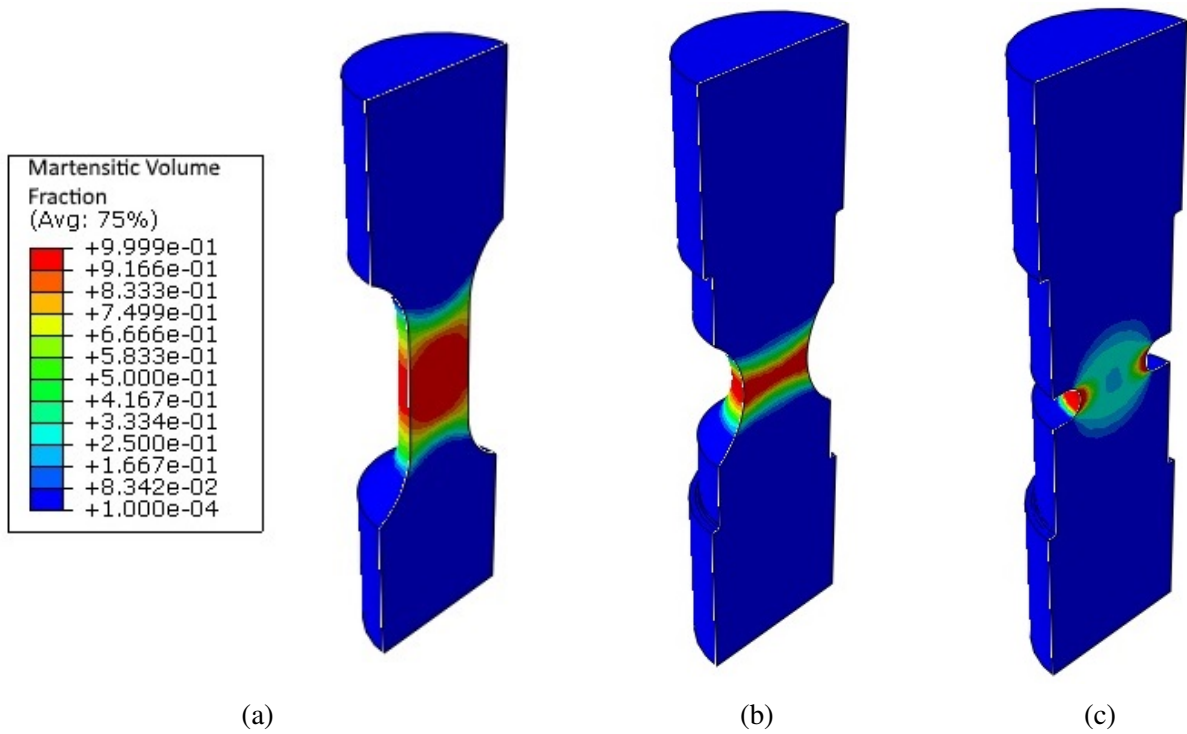
Figure 2.4: Cross-sectional view of martensitic volume fraction of (a) smooth upon first reaching full transformation in center of specimen ; (b) $\frac{a}{R} = 0.5$ upon first reaching full transformation in center of specimen ; and (c) $\frac{a}{R} = 2.5$ showing circular evolution of martensitic volume fraction around center of specimen.

noting that the $\frac{a}{R} = 2.5$ specimen shows that the axial strain evolves in a spherical pattern from the notch and then above/below the plane of minimum cross-section to the central axis. This means that it is possible to have a high axial strain value without transformation along the central axis of the plane of minimum cross-section, in agreement with the experimental results shown in Fig. 3.4. However, the radial strain results do present interesting results. As shown in Fig. 2.6, the radial strain for the smooth and $\frac{a}{R} = 0.5$ specimens indicates that at completion of loading, the area of minimum cross section shows a generally uniform reduction in radius. However, for the $\frac{a}{R} = 2.5$ specimen, while the edges of the notch do show a significant change in radial strain, the rest of the plane of minimum cross-section does not indicate much change in radial strain. Therefore, even though the edges do show much strain, in an averaged sense, the radial strain along the plane of minimum cross section does not change much, in agreement with the experimental results to be
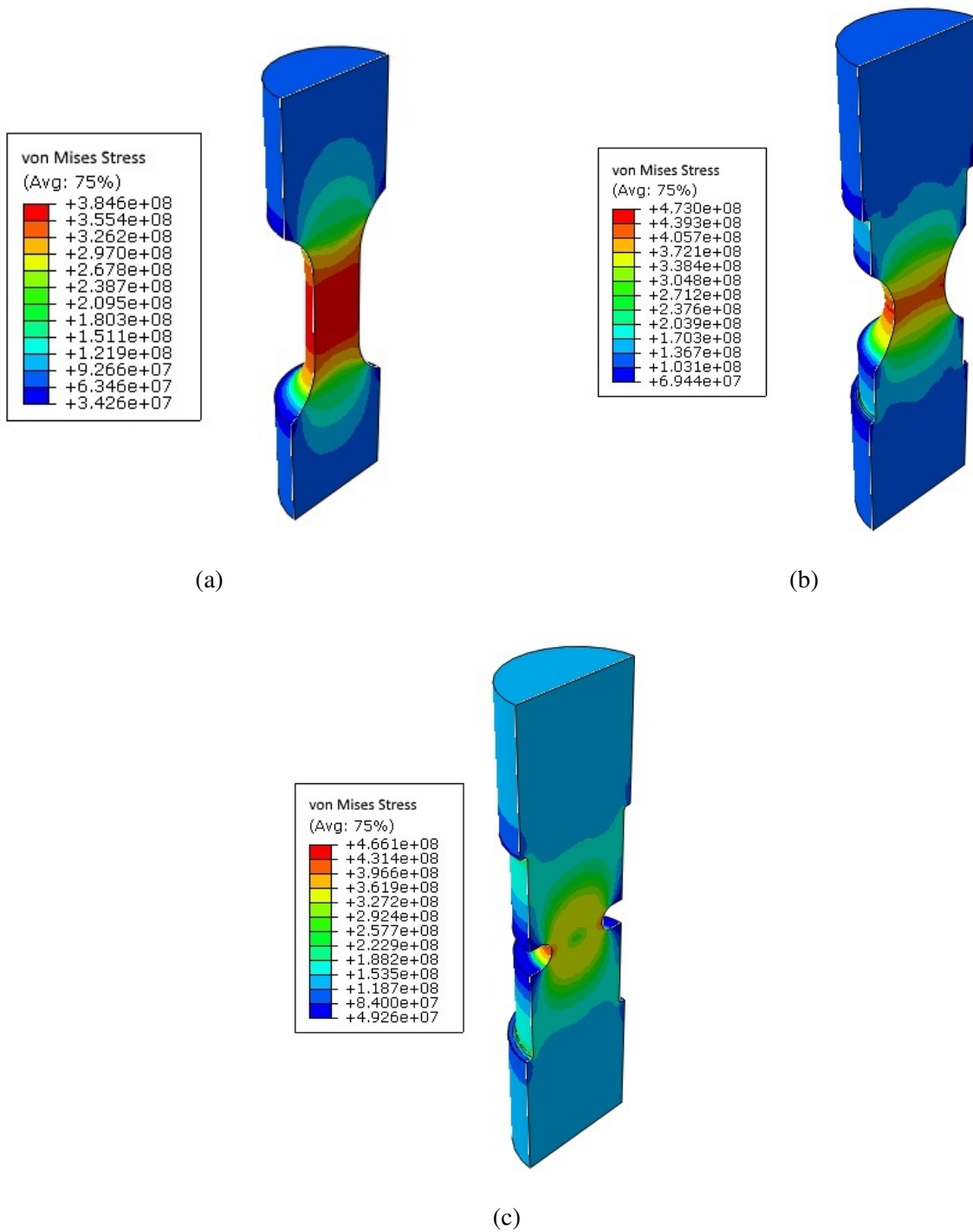
Figure 2.5: Cross-sectional view of Von Mises stress of (a) smooth upon first reaching full transformation in center of specimen ; (b) $\frac{a}{R} = 0.5$ upon first reaching full transformation in center of specimen ; and (c) $\frac{a}{R} = 2.5$ showing circular stress distribution around center of specimen.

presented in Sec. 3.2.

2.2.1 Discussion

The results shown above lead to several interesting points. The first observation is that as the notch acuity is increased by introducing and reducing the size of the notch, there is a critical notch size at which the phase transformation stops propagating along the plane of minimum cross section, but rather starts to propagate around this plane in a spherical pattern(based on Fig. 2.4). This observation helps to explain why even though the local axial strain in a $\frac{a}{R} = 2.5$ specimen may be greater than the local axial strain in the $\frac{a}{R} = 0.5$, yet the local radial strain for the $\frac{a}{R} = 2.5$ is less than the local radial strain for the $\frac{a}{R} = 0.5$ in the plane of minimum cross section. By having the phase transformation propagate in a spherical pattern above and below the plane of minimum cross section in the $\frac{a}{R} = 2.5$ specimen, therefore the phase transformation near the central axis on the plane of minimum cross section of the $\frac{a}{R} = 2.5$ specimen is delayed. Because of this delay, the material in the middle of the plane of minimum cross-section for the $\frac{a}{R} = 2.5$ specimen does not reorient in the direction of the load, leading to a smaller reduction in radial strain for the $\frac{a}{R} = 2.5$ specimen as compared to the smooth and $\frac{a}{R} = 0.5$ specimens, for which at the same load level the material at the center of the plane of minimum cross section does reorient along the axial direction.

Furthermore, since the area along the central axis above and below the plane of minimum cross-section for the $\frac{a}{R} = 2.5$ specimen exhibits phase transformation prior to the area along the central axis on the plane of minimum cross-section, therefore this area along the plane of minimum cross section is shielded from the need to strain. Since the area along the central axis on the plane of minimum cross-section has a lower strain due to the shielding, therefore the stress in this area is also lower. However due to force balance, this means that the area around the notches on the plane of minimum cross-section must therefore sustain a higher amount of load. This can be seen in Fig. 2.7, where it is shown that initially the stress throughout the cross-section increases (corresponding to 20% of maximum load). However upon reaching 40% of maximum load, the phase transformation starts to initiate at the edge (as indicated in Fig. 2.8), leading to an almost constant stress level in the phase transforming region. The phase transforming region continues to

(a)

(b)

(c)
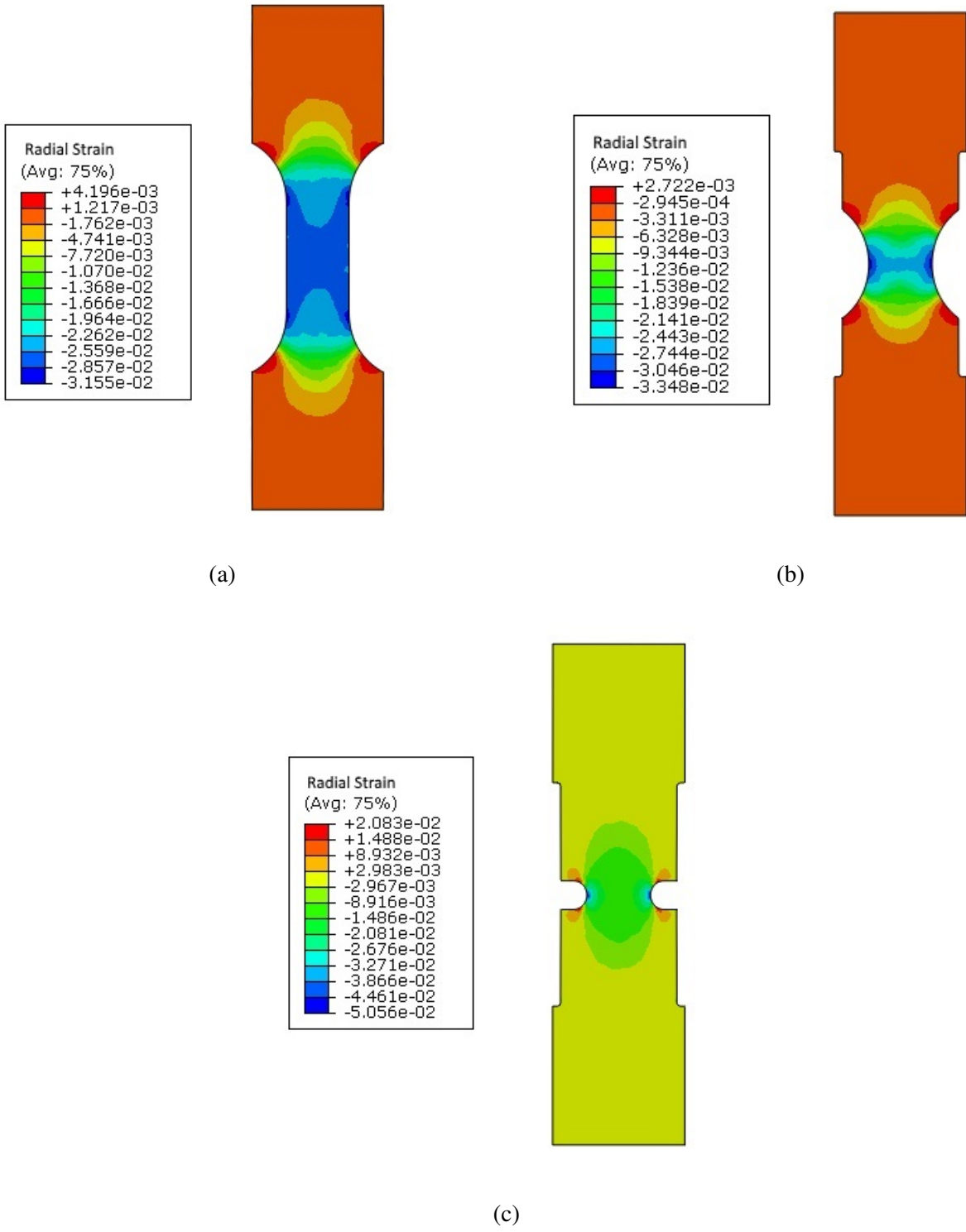
Figure 2.6: Cross-sectional view of radial strain at completion of pseudoelastic loading for A) smooth; B) $\frac{a}{R} = 0.5$; and C) $\frac{a}{R} = 2.5$.

expand through 60% of maximum load, and therefore there is a larger region of constant stress for 60% of maximum load. At 80% of maximum load, the material close to the notch has completed transformation and would therefore behave elastically. However the rest of the area in the plane of minimum cross section is still transforming and can therefore not support additional load, meaning that the elastic region near the notch must support any further increase in load until transformation is completed. This can be further seen by the additional increase in stress near the notch as shown at 100% of maximum load.
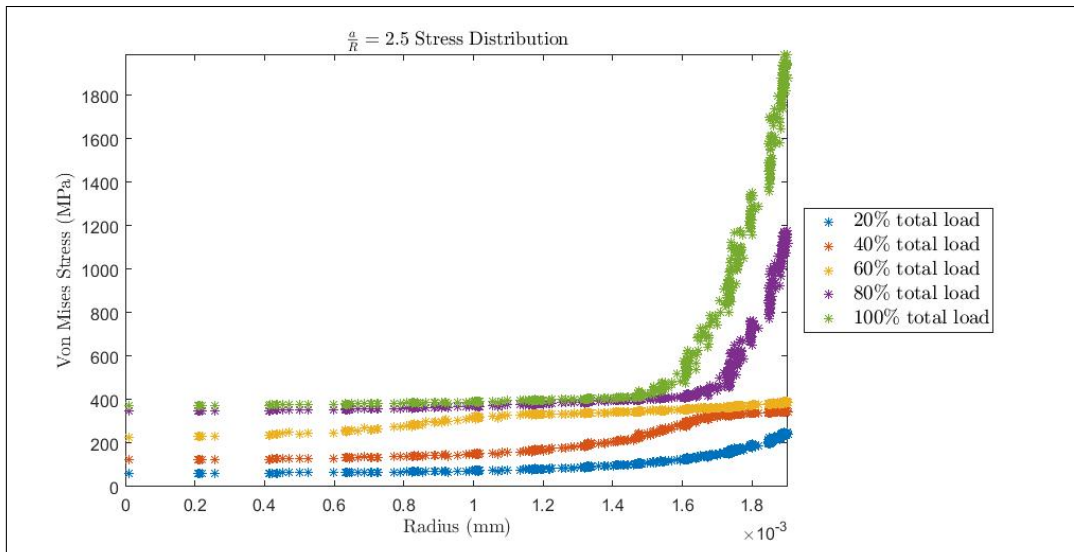
Figure 2.7: Radial stress distribution for the $\frac{a}{R} = 2.5$ specimen at 20%, 40%, 60%, 80%, 100% of maximum load.

This effect of causing the load level to increase drastically near the notch wall in the plane of minimum cross-section while the rest of the plane of minimum cross-section is still undergoing phase transformation is due to the method in which the phase transformation propagates in the $\frac{a}{R} = 2.5$ specimen. By comparison, the stress distribution for the $\frac{a}{R} = 0.5$ specimen during pseudoelastic loading, shown in Fig. 2.9, does not have as drastic of an edge effect when compared to the $\frac{a}{R} = 2.5$ stress distribution from Fig. 2.7. As can be seen for the $\frac{a}{R} = 0.5$, while there is a stress level for which the phase transformation causes an almost uniform stress distribution (60%
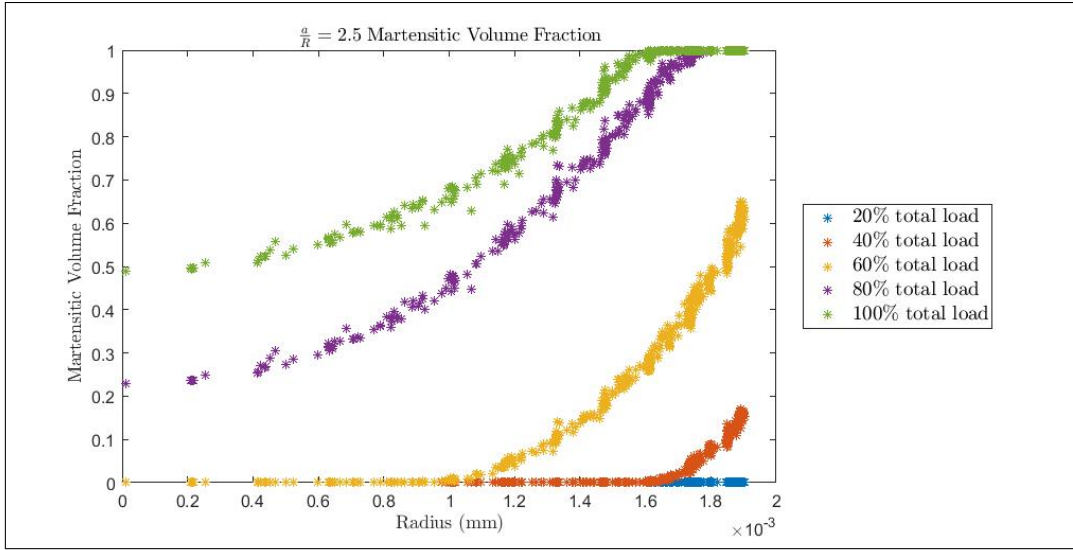
Figure 2.8: Radial martensitic volume fraction distribution for the $\frac{a}{R} = 2.5$ specimen at 20%, 40%, 60%, 80%, 100% of maximum load.
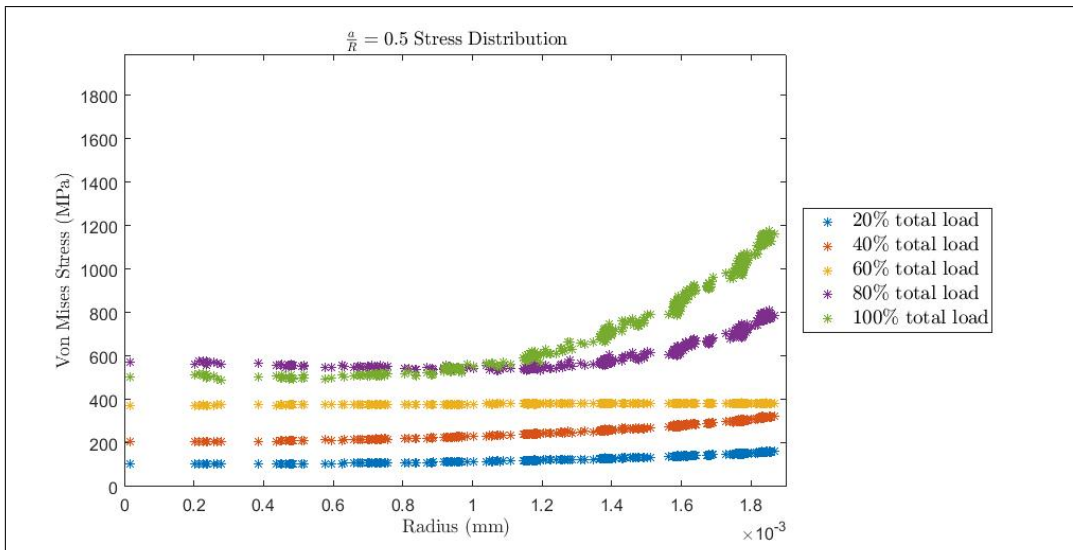
Figure 2.9: Radial stress distribution for the $\frac{a}{R} = 0.5$ specimen at 20%, 40%, 60%, 80%, 100% of maximum load.

of maximum load), because the phase transformation propagates through the plane of minimum cross-section prior to moving above and below this plane, therefore the stress distribution at 100% of maximum load shows a stress distribution as would be expected for a typical elastic material.

Thus, by increasing the notch acuity, the phase transformation can lead to a dramatic increase in stress near the stress concentration due to suppression of the phase transformation away from the stress concentration, which could lead to early failure as evidenced by Baxevanis et al. [46].

2.3 Thermal Actuation in Notched Cylindrical SMA Bars

The results presented above for the analysis of notched cylindrical SMA bars subjected to pseudoelastic loading present an interesting view into how the application of stress can lead to differences in phase transformation due to the presence of stress concentrations. Given that the phase transformation is shown to strongly depend on these stress concentrations, it is also useful to consider other commonly used loading paths. Specifically, for actuation type applications, the results shown in Sec. 2.2 suggest that it is necessary to understand how stress concentrations affect the phase transformation and associated stress redistribution in thermal actuation loading paths. Furthermore, Chs. 4 and 5 both focus on actuation fatigue and therefore understanding how stress redistributes in a single cycle is informative to understanding how damage may evolve in every cycle of the actuation fatigue lifetime.

2.3.1 Results on Thermal Actuation of Notched Cylindrical SMA Bars

As a result of the thermal actuation cycles, it is expected that the notched cylinders will undergo phase transformation due to cycling between temperatures well above A_F^σ to a temperature below M_F^σ. However, in addition to the bulk behavior expected by cycling from above A_F^σ to below M_F^σ, it is important to consider the implications of the interaction between stress and temperature, in particular near stress concentrations such as that due to the notches in the notched cylindrical bars under consideration. This interaction between the stress and phase transformation is responsible for the differences in evolution of the phase transformation as shown in Fig. 2.10, which shows three different specimens representative of the different transformation characteristics. It can be seen in Fig. 2.10 that, although the phase transformation initiates at the edge of the notches for all specimens, the way in which the phase transformation progresses is different for the different notch acuities. For small notch acuities ($\frac{a}{R} < 0.4$ and the smooth baseline), the phase transfor-

mation first propagates along the plane of minimum cross-section prior to expanding above/below this plane. For high notch acuities ($\frac{a}{R} > 2.5$), the phase transformation propagates spherically out from the notch edge to areas above/below the plane of minimum cross-section. However, for intermediate notch acuities ($0.4 < \frac{a}{R} < 2.5$), an interesting behavior can be noted. Taking the specimen with a notch acuity of 1.25 as an example, it can be seen that while the phase transformation does initially propagate through the plane of minimum cross-section as shown at 295 K, the spherical phase transformation propagation behavior becomes dominant by 275 K. Furthermore, at 265 K, it appears that material which had completed phase transformation at 295 K has now undergone some reverse phase transformation in regions close to the central axis along the plane of minimum cross-section. It is only through continued cooling below the M_F temperature that this region completes forward transformation. The phase transformation reversal appears to occur for a number of different notch acuities, corresponding to the intermediate notch acuity range mentioned above, as will be discussed further in the following paragraphs.

In order to better understand the phase transformation reversal, the notched cylindrical specimen with a notch acuity, $\frac{a}{R}$, of 1 is further examined. Numerical results indicate that phase transformation initiates at the edge of the notch at approximately 371 K and propagates along the plane of minimum cross-section as well as moving above and below this plane close to the notch wall. This can be seen clearly at 325 K in Fig. 2.11. By 295 K, phase transformation has completed throughout the plane of minimum cross-section as well as for some other material close to this plane near the notch wall. However, according to direction of phase transformation in Fig. 2.11, there is widespread reverse transformation by 285 K near the center of the plane of minimum cross-section, which has lead to the material near the center to go back to a mixed phase between austenite and martensite. Indeed, it can be noted from Fig. 2.11 that by 285 K, up to 60% of the plane of minimum cross section (and material close to this plane) is undergoing reverse phase transformation. In the mean time, other surrounding material completes phase transformation as indicated by the circular region of complete phase transformation at 280 K. Reverse transformation in this specimen can be found throughout the center of the plane of minimum cross-section of
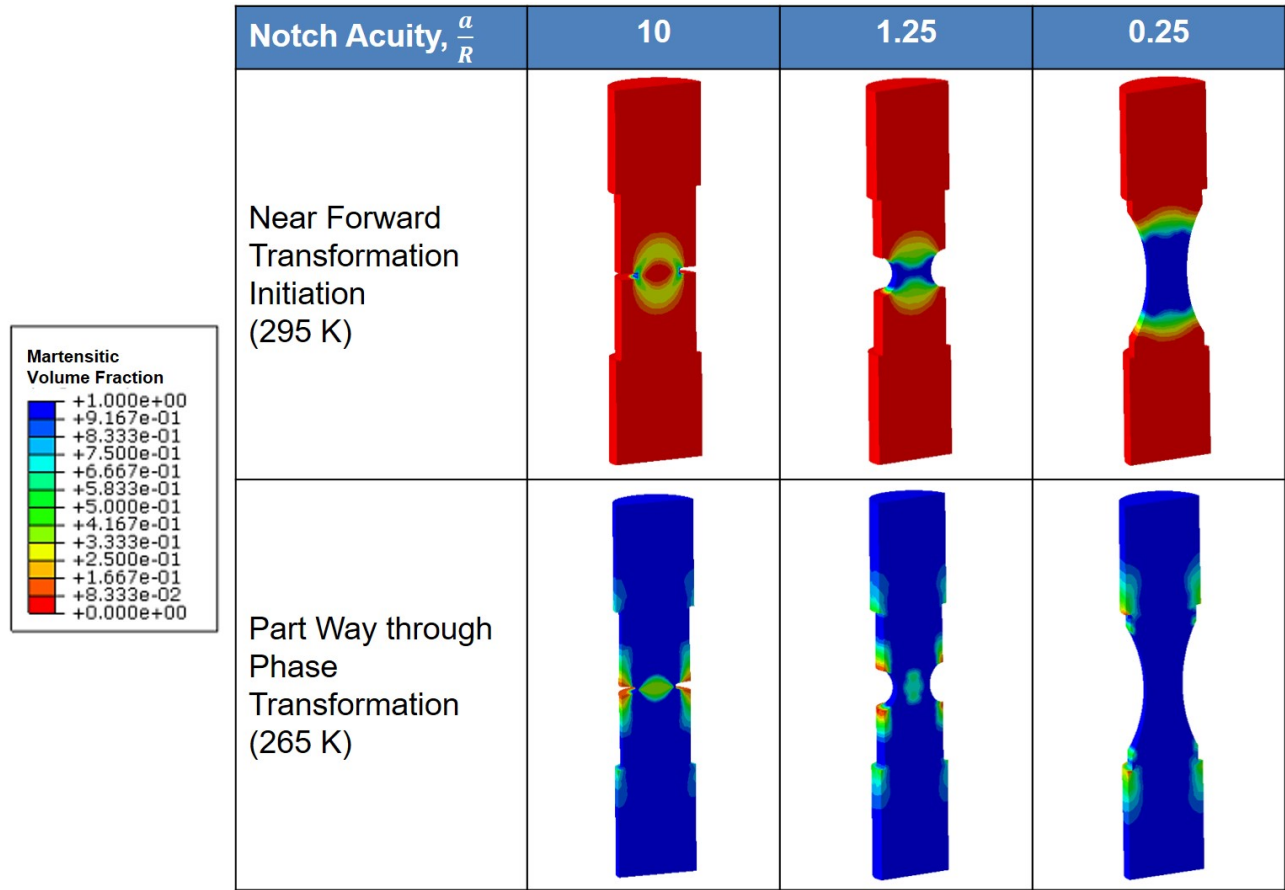
Figure 2.10: Comparison of martensitic Volume Fraction during forward transformation for various specimens. All specimens subjected to 200 MPa nominal stress.

this specimen from 288 K to 275 K, and forward transformation does not resume throughout the specimen until 265 K.

For further clarification on what leads to the partial phase transformation reversal, it is important to recall that the phase transformation is thermomechanically driven, that is both temperature and stress contribute to the phase transformation. Therefore, the reason for the phase transformation reversal may be deduced by examining the local stress state in conjunction with the temperature. Consider further the specimen with a notch acuity $\frac{a}{R} = 1$. As discussed above based on Fig. 2.11, phase transformation clearly completes throughout the plane of minimum cross section by 295 K. However by 285 K, at least part of this plane of minimum cross section has undergone some

Temperature (K)	325	295	285	280	250
Material Phase ■ Austenite ■ Mixed ■ Martensite					
Direction of phase transformation ■ Forward ■ No PT ■ Reverse					
von Mises Stress Distribution 2.9e+09 2.2e+09 1.5e+09 7.2e+08 0					
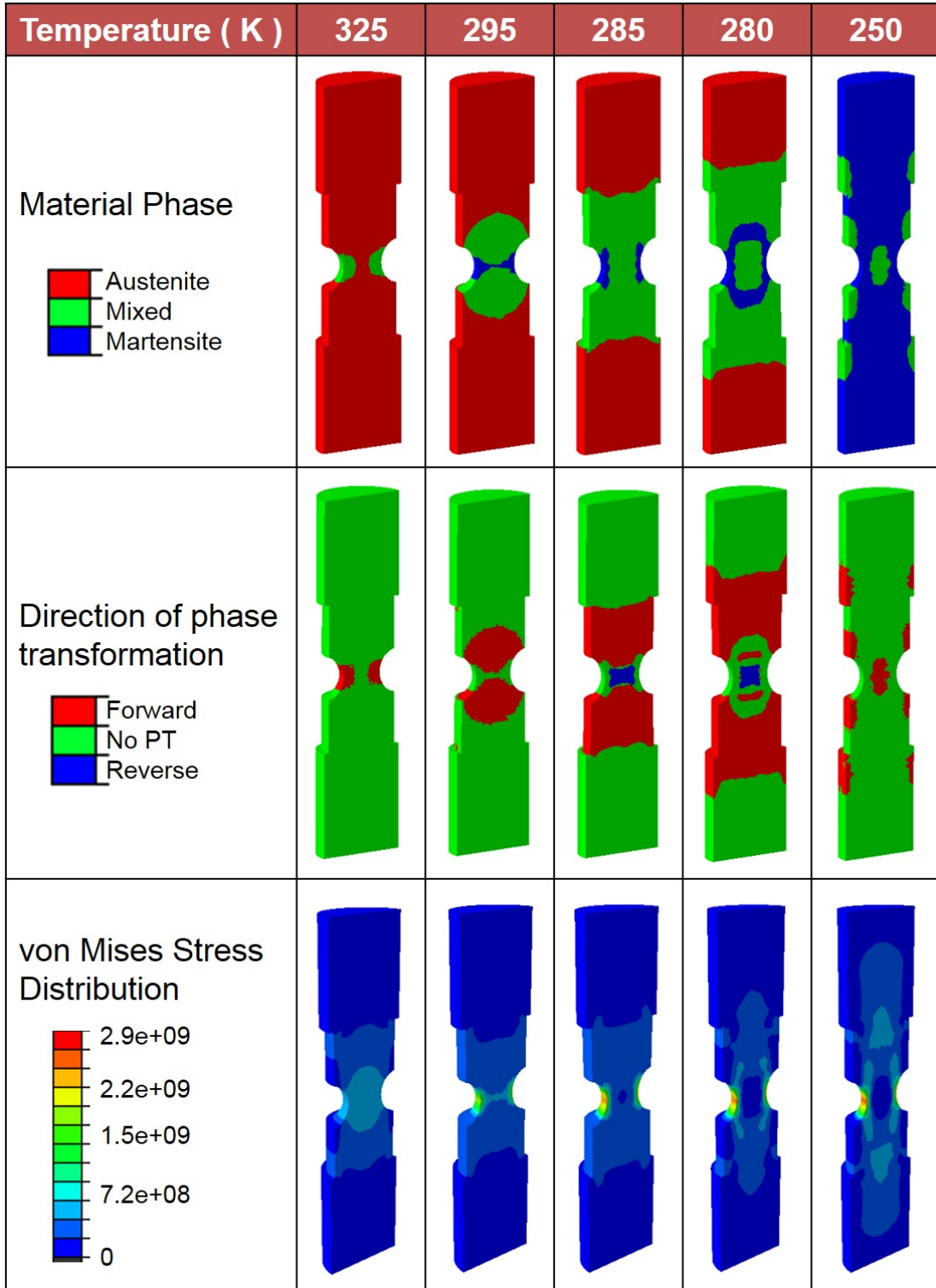
Figure 2.11: Evolution of martensitic Volume Fraction, phase transformation direction, and von Mises stress for $\frac{a}{R} = 1$ specimen subjected to 200 MPa nominal stress.

reverse transformation. By tracking the local von Mises stress-temperature state of each point, it is possible to understand why the partial reverse transformation occurs. Examining the bottom row of images in Fig. 2.11, it can be seen that as the phase transformation progresses, there is a clear change in the von Mises stress distribution. As transformation initiates, the stress tends to distribute more evenly throughout the notched region of the specimen. However, as material begins to complete phase transformation, that material then starts to take on more stress as shown at 295 K in Fig. 2.11. This trend continues through 285 K, where in the material near the notch wall supports additional load. However this additional load bearing near the notch wall leads to unloading of the central region of the notch, which in turn leads to the phase transformation reversal. This load reduction in the central region continues to exist as the specimen continues to cool.

To gain a more quantitative perspective, consider points on the notch wall and along the central axis in the plane of minimum cross section. As shown in Fig. 2.12, it can be seen that for the point along the central axis, the initial von Mises stress increases from approximately 345 K to 325 K. During this cooling, it can also be noted that the von Mises stress at the notch edge was reducing, indicating that the stress in the plane of minimum cross-section is redistributing. The stress increase in the center is a direct results of the stress reduction near the notch wall in order to maintain a balance in the load. Furthermore, as forward transformation initiates at the central point in the plane of minimum cross-section, it can be seen that the von Mises stress level reduces at the center of the specimen. Upon reaching 305 K, phase transformation completes in the center and von Mises stress starts to increase. However, at approximately 295 K, Fig. 2.11 shows that additional material near the notch that is above and below the plane of minimum cross-section completes phase transformation, thereby allowing for a reduction in von Mises stress at this point to levels similar to the initial load due to a return to elastic behavior. Furthermore, as additional material completes forward phase transformation, this leads the von Mises stress at the central point to reduce further. This additional reduction in von Mises stress becomes so significant by 288 K that the von Mises stress level causes the local von Mises stress-temperature state to drop below the A_S curve, leading to the reverse transformation noted from Fig. 2.11. The local von

Mises stress-temperature state at the point at the center of the plane of minimum cross-section remains below the A_S curve until 275 K, and forward transformation of the material point along the central axis in the plane of minimum cross-section does not start until 265 K.
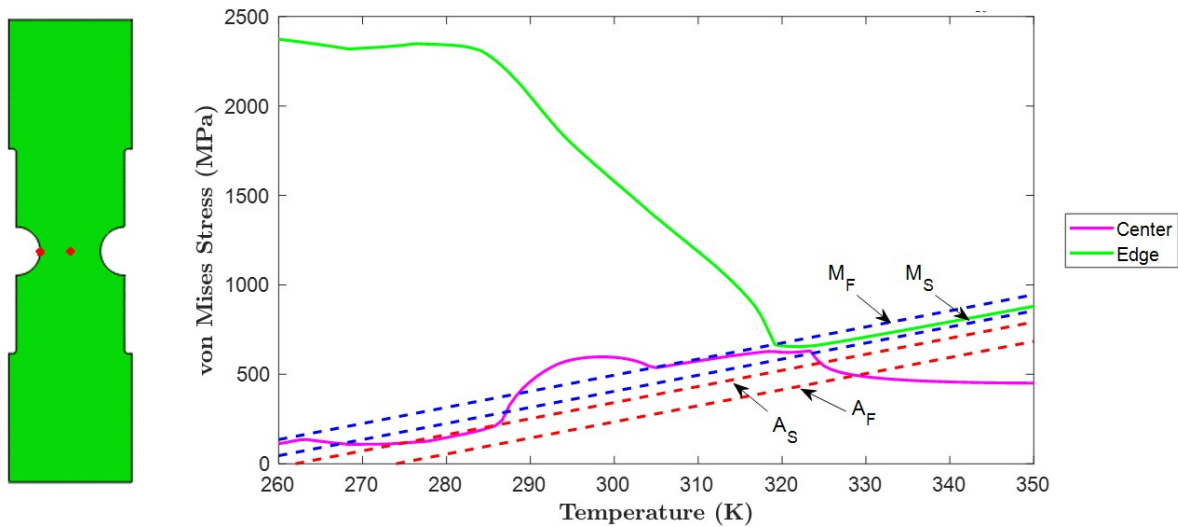
Figure 2.12: Plot of von Mises stress-temperature state of point on plane of minimum cross-section at edge and along central axis for the $\frac{a}{R} = 1$ specimen during cooling from 350 K to 260 K, as indicated by specimen to side. Overlayed lines represent lines from phase diagram.

In contrast, tracking the local von Mises stress-temperature state at a point on the edge of the notch shows a dramatically different behavior between 350 K and 260 K. From linear elastic analysis, it is expected that the initial von Mises stress at the edge should be higher than the stress for a material point removed from the edge. This is indeed confirmed by looking at the stress levels at 350 K in Fig. 2.12. As the phase transformation progresses at the edge of the specimen, it can be seen that the von Mises stress at the edge reduces, indicating a redistribution of stress throughout the cross-section of the specimen. Indeed, this stress redistribution can be seen to cause the increase in von Mises stress at the center point from 345 K to 325 K, as mentioned previously. However, once the material at the edge completes forward transformation and starts to behave elastically

again, it can be seen that the stress at the edge starts to shoot up dramatically in order to offset the reduction in stress noted at the center and which can also be seen throughout the entire plane of minimum cross-section as discussed next.
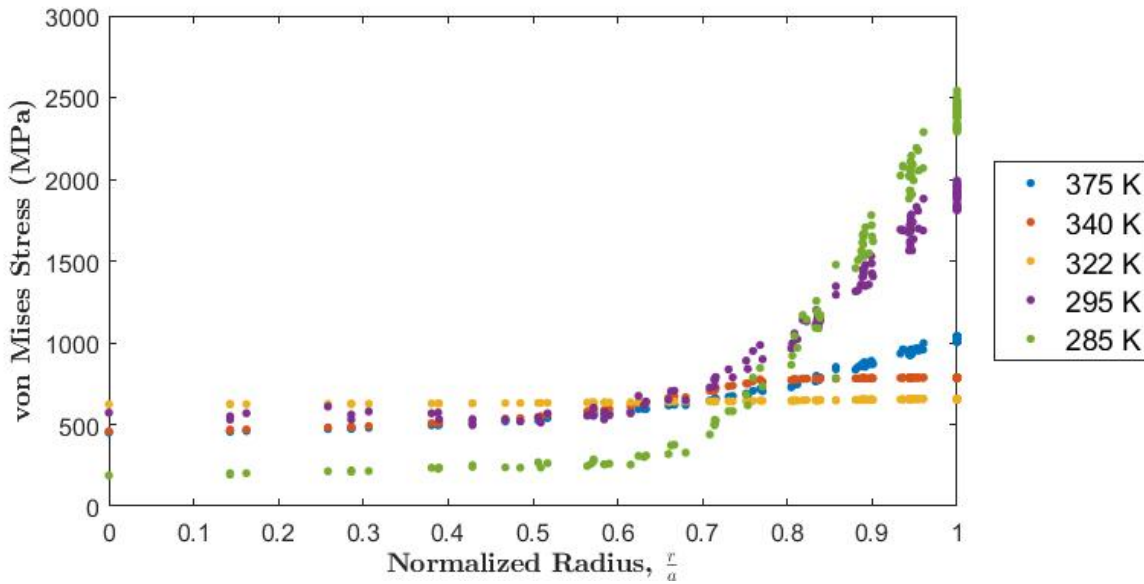
Figure 2.13: Evolution of von Mises stress during cooling from 375 K to 285 K in $\frac{a}{R} = 1$ specimen.

Looking at the von Mises stress throughout the plane of minimum cross section, not just at the center and edge, can give a better understanding of how the stress redistributes as a function of temperature throughout the specimen. As shown in Fig. 2.13. the von Mises stress at 375 K is similar to what would be expected through the plane of minimum cross section for an elastic material. By 340 K, phase transformation has started near the notch wall which initiates some stress redistribution in the plane of minimum cross-section. Furthermore, due to phase transformation, the stress redistributes such that it is approximately equalized throughout the plane of minimum cross-section at 322 K. This corresponds to when forward phase transformation is progressing throughout the entire plane of minimum cross-section, as shown in Fig. 2.14. However, by 295 K,
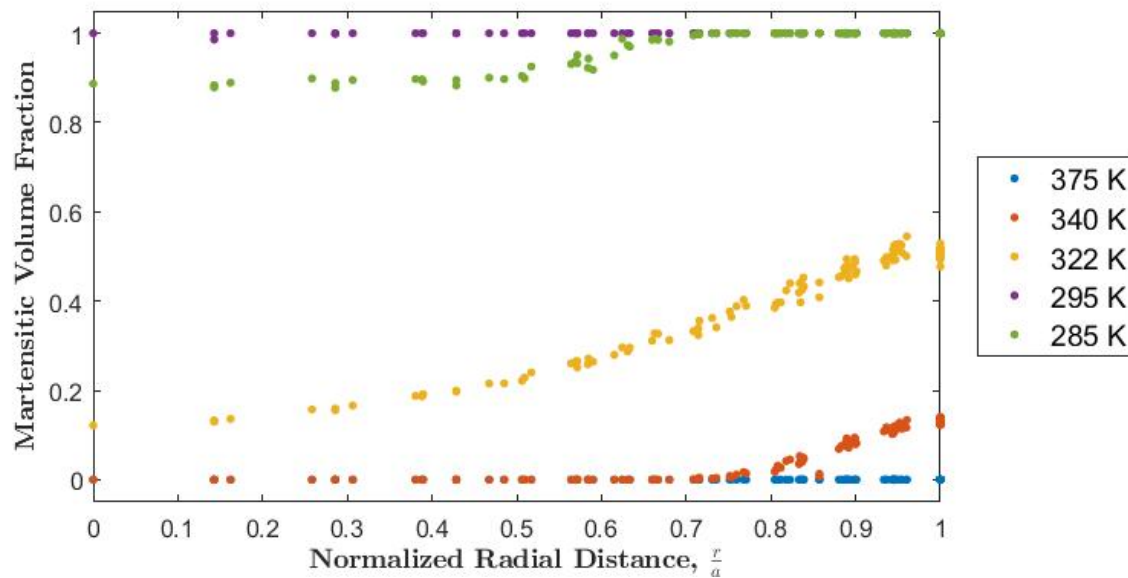
Figure 2.14: Evolution of martensitic Volume Fraction during cooling from 375 K to 285 K in $\frac{a}{R} = 1$ specimen.

the material in the plane of minimum cross-section as well as surrounding material has completed forward transformation and behaves elastically, thereby returning to an elastic stress distribution, which causes a reduction in von Mises stress for material closer to the central axis. As more material above and below the plane of minimum cross section completes forward transformation, the von Mises stress near the central axis continues to decrease, and is so significant that reverse transformation initiates by 285 K, as indicated in Fig. 2.12 and further verified through approximately 60% of the radial distance according to Fig. 2.14.

Returning to the entire spectrum of notch acuities considered, it is possible now to better understand the reason for the differences in the martensitic volume fraction evolution. Specifically, as examined for the notched cylindrical bar with a notch acuity of 1, it was found that the stress redistribution was responsible for the partial reversal of phase transformation. Therefore, it can be postulated that the difference in phase transformation behavior shown in Fig. 2.10 is due to stress redistribution during phase transformation, and this can indeed be seen from Fig. 2.15. While in

Notch Acuity, $\frac{a}{R}$	10	1.25	0.25
Near Forward Transformation Initiation (295 K)			
Part Way through Phase Transformation (265 K)			

S, Mises
(Avg: 75%)
+1.500e+09
+1.375e+09
+1.250e+09
+1.125e+09
+1.000e+09
+8.750e+08
+7.500e+08
+6.250e+08
+5.000e+08
+3.750e+08
+2.500e+08
+1.250e+08
+0.000e+00
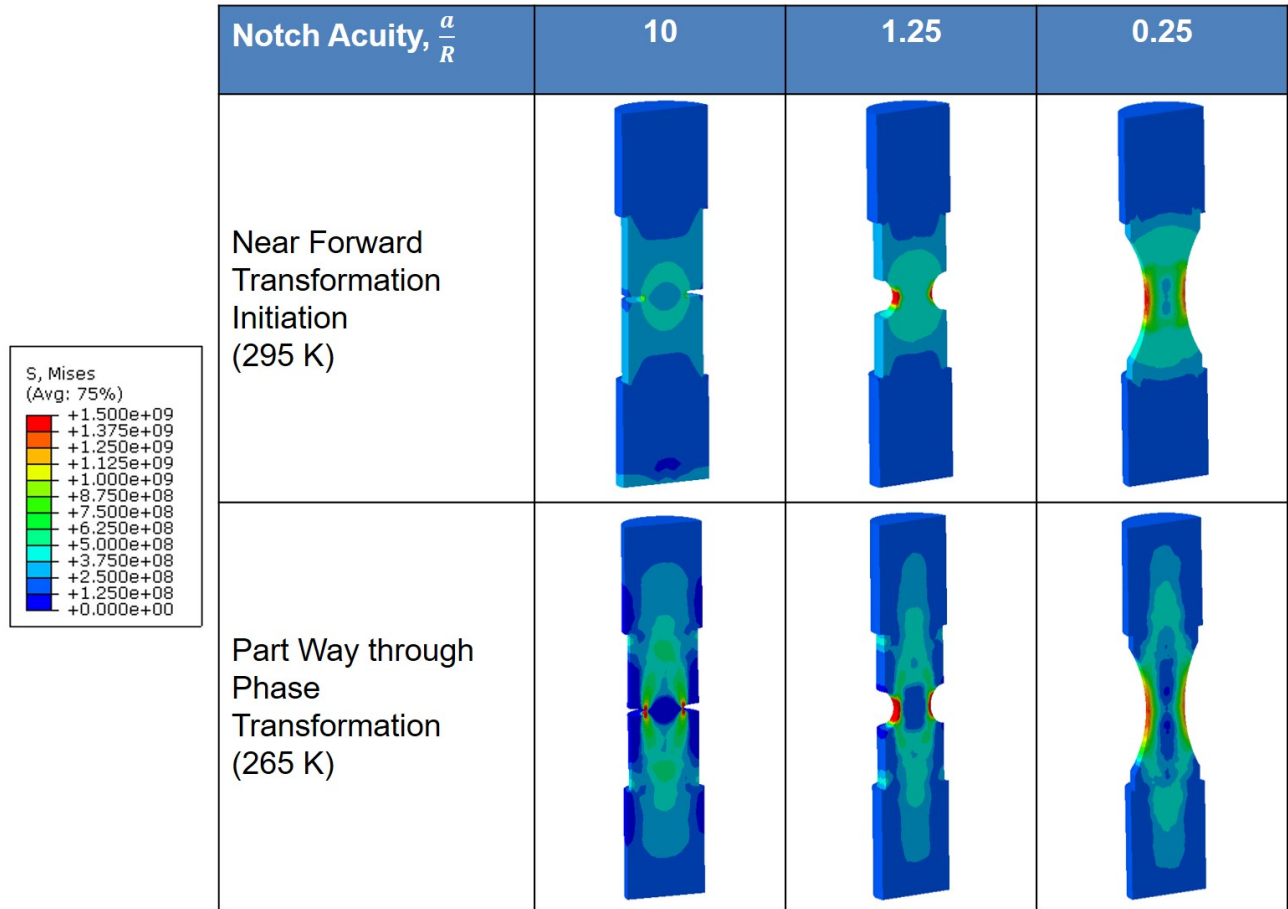
Figure 2.15: Comparison of von Mises stress during forward transformation for various specimens subjected to 200 MPa nominal stress.

austenite, the material behaves elastically and therefore the von Mises stress distributions correspond to the typical von Mises stress distribution in an elastic medium near a stress concentration. However the non-linear behavior of these SMA notched cylindrical bars can be clearly seen by examination of stress distributions shown in Fig. 2.15. In particular, it can be seen that the von Mises stress tends to distribute more evenly throughout the plane of minimum cross-section near the initiation of phase transformation at 295 K than a purely elastic response near a stress concentration. As described for the $\frac{a}{R} = 1$ specimen, this is due to a reduction in von Mises stress at the edge of the notch as it undergoes forward phase transformation, thereby requiring the surrounding

material to support more load. The elevation of von Mises stress at material points away from the notch wall in turn causes the rest of the material to start to undergo forward phase transformation. However, as the material at the wall of the notch completes forward phase transformation and starts to behave elastically, the stress at the notch wall increases dramatically, thereby leading to a reduction in stress of the material away from the notch wall. This can be clearly seen at 265 K in Fig. 2.15 which indicates that all specimens have the highest von Mises stress at the notch, but a reduction in von Mises stress as radial distance from the central axis is reduced for points close to the plane of minimum cross-section. In turn, this stress redistribution during phase transformation can be used to explain the phase transformation reversal as noted in Fig. 2.10 for the specimens in the intermediate notch acuity range.
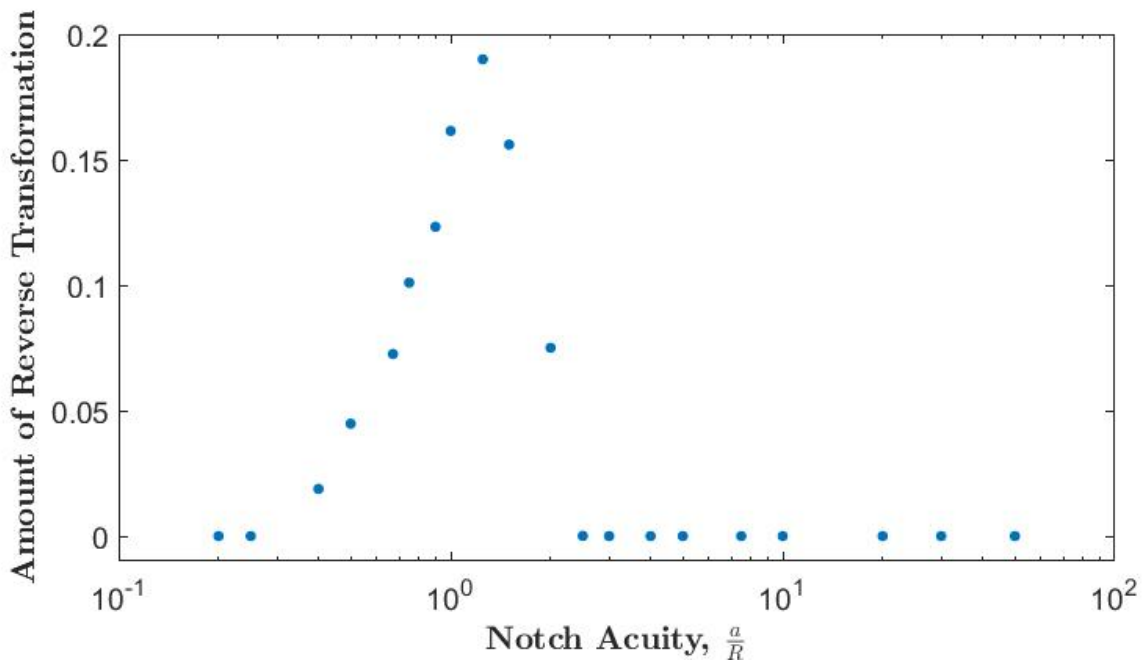
Figure 2.16: Amount of reverse transformation at a point along the central axis on the plane of minimum cross-section by notch acuity.

As mentioned in the preceding discussion for the $\frac{a}{R} = 1$ notched cylindrical specimen, the

39
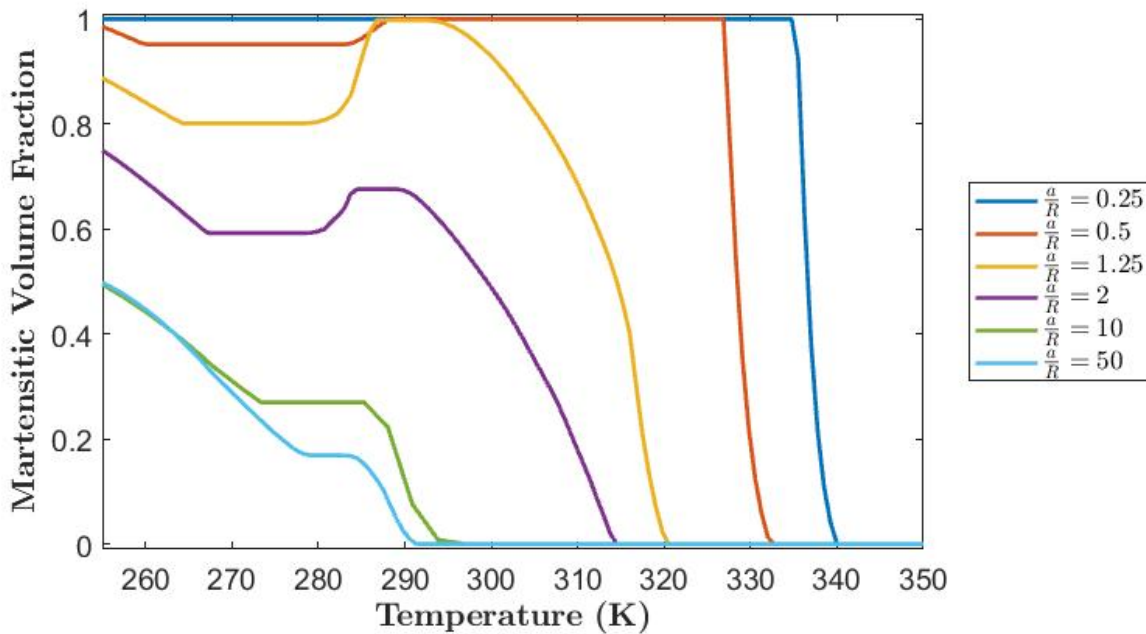
Figure 2.17: Martensitic Volume Fraction at center of multiple specimens as a function of temperature.

reversal in phase transformation is due to an interplay between von Mises stress and temperature. Looking beyond the $\frac{a}{R} = 1$ specimen, it can be found that the phase transformation reversal occurs for a range of notch acuities, as indicated in Fig. 2.16. Furthermore, each notch acuity will lead to a different stress concentration, thereby leading to different stress fields in the specimens, which in turn should lead to differences in the amount of phase transformation reversal and phase transformation temperatures. Indeed, as shown in Fig. 2.16, the martensitic volume fraction may reduce by as much as 18% for a point along the central axis and on the plane of minimum cross-section. Also, as shown in Fig. 2.17, it is shown that forward transformation at the point on the central axis and along the plane of minimum cross section initiates at different temperatures depending on the notch acuity. As expected, for low notch acuities, the stress is more distributed throughout the plane of minimum cross section, leading to higher forward transformation start temperatures compared to high notch acuity specimens which have lower von Mises stress at the center. Then
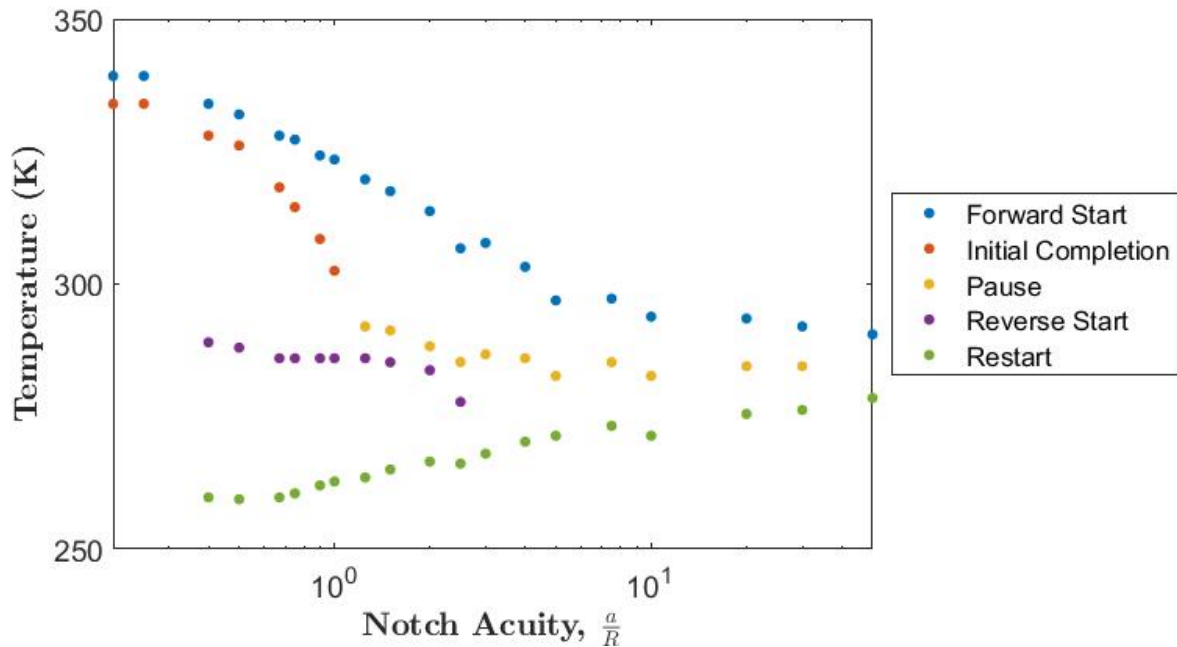
Figure 2.18: Temperature at which transformation initiates, pauses, reverses, and continues at center of specimen.

for notched specimens with notch acuities of 1.25 or less, forward phase transformation appears to complete, where as notched specimens with higher acuities do not initially complete phase transformation. It is interesting to note though, that all specimens with a notch acuity greater than 0.5 appear to reach an initial plateau in forward transformation, regardless of notch acuity. This is indicative of the von Mises stress reducing in the center of all specimens such that forward transformation completes or pauses. Upon continued cooling, Fig. 2.17 indicates that the martensitic volume fraction reduces only for intermediate notch acuities (as identified previously), indicating that they undergo reverse phase transformation in the center of the specimens. Finally, Fig. 2.17 indicates that all specimens which initially do not complete phase transformation or have undergone some level of phase transformation reversal will continue to undergo forward transformation once the temperature reduces far enough to overcome the reduction in von Mises stress which paused or reversed the phase transformation. These initiation, initial completion or forward transformation

41

pause, reverse transformation initiation, and forward transformation restart temperatures are shown in Fig. 2.18 for all specimens considered. It should be noted that while the preceding results and discussion have all focused on the phase transformation behavior during cooling, similar results have also been obtained during heating in which reverse transformation is similarly paused and reversed for the intermediate notch acuity range.

As mentioned previously, the phase transformation only occurs within a range of notch acuities, specifically between appoximately $\frac{a}{R} = 0.4 - 2.5$. This appears to be due to a trade-off between the effects of the notch acuity and the phase transformation properties. As shown in Fig. 2.15, the phase transformation causes all notch acuities to have a net reduction in von Mises stress in the center of the plane of the minimum cross-section. Nevertheless, for small notch acuities, the effective stress distribution is not significantly affected, for which the phase transformation has been shown to propagate through the plane of minimum cross-section and then expand above and below this plane. Therefore, due to this propagation method, the von Mises stress in the center is not able to drop so low that phase transformation occurs. In contrast, for high notch acuities ($\frac{a}{R} > 2.5$), the initial stress distribution is in a spherical shape touching the notch wall in the plane of minimum cross-section and then going above and below. Accordingly, the phase transformation propagates along this spherical stress distribution. In turn, as the phase transformation completes in this spherical distribution, it leads to a reduction in von Mises stress in the center of the plane of minimum cross section, which pauses the forward phase transformation. For intermediate notch acuities, a mixture of these stress distributions is present, which means that initially the intermediate notch acuities will try to propagate the phase transformation through the plane of minimum cross-section. However, as mentioned previously, when the phase transformation completes near the notch above and below the plane of minimum cross-section, the von Mises stress at the center of the plane of minimum cross-section reduces (as noted for high notch acuities) so far that phase transformation reversal initiates. At this point, the intermediate notch acuity specimens behave more similar to the high notch acuity specimens and forward phase transformation does not resume until the temperature reduces far enough to overcome the von Mises stress reduction.

42

An additional effect of the stress redistribution is a significant change in the triaxiality through-out the specimen. As noted in Ch. 1, triaxiality is defined as the ratio between the hydrostatic stress and an equivalent stress, which is typically taken as the von Mises stress (see Eq. 1.1). Tri-axiality has also been used as an indicator of failure. Therefore, for purposes of understanding how the stress redistribution during phase transformation may affect failure, it is useful to consider the evolution of triaxiality. Take the $\frac{a}{R} = 1$ specimen for example, as shown in Fig. 2.19. In this figure it can be seen that after loading and up through the beginning of transformation, the triaxiality follows the standard elastic triaxiality distribution. However as stress redistribution causes phase transformation reversal, it can be seen that the triaxiality drops down along the central axis in the plane of minimum cross-section of the specimen. Upon further cooling, although it seems like the triaxiality along the central axis of the plane of minimum cross-section recovers slightly, it can be noted that the triaxiality in regions above/below the plane of minimum cross-section increase drastically.

A deeper dive into the values at certain key points of interest shows that indeed the triaxiality does vary significantly during phase transformation. As shown in Fig. 2.20, the triaxiality at the notch wall in the plane of minimum cross-section does show some slight variation during phase transformation, however after phase transformation completes in this region, the triaxiality appears to recover to the original value. On the other hand, the triaxiality along the central axis in the plane of minimum cross-section and above/below the plane of minimum cross-section show significant variation due to the phase transformation. As transformation along the central axis in the plan of minimum cross section initially completes, the triaxiality increases (which can lead to interesting results as will be noted in Ch. 3). However then as phase transformation reversal initiates, the triaxiality become negative, indicating a compressive hydrostatic stress. On the other hand, for the point along the central axis but above the plane of minimum cross section, the phase transformation leads to a significant increase in the hydrostatic stress due to the phase transformation. Such significant rises in triaxiality can have direct impacts on fracture and can partially explain the fracture of notched specimens during phase transformation as noted by Olsen [51].
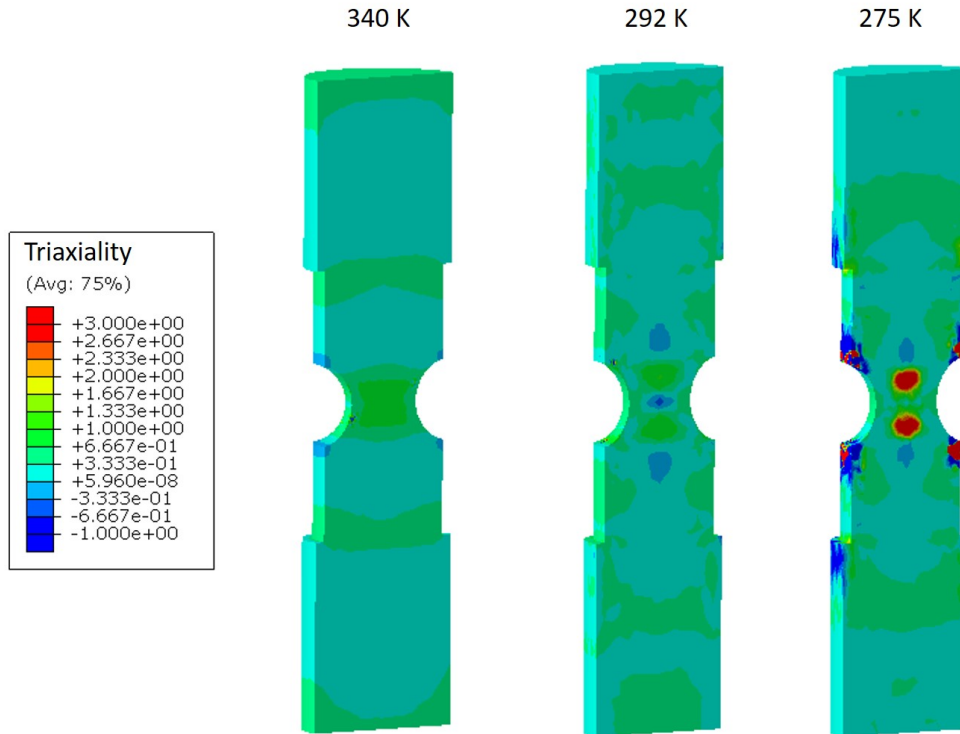
Figure 2.19: Triaxiality in the $\frac{a}{R} = 1$ specimen during cooling.

2.4 Conclusion

As the functional lifetime of a SMA component is considered, the numerical results obtained in this chapter are useful in understanding how a stress concentration will affect the phase transformation in SMA members during each phase transformation cycle. Through the use of numerical simulations, it has been shown that stress redistribution during phase transformation in SMAs can lead to very unique consequences. Through analysis of notched cylindrical SMA bars with varying notch acuities subjected to pseudoelastic loading, it was demonstrated that the phase transformation will propagate in different methods, changing from progagating through the plane of minimum cross-section before spreading up and down for low notch actuities, to propagating spherically for high notch acuities. Such phase transformation patterns for pseudoelastic loading follow the stress contour patterns, however during phase transformation, stresses will tend to redistribute to areas that have completed phase transformation as load level increases due to the limited load bearing
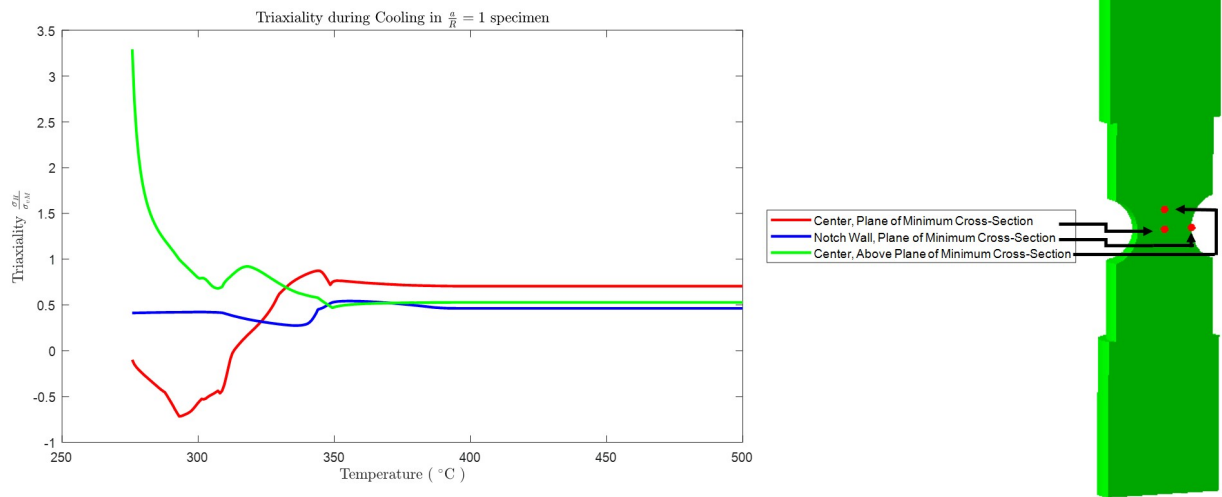
Figure 2.20: Triaxiality during cooling for 3 points in the $\frac{a}{R} = 1$ specimen.

capacity of regions still undergoing phase transformation.

For notched cylindrical SMA bars subjected to thermal actuation, the results indicate that, similar to the pseudoelastic results, the phase transformation propagation method is also dependent on the notch acuity. The change from a linear to a spherical phase transformation propagation pattern is in the range of notch acuity ratios between 0.5 and 2. However in this region, the stress redistribution that occurs due to phase transformation, coupled with the competing phase transformation propagation mechanisms can lead to phase transformation reversal. Indeed results for the various notch acuities analyzed indicate up to 18% phase transformation reversal could be obtained at a notch acuity of $\frac{a}{R} = 1.25$. Furthermore, analysis of the triaxiality evolution during phase transformation indicates that for intermediate notch acuities, the stress redistribution can lead to both the elevation as wall as the reduction in triaxiality through the specimens, which can have significant impacts on the fracture in notched cylindrical SMA bars.

3. EXPERIMENTAL VALIDATION OF THE EFFECT OF STRESS REDISTRIBUTION DURING PHASE TRANSFORMATION IN NOTCHED CYLINDRICAL SHAPE MEMORY ALLOY BARS [1]

The numerical results in Ch. 2 provide some valuable insight into the phase transformation of a SMA component within a single phase transformation cycle from a theoretical perspective. However, to quote Richard Feynman, "It doesn't matter how beautiful your theory is, it doesn't matter how smart you are. If it doesn't agree with experiment, it's wrong." Therefore, it is necessary to conduct experiments in order to provide some level of validity to the numerical results previously obtained. In this spirit of validation, the following chapter presents some experimental results and provides comparison of these experimental results to the numerical results presented in Ch. 2. Therefore, the following chapter is presented as follows. First, Sec. 3.1 discusses the experimental specimens and testing procedures utilized to test notched cylindrical SMA bars. Section 3.2 presents experimental results for pseudoelastic loading paths and draws comparisons with the numerical results from Sec. 2.2. Section 3.3 presents experimental results for thermal actuation loading paths and provides a comparison to numerical results shown in Sec. 2.3. Finally, Sec. 3.4 presents neutron diffraction experiments which enabled quantitative validation of the material crystallographic state during thermal actuation.

3.1 Experimental Approach

In order to validate some of the numerical results presented in Ch. 2, a number of experimental tests were run on specimens with two different notch geometries, along with a smooth cylindrical dogbone. The smooth cylindrical dogbone was required for model calibration purposes. The specimens were 46.5mm tall, with a 4mm radius in the grip region, 3.5mm radius in the initial

---

radial reduction region, and a minimum radius of 1.95mm in the plane of minimum cross-section. The notch sizes were based on the $\frac{a}{R} = 0.5$ and the $\frac{a}{R} = 2.5$ numerical specimens and therefore the notch radius was adjusted accordingly (3.9mm notch radius for the $\frac{a}{R} = 0.5$ specimens and 0.78mm notch radius for the $\frac{a}{R} = 2.5$ specimens). Sample specimens are shown in Fig. 3.1. All specimens used for experimentation at TAMU were machined out of a $Ni_{50.8}Ti_{49.2}$ bar via conventional grinding and the outer surface was left in the conventionally ground finish condition.

In addition, the gauge region of the specimens was coated in white spray paint, followed by speckling with black spray paint. This surface coat was needed in order to allow for determination of the 3D strain fields via digital image correlation (DIC) for both the smooth cylindrical dogbone as well as the $\frac{a}{R} = 0.5$. Due to the size of the notch in the $\frac{a}{R} = 2.5$ specimen, reliable DIC strain fields could not be properly obtained, however optical extensometry was also utilized for all specimens to determine the axial and radial extension of various points in each specimen. Optical extensometry was performed via a custom script written utilizing LabView Vision Assistant $^{®}$, which tracks the location of the top and bottom of the notch, and left and right edges of the plane of minimum cross section. The locations tracked are shown in Fig. 3.2 on a $\frac{a}{R} = 0.5$ specimen. Furthermore, these optical extensometry results were validated by comparing the axial extension based on the distance between the grip regions to a laser based axial strain measurement which utilized reflective tags placed on the specimens at the bottom of the grip regions.

All experiments were conducted on a MTS Insight electromechanical test frame. The test specimens were loaded into custom threaded grips in order to prevent slipping. In order to validate the pseudoelastic simulations, all pseudoelastic experiments were run at room temperature by increasing and decreasing the axial strain at a strain rate of 10^{-3} /s, utilizing the notch height as the gauge length, up to a maximum nominal stress level of 200 MPa based on the radius of the top of the specimens. Based on Saint Venant's principle, this region at the top/bottom of the specimen, removed from the notched region should have a more uniform stress distribution. The nominal stress level of 200 MPa based on the radius at the top of the specimen results in a maximum average nominal stress of 680 MPa based on the radius of the plane of minimum cross section. It is acknowledged

Notch Acuity, $\frac{a}{R}$	2.5	0.5	Smooth
Geometry			
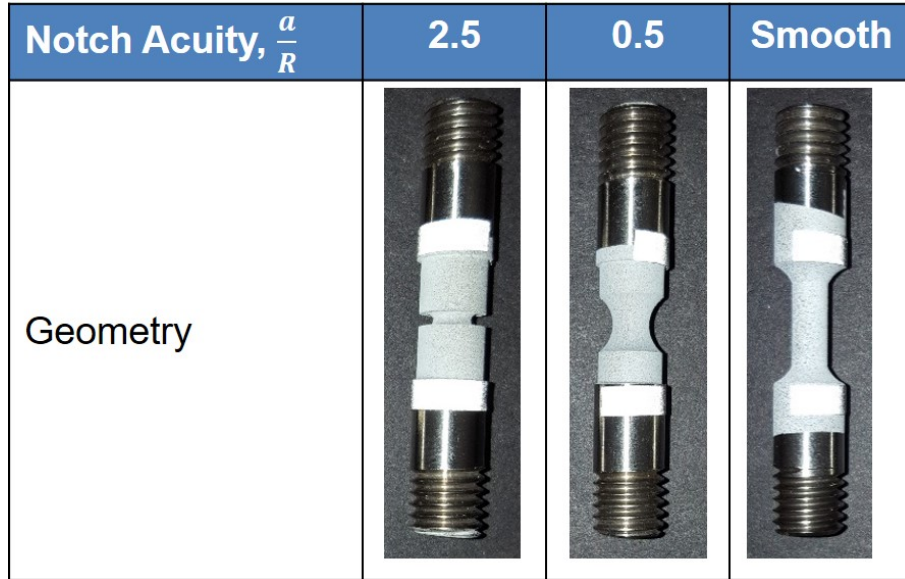
Figure 3.1: Image of the three types of experimental specimens.

that, as shown in Sec. 2.2, the stress distribution in the plane of minimum cross-section is non-uniform, however since the primary region of interest is the behavior within the notched region, the response under pseudoelastic loading will be based on this average stress value in the plane of minimum cross-section.

For the thermal actuation experiments, heating of the specimens was accomplished by inductively heating the grips and allowing the heat to conduct through the specimens. Upon reaching the desired maximum temperature, the inductive heater was turned off and the specimens were allowed to convectively cool by transferring the heat to the ambient air (approximately 298 K). It was not possible to utilize a thermal chamber which could accommodate cooling below ambient temperature since the thermal chamber would obstruct the ability to utilize two cameras as needed for 3D DIC. The temperature of each specimen was obtained via thermocouples attached at 3 locations on each specimen (in the top grip region, in the bottom grip region, and at the center of each specimen). A custom Labview VI ® was used to record the measured temperatures and trigger the induction heater to turn on and off as needed for the thermal sweeps. While the data recorded does show a thermal gradient throughout the specimen during heating due to conduction, the experi-
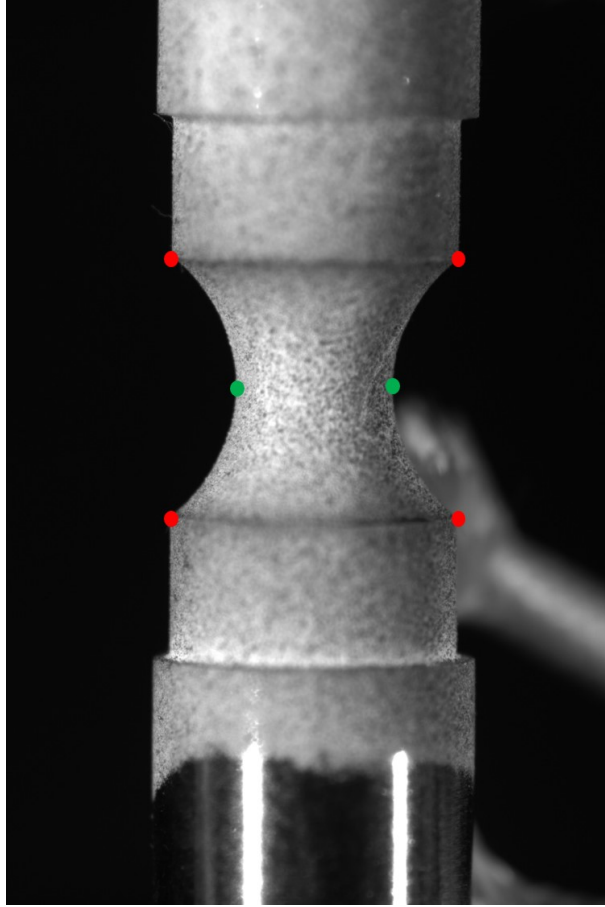
Figure 3.2: Locations of optical measurement points. Red points indicate notch axial extension measurement points and green points indicate notch radial extension measurement points. Central thermocouple shown coming from behind specimen.

ments did show that the temperature throughout the specimen during cooling was nearly uniform, in particular in the temperature ranges where phase transformation occurred, thereby validating the assumption of uniform temperature made for the numerical simulations. The specimens were pre-loaded to 30 N at $1x10^{-3}\frac{mm}{mms}$ using the notch length as the gauge length. Upon reaching the pre-load, the temperature was increased to 400 K and then the load was increased to the desired test load at $1x10^{-3}\frac{mm}{mms}$, while maintaining the temperature constant. After reaching the test load of 9975 N (corresponding to 65% of the ultimate tensile load at 425 K for all notched geometries), the temperature was cycled from 400 K to 310 K while maintaining a constant load. It should be noted

that the numerical load of 200 MPa on the surface leads to the same total load as that applied in the experiments. Also, this load was selected in order to ensure some level of transformation prior to room temperature, while minimizing risk of specimen failure (similar experiments at 14000 N, or 90% of the ultimate tensile loads, failed during the first cooling cycle).

In addition to the pseudoelastic and thermal actuation experiments conducted at Texas A&M University, additional thermal actuation experiments were conducted at Oak Ridge National Laboratory utilizing specimens were also machined of out $Ni_{50.3}Ti_{29.7}Hf_{20}$. The primary reason for the use of these additional specimens was in order to allow for complete forward and reverse phase transformation due to the elevated phase transformation temperatures of $Ni_{50.3}Ti_{29.7}Hf_{20}$. As described above, thermal actuation experiments at Texas A&M University were conducted without the use of a thermal chamber, meaning that the lowest possible temperature for the specimens was room temperature. However as such, $Ni_{50.8}Ti_{49.2}$ was unable to complete forward transformation due to an M_F temperature of approximately -40 $\deg$C. Therefore, these additional experiments utilizing $Ni_{50.3}Ti_{29.7}Hf_{20}$, which has an M_F temperature of approximately 160 $°C$ allow for the full forward and reverse transformation to occur. By performing these experiment on $Ni_{50.3}Ti_{29.7}Hf_{20}$ at Oak Ridge National Laboratory, it was possible to characterize the material crystal structure using neutron diffraction.

3.2   Experimental Validation under Pseudoelastic Loading Conditions

The numerical results presented in Sec. 2.2 clearly suggest that the presence of a stress concentration such as a notch can have a profound impact on the evolution of the phase transformation in a SMA. In order to prove such impacts exist, pseudoelastic experiments were also performed. It is well known that introduction of a notch in a material can lead to notch strengthening, while at the same time leading to a stress concentration. The effect of this notch strengthening can be seen in Fig. 3.3, which presents experimental results for pseudoelastic tests at room temperature for the three different geometries. In the following plots, the nominal stress is based on the area of minimum cross-section (which is the same for all specimens) in order to allow for a direct comparison without taking into account the effect of the stress concentrations (the effect of which was

examined further in Sec. 2.2). Also, in Fig. 3.3, the strain measurement is taken from the laser tags which are placed at the same location on all specimens (at the top and bottom of the grip region as shown in Fig. 3.1). Figure 3.3 shows that as the notch size is reduced from smooth to $\frac{a}{R} = 0.5$ to $\frac{a}{R} = 2.5$, the stress required to initiate phase transformation is increased, hence relating back to the notch strengthening effect. Furthermore, in this averaged strain measurement, it appears that the $\frac{a}{R} = 2.5$ may not transform. Indeed, in this averaged sense, it appears that the amount of phase transformation is greatest for the smooth, but then reduces for the $\frac{a}{R} = 0.5$, and is even lower for the $\frac{a}{R} = 2.5$. However, if instead the strain measurement is calculated based on the strain of the notched region, as shown in Fig. 3.4, it can be seen that all three geometries present some amount of transformation. It is worth noting that the $\frac{a}{R} = 0.5$ specimens have less axial strain in the notch based measurement as well as the averaged measurement then the smooth specimen, where as the $\frac{a}{R} = 2.5$ specimens have more transformation than either the $\frac{a}{R} = 0.5$ or the smooth in the notched based measurement but less in the averaged measurement. Furthermore, the radial strain in the center of the specimens (at the area of minimum radius) was also measured and is shown in Fig. 3.5, which shows that the radius of the smooth specimen reduces the most during the forward transformation, followed by the $\frac{a}{R} = 0.5$ and then the $\frac{a}{R} = 2.5$. This result may seem counter-intuitive at first given that Fig. 3.4 shows that the $\frac{a}{R} = 2.5$ shows the highest amount of axial strain based on the notch region, however this result does agree with the numerical results which will be presented in Sec. 3.2.1. Also worth noting is that more plastic strain is generated for the $\frac{a}{R} = 2.5$ specimen based on Fig. 3.4 than the smooth or the $\frac{a}{R} = 0.5$ when going to the same nominal stress level, which also relates back to the stress concentration due to the notch.

3.2.1 Comparison of Numerical and Experimental Results for Pseudoelastic Loading

In order to validate the numerical results shown in Ch. 2, it is hereby necessary to compare the numerical results of Ch. 2 to the experimental results obtained above. As mentioned, the experimental results for strain were obtained based on both optical and laser based measurements. However, as these are not local measurements, only the averaged extension could be compared between the experimental and numerical results.
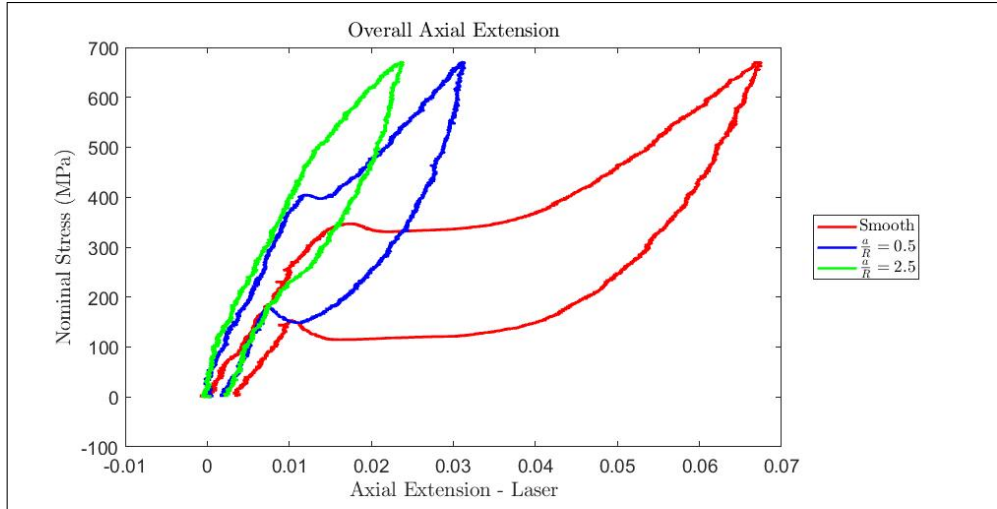
Figure 3.3: Experimental stress-axial extension plot for pseudoelastic tests on smooth, $\frac{a}{R} = 0.5$, and $\frac{a}{R} = 2.5$ specimens. Strain value based on laser tag measurement from top to bottom of specimen.
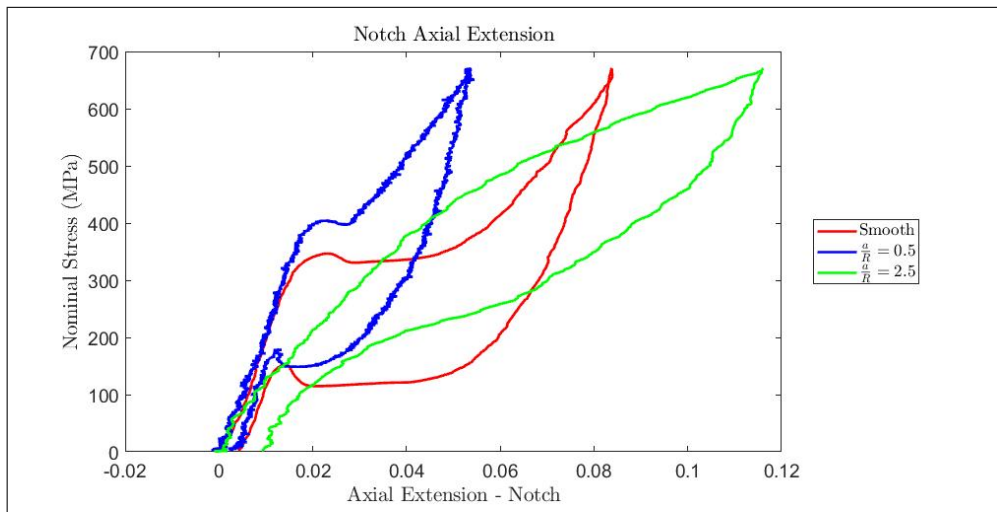
Figure 3.4: Experimental stress-axial extension plot for pseudoelastic tests on smooth, $\frac{a}{R} = 0.5$, and $\frac{a}{R} = 2.5$ specimens. Strain value based on optical measurement from top to bottom of notched region

The results of such comparison are presented in Figs. 3.6 through 3.9. From the axial measurements, it is clear that both the laser based measurements (as shown in Figs. 3.6 and 3.8) as well as the optical based axial measurements (as shown in Fig. 3.7) show good agreement between the
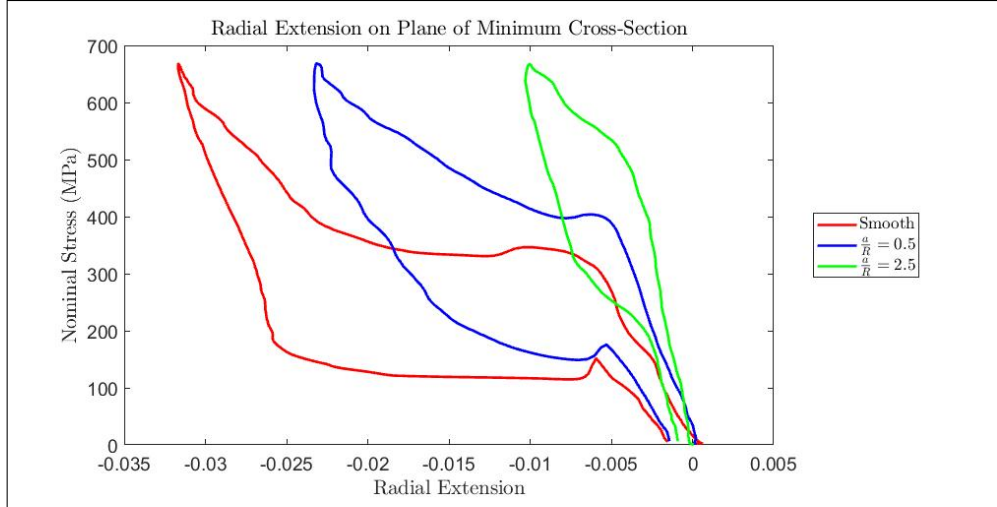
Figure 3.5: Experimental stress-radial extension plot for pseudoelastic tests on smooth, $\frac{a}{R} = 0.5$, and $\frac{a}{R} = 2.5$ specimens. Strain value based on optical measurement from left to right at center of notch (location of minimum radius).

experimental and the numerical results. Indeed, the numerical results were able to capture various non-linear phenomena as present in the notched specimens. In addition, the numerical results and experimental results also match closely for the radial extension as shown for the $\frac{a}{R} = 2.5$ specimen in Fig. 3.9. Although these results do not completely confirm the stress redistribution results as presented in Ch. 2, the close match between these experimental and numerical results in terms of the stress-extension response at multiple locations throughout the specimens suggest that the numerical results are at least partially validated.

3.3 Experimental Validation under Actuation Loading

In order to provide further credibility to the numerical simulations presented in Ch. 2, it is also necessary to attempt to experimentally validate the numerical results of Ch. 2 for thermal actuation loading conditions. To that end, multiple experimental specimens were tested under thermal actuation loading conditions. The first stage in building confidence is ensuring that the results from calibration could be well matched by numerical simulations. As shown in Figs. 3.10 and 3.11, the experimentally determined principal strain for the smooth specimen thermally cycled under 200 MPa as determined by DIC compare well with the principal strain computed from the
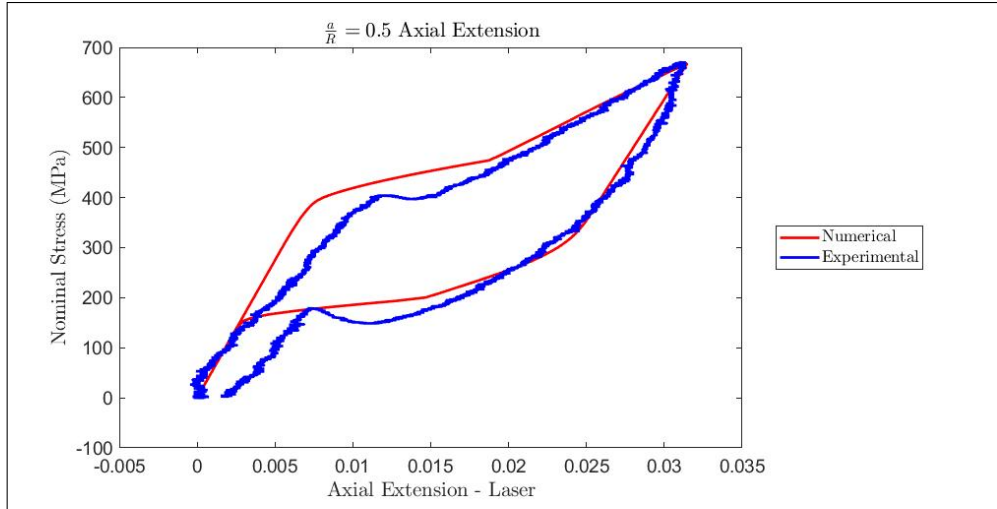
Figure 3.6: Comparison of axial extension as determined numerically and experimentally for $\frac{a}{R} = 0.5$ specimen based on laser tag measurement location.
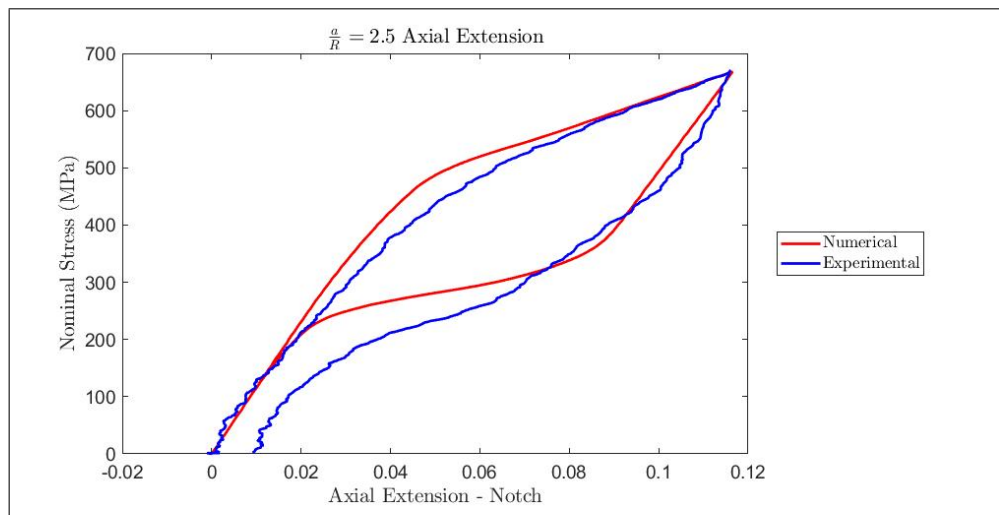
Figure 3.7: Comparison of axial extension as determined numerically and experimentally for $\frac{a}{R} = 2.5$ specimen based on optical measurement of axial notched region.

numerical simulations. Furthermore, it can also be seen in Figs. 3.12, 3.13, and 3.14 that there is good agreement between the experimental principal strain and the predicted principal strain from the numerical simulations for the $\frac{a}{R} = 0.5$ specimen. Hence, these principal strain field based comparisons help to give support to the obtained numerical results.

In addition to DIC results, optical extensometry was also used to provide feedback on the match

54
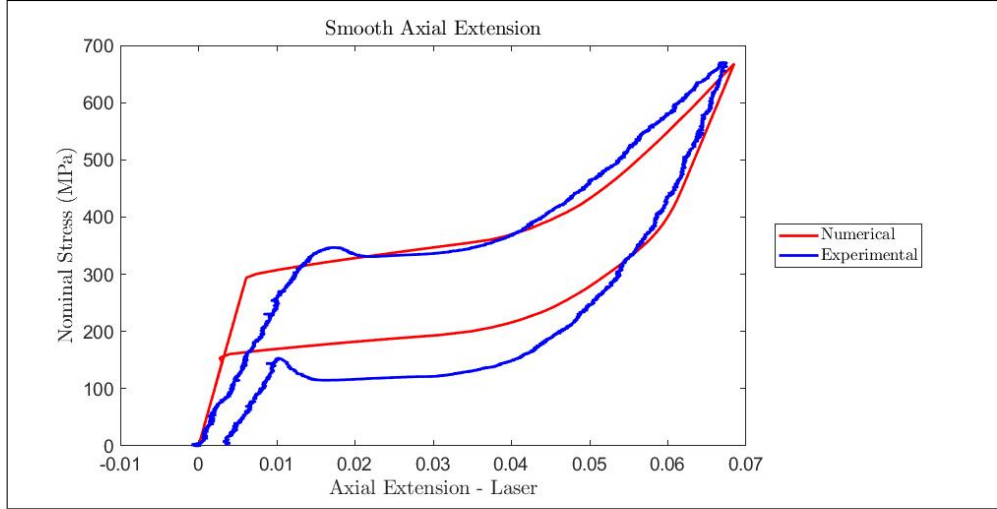
Figure 3.8: Comparison of axial extension as determined numerically and experimentally for smooth specimen based on laser tag measurement location.
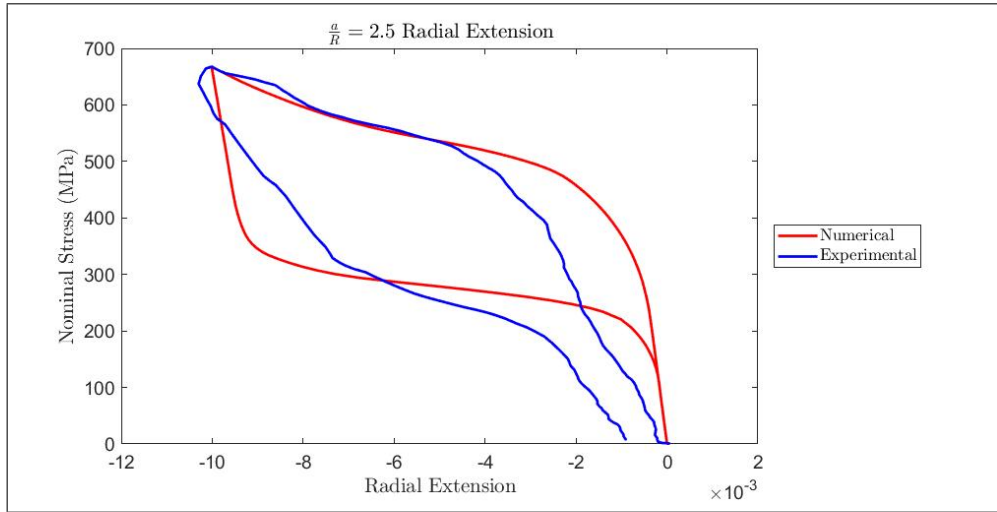
Figure 3.9: Comparison of radial extension as determined numerically and experimentally for $\frac{a}{R} = 2.5$ specimen based on optical measurement of plane of minimum cross-section.

between the numerical simulations and experimental results. The comparisons between experimental and numerical results for axial extension ($\frac{\Delta L}{L_0}$) of the notched region and radial extension ($\frac{\Delta r}{r_0}$) of the plane of minimum cross-section are shown in Figs. 3.15 and 3.16 for the $\frac{a}{R} = 0.5$ specimen, and in Figs. 3.17 and 3.18 for the $\frac{a}{R} = 2.5$ specimen. It can be noted that the the results show a two stage phase transformation in the $\frac{a}{R} = 0.5$ specimen in both the experimental and

55
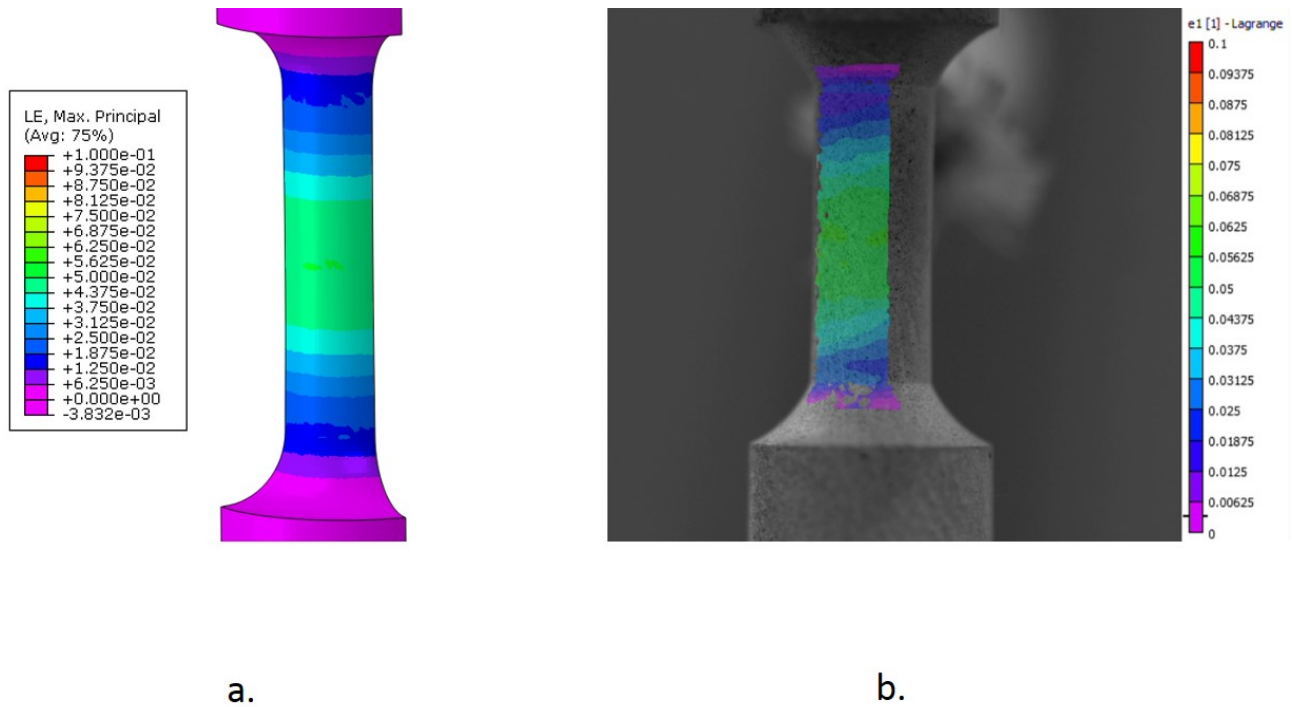
Figure 3.10: Comparison of smooth specimen under 200 MPa near start of forward transformation as captured by (a) numerical results; and (b) experimental results from DIC.

numerical results. Based on the numerical results, the inflection point corresponds to the point at which transformation has completed propagation through the plane of minimum cross-section and is now starting to spread above and below this plane. This inflection point also corresponds to the temperature at which the principal strains were obtained numerically and experimentally in Fig. 3.13. In contrast, the experimental and numerical results for the $\frac{a}{R} = 2.5$ specimen show a single continuous slope in the thermal region tested, suggesting a different phase transformation propagation as indicated previously. It should also be noted that the notch radial extension has a negative value, corresponding to the fact that the radius is contracting. The initial reduction in radius can be attributed to thermal contraction, where as the large change in radius can be attributed to crystallographic reorientation along the axial direction during forward transformation, and then returning to the higher symmetry crystal structure during reverse transformation. Unfortunately, cooling to temperatures in which the numerical simulations would suggest phase transformation reversal was

56
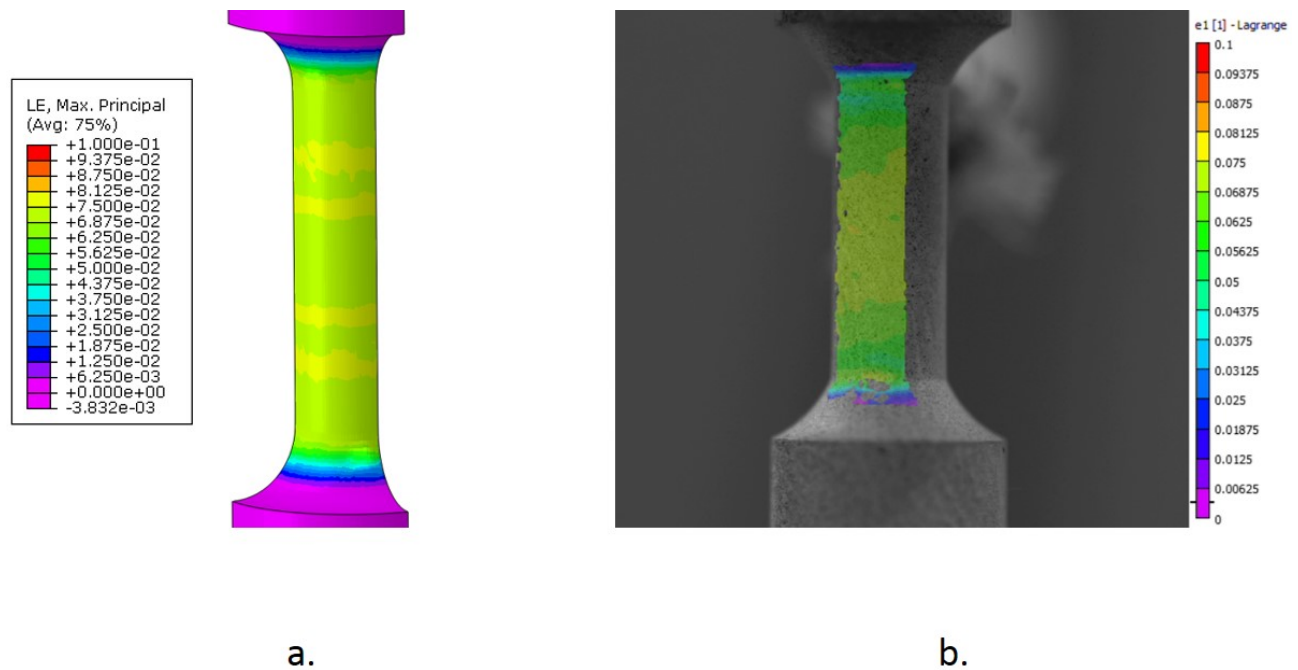
Figure 3.11: Comparison of smooth specimen under 200 MPa at end of cooling as captured by (a) numerical results; and (b) experimental results from DIC.

not achieved in these specimens due to experimental limitations previously mentioned, leading to only partial forward transformation as indicated by the lack of a plateau in the experimental results during heating. It must also be acknowledged that the experimental results show some level of plasticity which is not properly accounted for in the numerical simulations which assume no plastic strain generation. However, overall the results of this comparison between experimental and numerical results show a good match, giving additional credibility to the numerical results presented previously.

3.3.1 SEM Analysis of Fracture Surface for Specimens that Failed under Thermal Actuation

In addition to the surface level DIC and optical extensometry measurements, the stress redistribution presented in Ch. 2 suggested that the stress increased dramatically in certain areas of notched cylindrical SMA specimens and also lead to triaxiality variation, and that this increase was dependent on the notch acuity. Furthermore, it has been shown by Baxevanis et al. [46] that
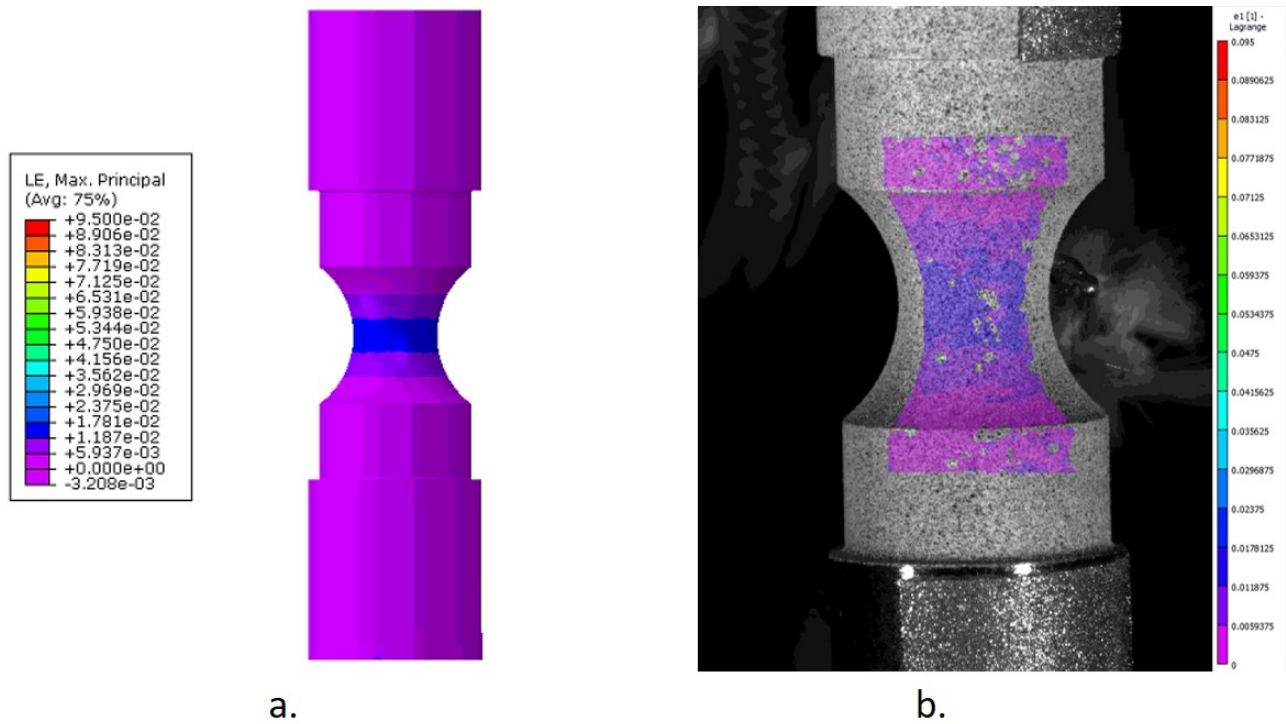
Figure 3.12: Comparison of $\frac{a}{R} = 0.5$ under 200 MPa near start of forward transformation as captured by (a) numerical results; and (b) experimental results from DIC.

notched plate specimens can fail during phase transformation at load levels well below the nominal failure load levels that either austenite or martensite can sustain. Therefore, an additional method which could suggest that the phase transformation propagates differently depending on the notch acuity would be to examine the fracture surface of notched cylindrical SMA bars with varying notch acuity.

To this end, after completion of the experiments as described in Sec. 3.3, specimens with notch acuities of both $\frac{a}{R} = 0.5$ and $\frac{a}{R} = 2.5$ were also subjected to 1150 MPa while in austenite and allowed to cool. During the forward phase transformation, specimens with both of these notch acuity ratios fractured. Some representative images of the resulting fracture surfaces for the $\frac{a}{R} = 2.5$ and $\frac{a}{R} = 0.5$ specimens are shown in Figs. 3.19 and 3.20, respectively. The fracture surface for the $\frac{a}{R} = 2.5$ specimen, shown in Fig. 3.19 clearly indicates that the fracture initiates near the notch wall on the bottom of the fracture surface and then propagates from this initiation
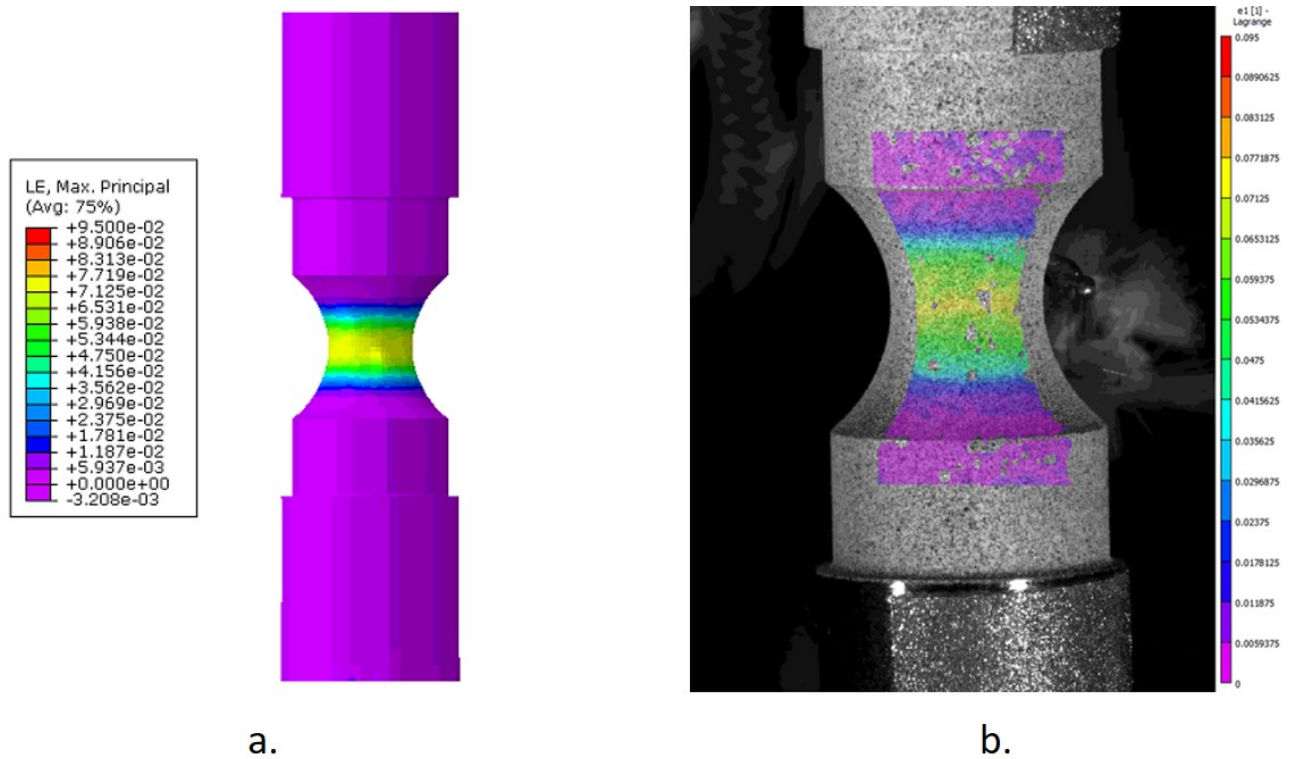
Figure 3.13: Comparison of $\frac{a}{R} = 0.5$ specimen under 200 MPa at 326 K (part way through cooling) as captured by (a) numerical results; and (b) experimental results from DIC.

site through the rest of the fracture surface. In contrast, as seen in the SEM image in Fig. 3.20, the fracture surface for the $\frac{a}{R} = 0.5$ specimen seems to indicate that fracture may have initiated near the center of the fracture surface. Indeed, it appears that the wavy patterns formed during fracture seem to propagate out radially from the center.

The difference in the fracture surface clearly indicates that differing mechanisms lead to the fracture during phase transformation. For the $\frac{a}{R} = 2.5$ specimen, the numerical results from Ch. 2 clearly indicated that the stresses will localize within the areas near the notch wall as the center of the plane of minimum cross-section starts to undergo forward phase transformation. Physically, this localization of stress would lead to an excessive stress level near the notch wall, which would lead to fracture. In turn, these SEM results shown in Fig. 3.19 clearly make sense in that fracture for the $\frac{a}{R} = 2.5$ initiated near the notch wall.

In contrast, for the $\frac{a}{R} = 0.5$ specimen, the numerical results from Ch. 2 indicate that phase
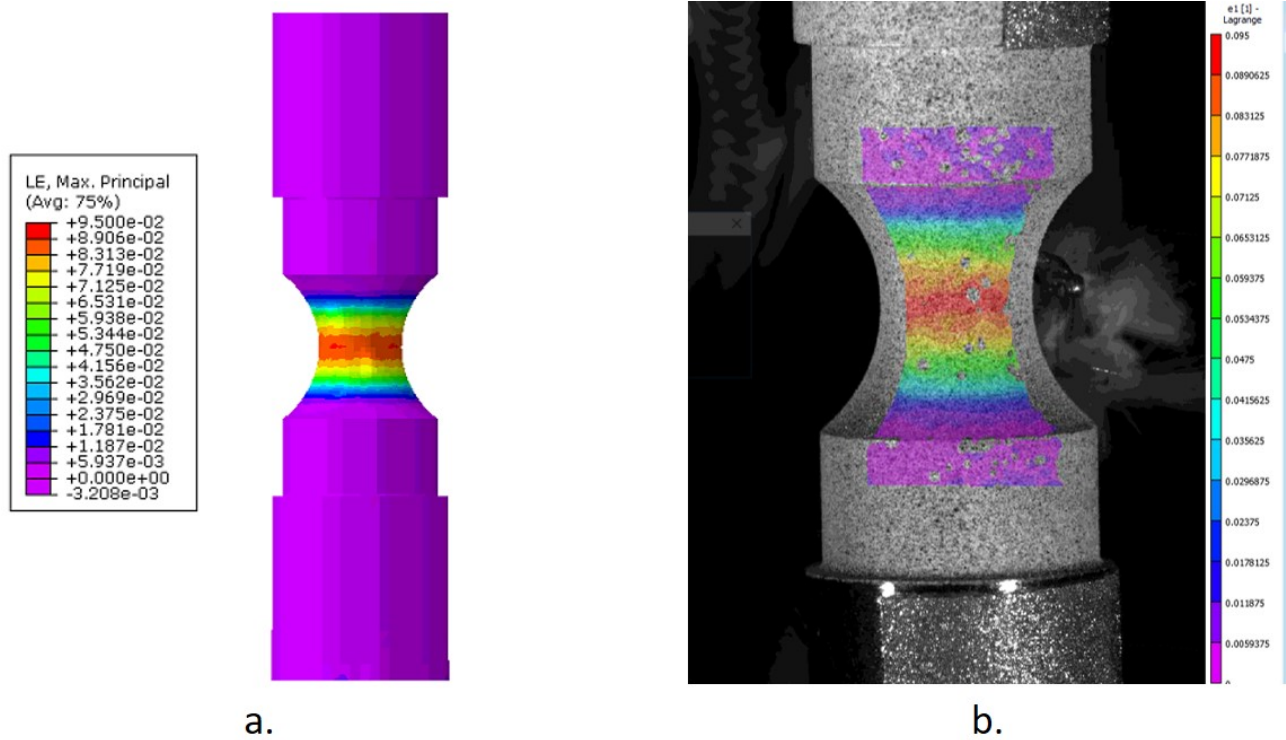
Figure 3.14: Comparison of $\frac{a}{R} = 0.5$ under 200 MPa at end of cooling as captured by (a) numerical results; and (b) experimental results from DIC.

transformation would initially complete through the the plane of minimum cross section, hence the stress localization in the notch wall would not initially build up as much as for the case of the $\frac{a}{R} = 2.5$ specimen. On the other hand, as the phase transformation progressed, the stress redistribution would lead to a significant increase in tensile hydrostatic stress in the middle of the specimen immediately prior to phase transformation reversal. In turn, this increase in tensile hydrostatic stress in the center of the plane of minimum cross section, when combined with a high level of applied stress, could lead to failure initiation in the center of the specimen, which matches the fracture surface initiation site as shown in Fig. 3.20.

3.4 Verification of Phase Transformation Reversal Utilizing Neutron Diffraction

As shown in the preceding sections, experiments performed at TAMU were able to partially validate the numerical simulations which indicate a strong dependence between phase transforma-
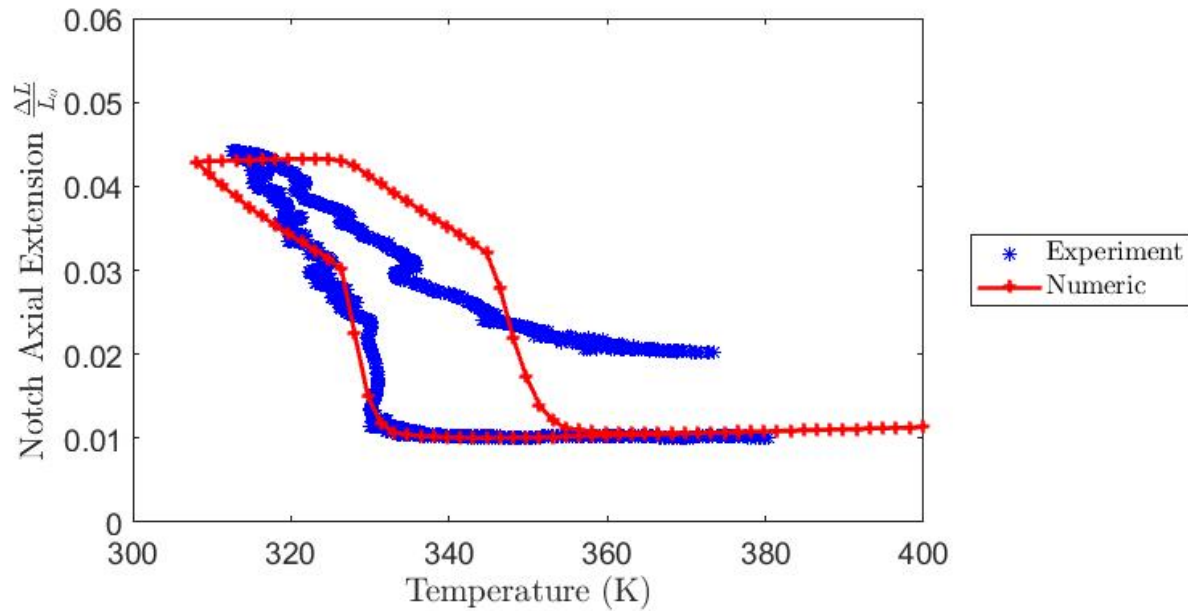
Figure 3.15: Comparison of numeric and experimental axial extension in the notched region under 200 MPa for the $\frac{a}{R} = 0.5$ specimen.

tion and stress redistribution. However, these experiments were only able to provide surface level validation, where as the phase transformation reversal appears to occur within the central regions of the specimen. Therefore experiments performed at TAMU could not completely validate the accuracy of the numerical results. On the other hand, it is possible to determine what happens internally in specimens utilizing some more advanced characterization methods. To that end, a series of experiments were performed at Oak Ridge National Laboratory (ORNL) utilizing neutron diffraction in order to map the evolution of the crystal structure through a beam path. The use of neutron diffraction involved exposing the test specimen to a beam of neutrons directed through the center of the plane of minimum cross section of multiple specimens in order map the crystal structure, both while in austenite and martensite, as well as during phase transformation.
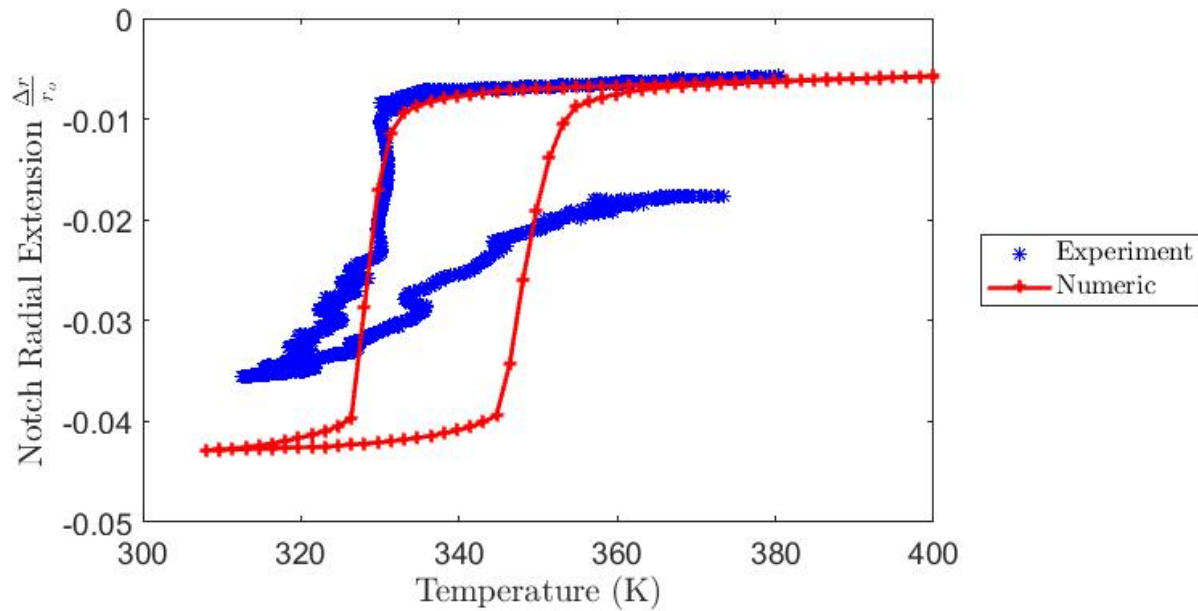
Figure 3.16: Comparison of numeric and experimental radial extension of the plane of minimum cross-section under 200 MPa for the $\frac{a}{R} = 0.5$ specimen.

3.4.1 Neutron Diffraction Experimental Setup

In order to probe the internal crystallographic transformation for notched SMA cylinders, full thermal actuation cycles were conducted at ORNL using beam line 7, also known as VULCAN, at the Spallation Neutron Source (SNS). Utilization of VULCAN allowed for neutron diffraction studies of the notched cylindrical SMA specimens, which in turn could be used to identify the crystal structure of the specimens. The crystallographic information is obtained through analysis of the measured neutron diffraction patterns.

The VULCAN testing facility allows for *in-situ* neutron diffraction studies on the notched cylindrical SMA specimens subjected to tensile loads. This is accomplished by placing the notched cylindrical SMA specimens inside a MTS load frame inside the VULCAN test facility as shown in Fig. 3.21. The MTS frame is also equipped with an inductive heating element in order to allow for heating of the test specimens. In order to cool the specimens, the specimens are exposed to
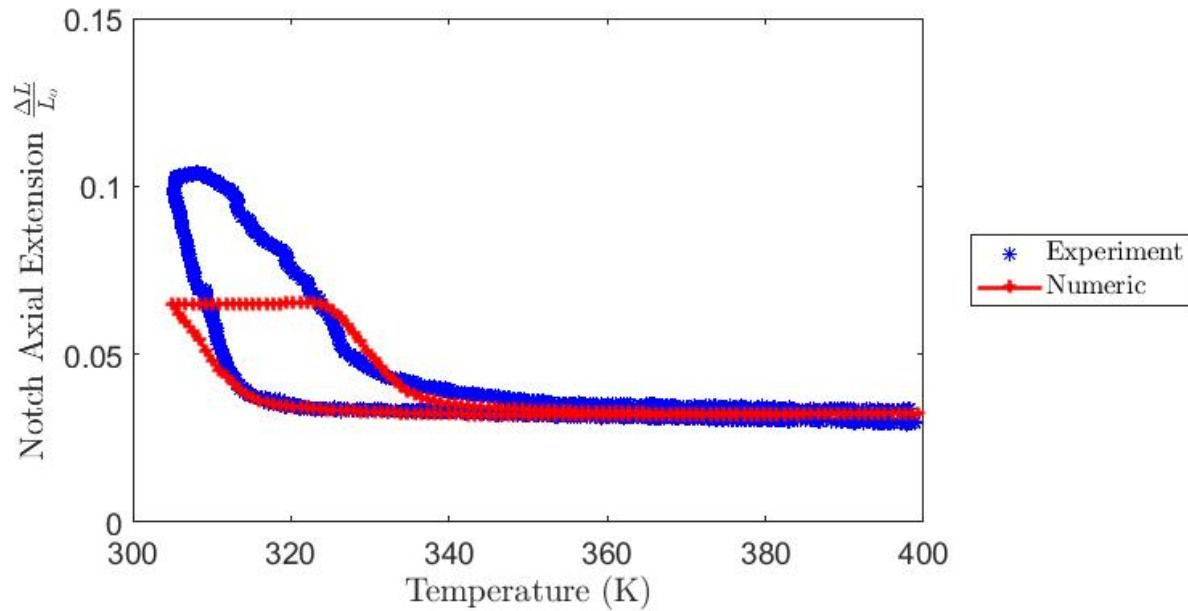
Figure 3.17: Comparison of numeric and experimental axial extension in the notched region under 200 MPa for the $\frac{a}{R} = 2.5$ specimen.

ambient air, therefore experiments can be conducted at or above room temperature, but not below. Also, due to the non-standard size of the notched cylindrical SMA specimens, custom adaptor grips were machined to go from the standard thread pitch used for most specimens at VULCAN to the thread pitch of the notched cylindrical SMA specimens. Larger notched cylindrical SMA specimens were not machined such that any results obtained at VULCAN would be obtained on specimens matching those utilized at TAMU.

Once the test specimens were loaded into the MTS test frame, the neutron beam line is aligned to be incident with the center of the test specimens, as shown on in Figs. 3.22 and 3.23. Due to the small size of the notched cylindrical SMA specimens, the neutron beam was shuttered down to a 2 mm x 2 mm area. After colliding with the specimens, the neutrons are then detected by two detectors banks positioned at $\pm 90°$ diffraction angles. These detector banks measure either the axial or radial diffraction from the notched cylindrical SMA specimens. The detectors are able to detect d-spacing in the specimens ranging from 0.4 Å to 3.0 Å, however the data is generally
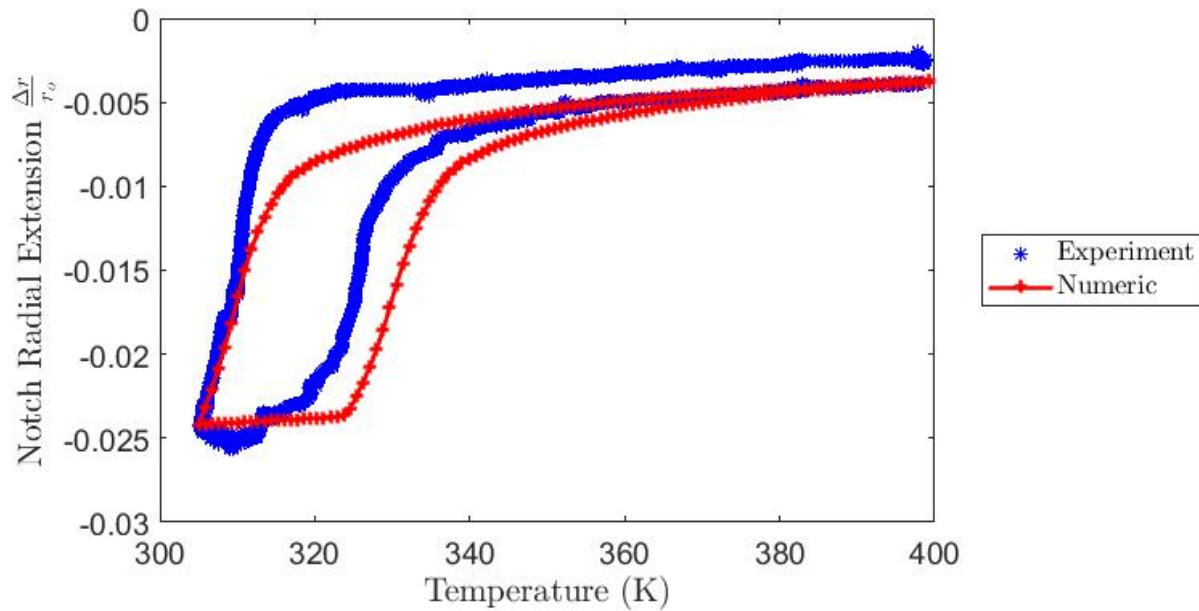
Figure 3.18: Comparison of numeric and experimental radial extension of the plane of minimum cross-section under 200 MPa for the $\frac{a}{R} = 2.5$ specimen.

truncated to d-spaces from 0.5 Å to 2.5 Å due to excessive noise outside these d-spaces. Upon completion of the experiments, the data was processed through the VDRIVE program in order to allow for diffraction data compilation and alaysis. Furthermore VDRIVE allowed for combination of the diffraction data with the matching MTS thermal and mechanical data.[96]. Additional details on the setup of the VULCAN experimental facility can be found elsewhere [97]. Further analysis was conducted by importing the data obtained from VDRIVE into MATLAB in order to allow for comparison of the resulting neutron diffraction spectra from the various specimens and experimental conditions.

Based on the experiments previously conducted at TAMU, it was determined that utilization of $Ni_{50.8}Ti_{49.2}$ notched cylindrical specimens were unable to undergo complete thermal actuation cycles in situations were the minimum temperature was room temperature. Therefore, experiments at ORNL were conducted on notched cylindrical specimens machined out of $Ni_{50.3}Ti_{29.7}Hf_{20}$. The selection of this alloy was based on the requirement that full forward and reverse transformation

64
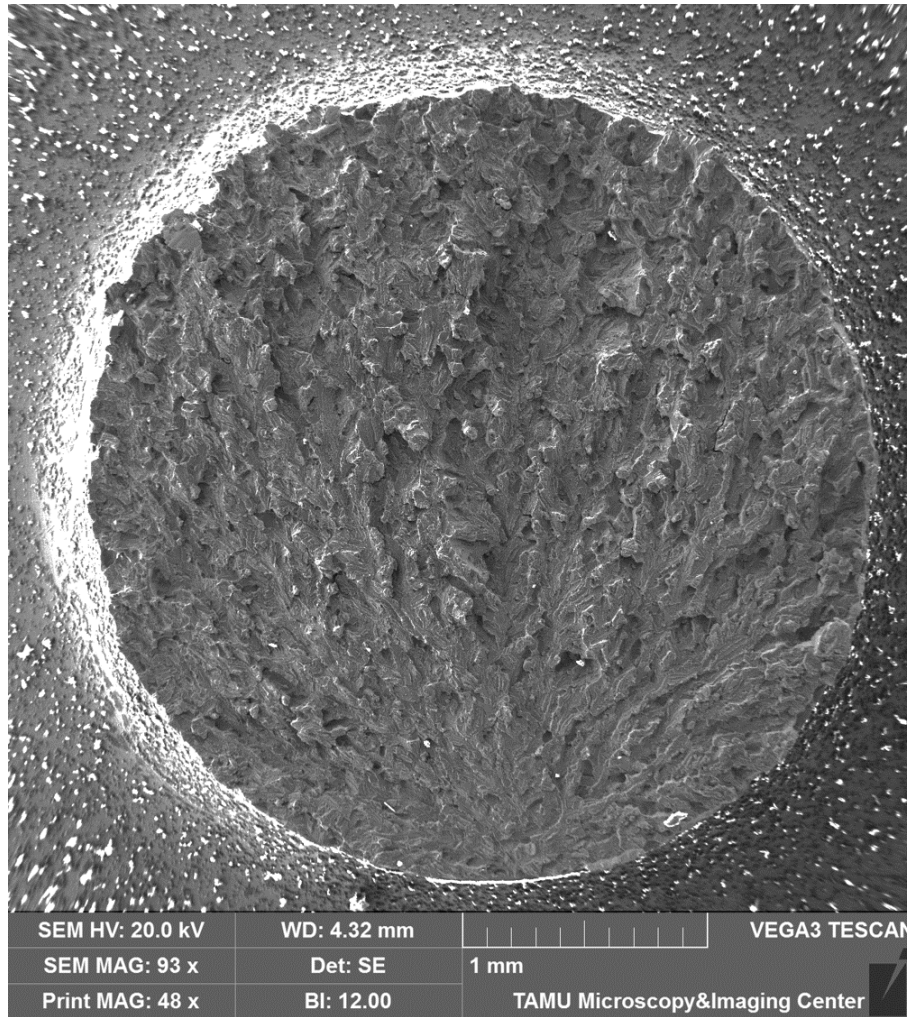
Figure 3.19: Fracture surface for $\frac{a}{R} = 2.5$ specimen subjected to 1150 MPa which failed during phase transformation.

must be achievable well above room temperature. In the case of this particular alloy and the selected heat treatment (500 °C for 3 hours), this lead to a M_F temperature of 160 °C, indicating that full forward and reverse transformation were achievable when exposed to ambient air temperature. Also, based on the numerical results and the beam size limitations, the notched cylindrical specimens utilized at ORNL had notch acuity ratios of $\frac{a}{R} = 0.5$ and $\frac{a}{R} = 1.25$, in addition to the smooth dogbone baseline. For the smaller notch acuity specimens tested at TAMU, $\frac{a}{R} = 2.5$, the neutron beam would not be able to emit enough neutrons in the notch area due to the small size of
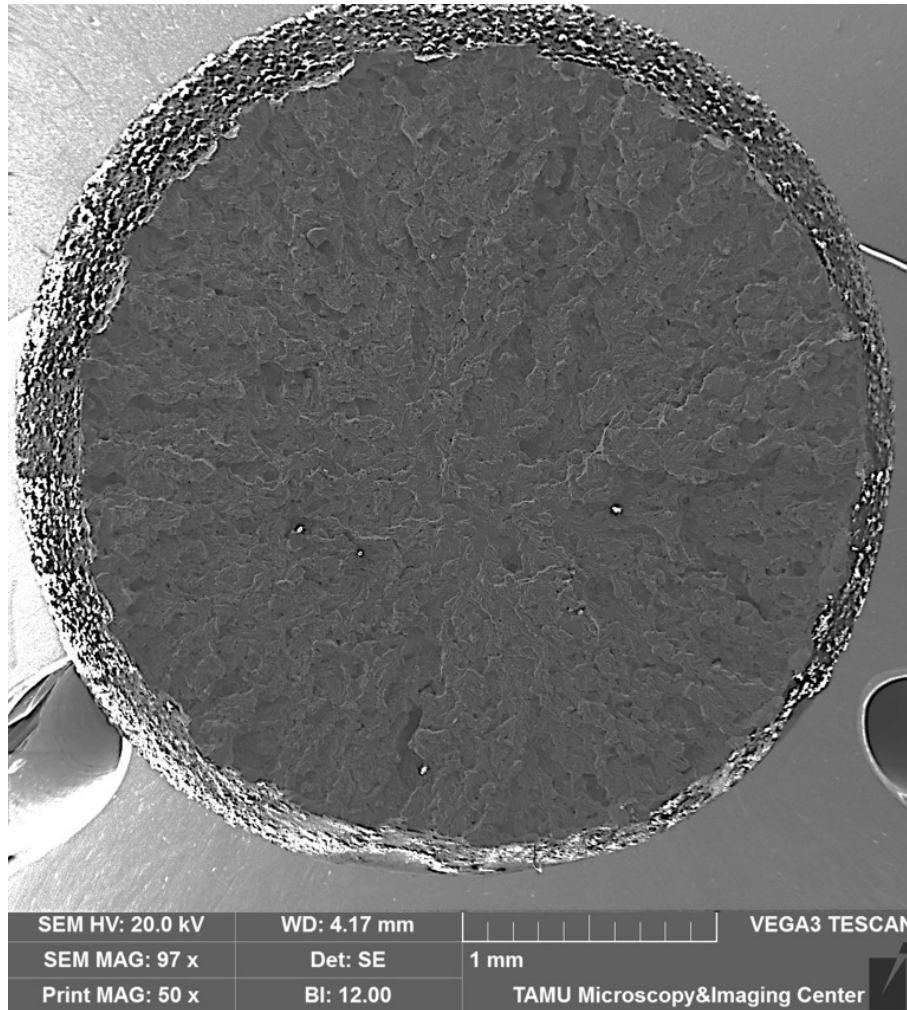
Figure 3.20: Fracture surface for $\frac{a}{R} = 0.5$ specimen subjected to 1150 MPa which failed during phase transformation.

the notch which would be required in order to determine what is happening locally without spilling over into the un-notched regions. Furthermore, as shown in Sec. 2.3, it is expected that the highest level of phase transformation reversal should occur for the $\frac{a}{R} = 1.25$ specimen, while the $\frac{a}{R} = 2.5$ specimen is expected to exhibit little, if any, phase transformation reversal.

After initial placement of the specimens, the experimental procedure was as follows:

1. A pre-load of 100 N was applied to the specimens.

2. A pre-loading neutron diffraction scan was completed to serve as baseline.
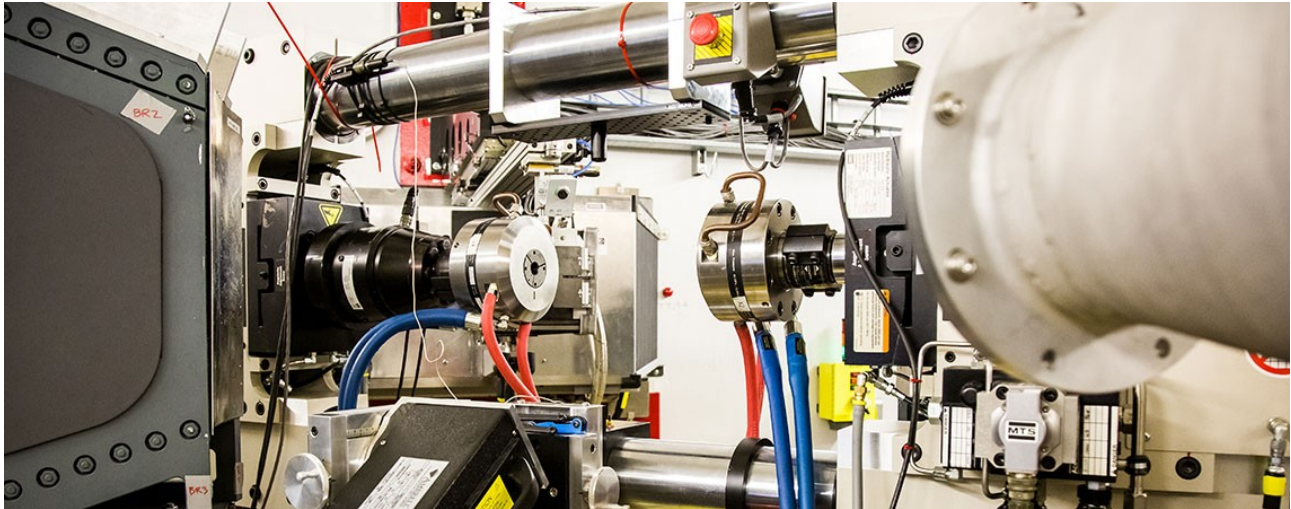
Figure 3.21: Experimental test fixture at VULCAN
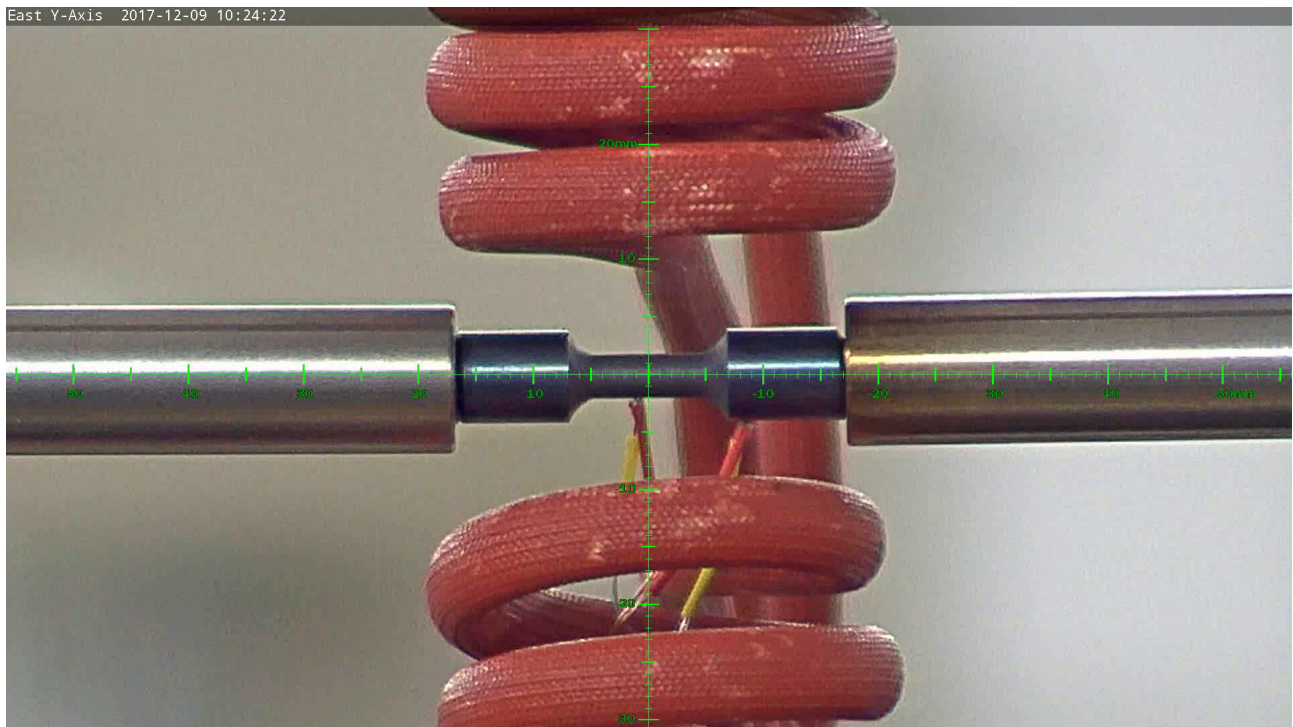
Figure 3.22: Close up of smooth cylindrical dogbone installed into the VULCAN test setup.
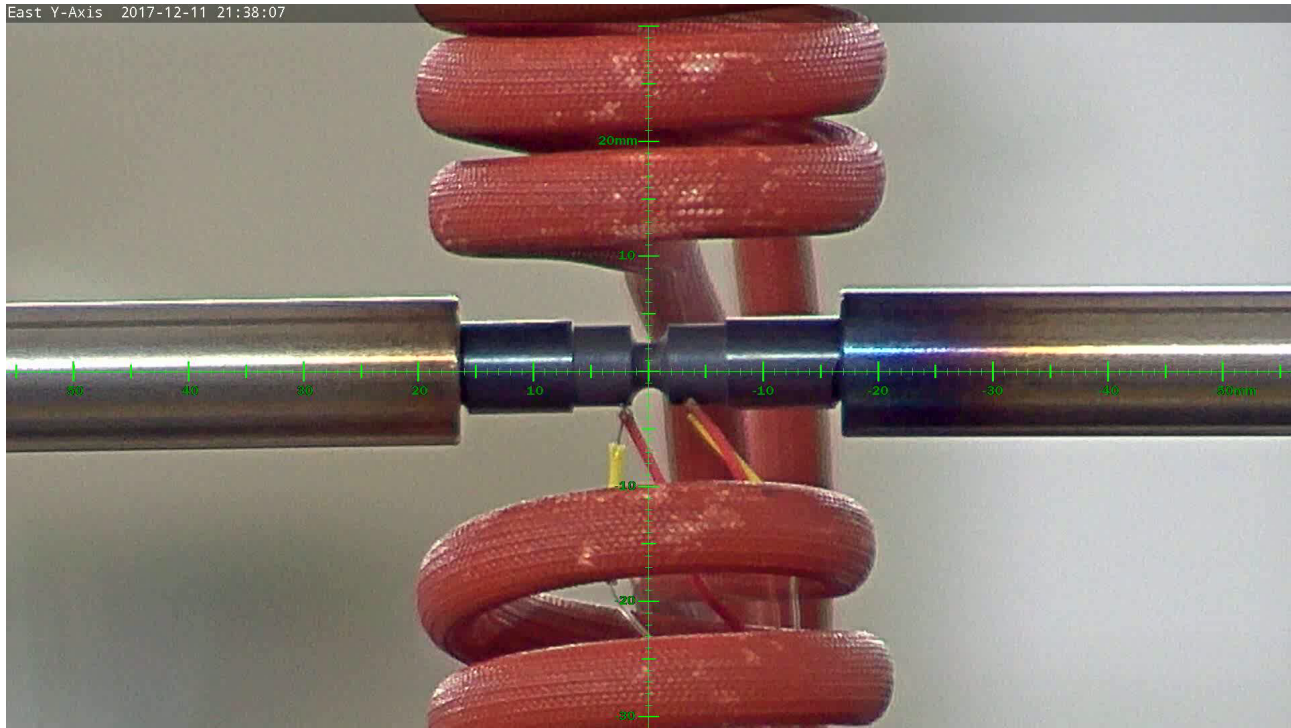
Figure 3.23: Close up of $\frac{a}{R} = 1.25$ specimen installed into the VULCAN test setup.

3. The specimen was heated to 300 °C.

4. A heated neutron diffraction scan was completed.

5. The specimen was loaded to 3597 N, corresponding to the same load level utilized in the numerical simulations and in the experiments at TAMU.

6. A loaded neutron diffraction scan was completed.

7. The specimen was cooled to 100 °C. Neutron diffraction data collected continuously.

   (a) From 300 °C to 225 °C, the cooling rate was 7 °C / min since no phase transformation was expected.

   (b) From 225 °C to 170 °C, the cooling rate was 0.25 °C / min since phase transformation was expected in this range.

(c) From 170 °C to 100 °C, the cooling rate was 7 °C / min since no phase transformation was expected.

8. A cooled neutron diffraction scan was completed.

9. The specimen was heated to 300 °C. Neutron diffraction data collected continuously.

   (a) From 100 °C to 190 °C, the heating rate was 7 °C / min since no phase transformation was expected.

   (b) From 190 °C to 250 °C, the heating rate was 0.25 °C / min since phase transformation was expected in this range.

   (c) From 250 °C to 300 °C, the heating rate was 7 °C / min since no phase transformation was expected.

10. A heated neutron diffraction scan was completed.

11. The specimen was unloaded and cooled.

It should be noted that the above procedure was repeated on two specimens for both the $\frac{a}{R} = 0.5$ and $\frac{a}{R} = 1.25$ specimens in order to ensure that the results were repeatable. Also, the cooling/heating cycle was performed twice on at least one specimen of each notch acuity size in order to confirm cyclic stability.

3.4.2 Neutron Diffraction Results

In order to establish a baseline for the thermal actuation experiments on the notched cylindrical specimens, the baseline austenitic and martensitic neutron diffraction patterns were collected on a smooth cylindrical dogbone specimen. As shown in Figs. 3.24 and 3.25, the austenitic and martensitic d-spacing peaks are clearly different. Comparison of peak intensities from Figs. 3.24 and 3.25 suggests that for axially detwinned martensite, it is sufficient to analyze the diffraction peaks primarily from the axial detector in order to determine the phase of the material. Therefore, the neutron diffraction results from the axial detector are primarily utilized for further analysis.

Furthermore, it can be seen that the sharpest peak for austenite is around a d-spacing of 2.2 Å, where as the most distinctive martensitic peak is around a d-spacing of 2.06 Å. The d-space of 2.2 Å corresponds to the (100) plane in the austenitic B2 crystal structure, while the d-space of 2.06 corresponds to the (100) plane for the martensitic B19' crystal structure. A zoomed in view of these peaks is given in Fig. 3.26.
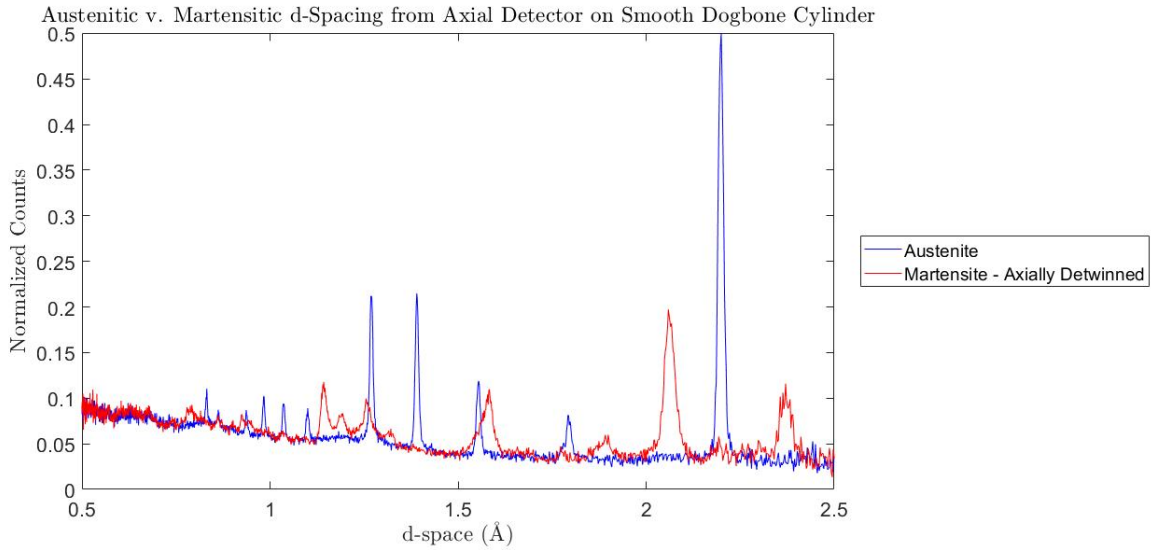
Figure 3.24: Comparison of d-spacing peak intensities for austenite and martensite from the axial detector for the smooth cylindrical dogbone specimen.

From these baseline neutron diffraction patterns on the smooth cylindrical dogbone, it is now possible to determine the effect of the addition of notches into the cylinders. As described in the experimental procedure, neutron diffraction patterns were collected both at high and low temperatures, corresponding to complete austenite and martensite respectively, as well as during the thermal cycling. As expected, while the specimens were held under load at high temperature, the austenitic neutron diffraction pattern for all specimens match as shown in Fig. 3.27. Similarly, under load at low temperature, the martensitic neutron diffraction patterns also match for all spec-
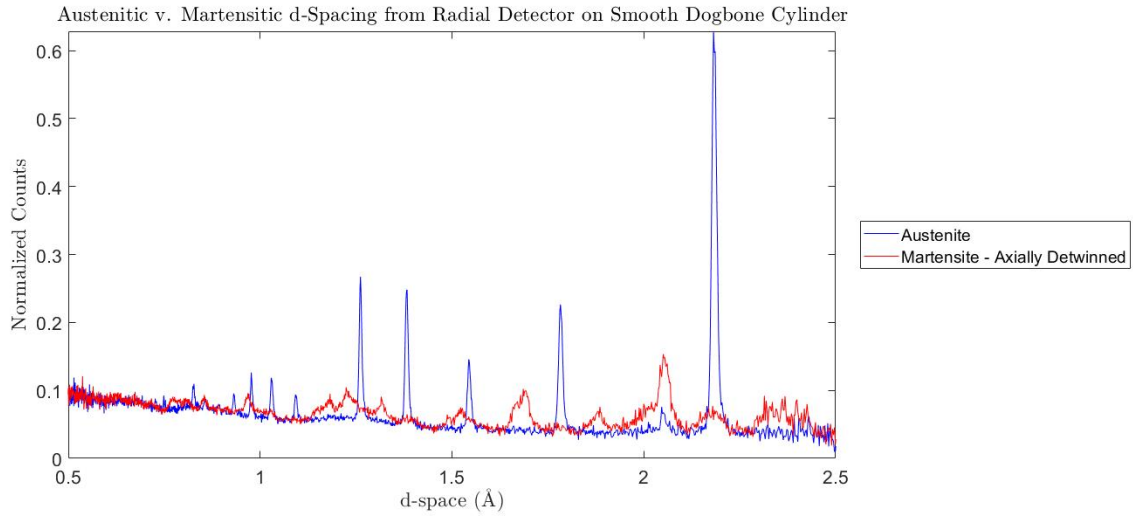
Figure 3.25: Comparison of d-spacing peak intensities for austenite and martensite from the radial detector for the smooth cylindrical dogbone specimen.
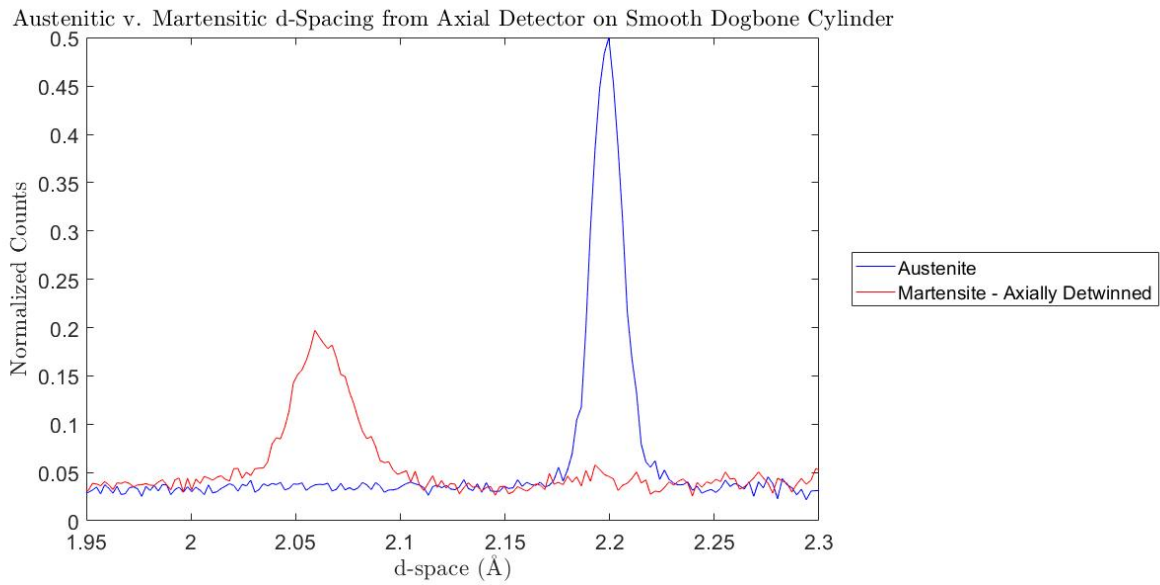
Figure 3.26: Magnification of d-spacing peak intensities for austenite and martensite from the axial detector for the smooth cylindrical dogbone specimen between a d-spacing of 1.95 and 2.3 .

imens as shown in Fig. 3.28. These results are to be expected and are in line with the simulation results described previously.
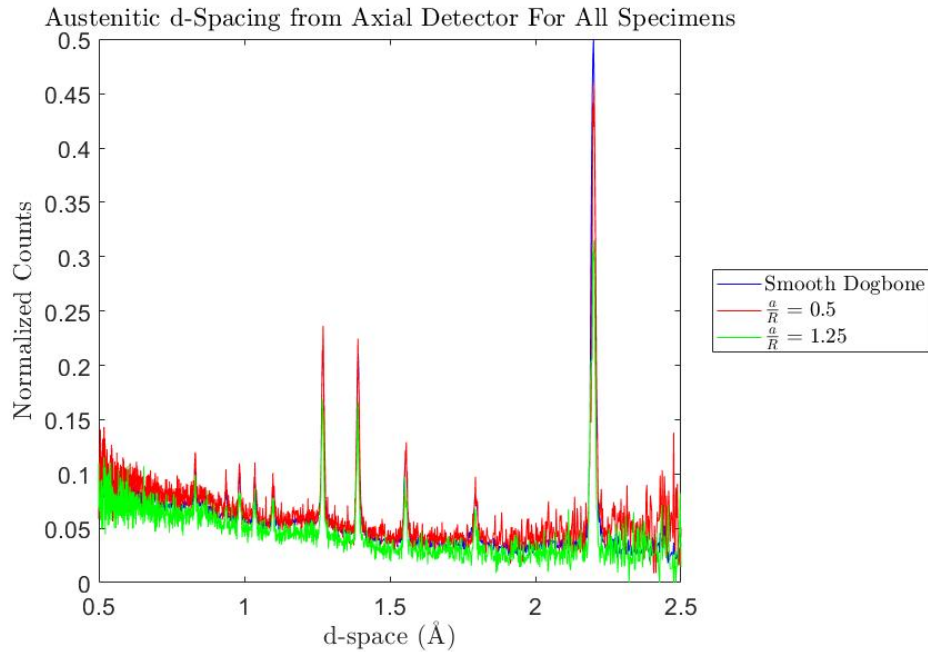
Figure 3.27: Neutron diffraction patterns for all specimens while under load and at 250 °C, indicating an austenitic crystal structure.

The baseline data are useful to ensure that all data is in line with prior results. Specifically, such neutron diffraction results were obtained previously for similar SMA material systems by previous researchers [98–102]. However these prior works have been primarily looking at smooth dogbones cylinders. Therefore, it is useful now to consider the effect of the addition of the notches into the cylinders. The neutron diffraction patterns obtained during the slow cooling and heating portions for the $\frac{a}{R} = 0.5$ specimen is shown in Figs. 3.29a and 3.30a, respectively. Based on the differences in the peaks for austenite and martensite as identified in Fig. 3.26, it is assumed that it is possible to determine the volume fraction of material in austenite based on the relative intensity of the peaks around a d-space of 2.3 Å in comparison to the volume fraction of material in martensite based on
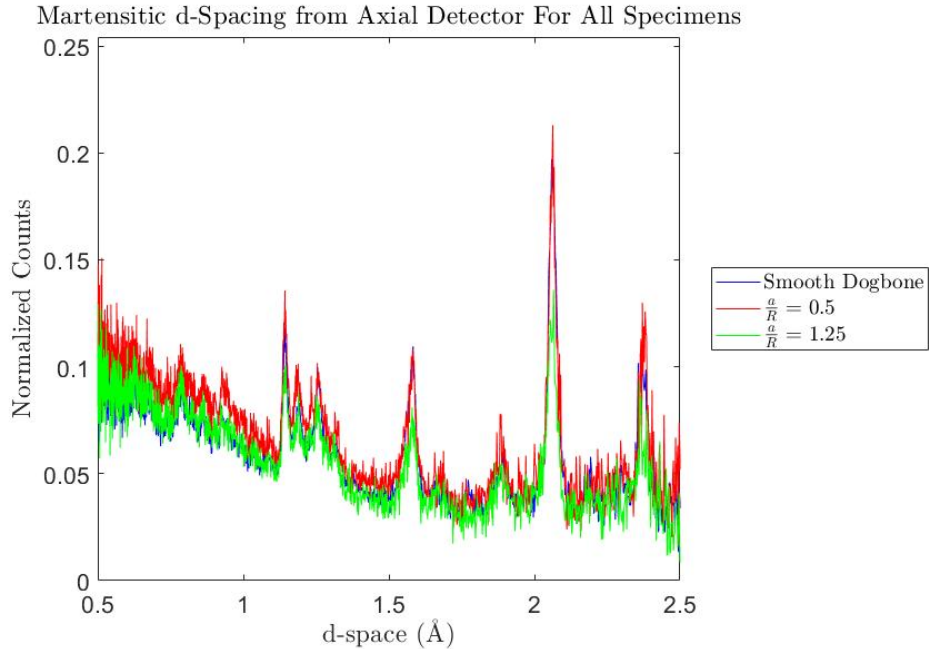
Figure 3.28: Neutron diffraction patterns for all specimens while under load and at 150 °C, indicating a martensitic crystal structure.

the peaks around 2.06 Å. Therefore, in order to utilize the neutron diffraction data to determine volume fraction of material in the austenitic phase, the average of the peaks with d-spacing between 2.26 and 2.35 Å is considered. Similarly, the average of the peaks from d-spacing of 1.98 to 2.1 Å are assumed to represent the martensitic volume fraction. For consistency, and since the magnitude of the martensitic peaks around 2.06 Å are lower than the austenitic peaks around 2.3 Å, the peak intensities are normalized such that maximum intensity of each d-space range corresponds to the material being completely in the corresponding material phase. Additionally, in the processing of this data, flyer points have been eliminated by comparing data points to each other. The reason for this comparison and elimination of data for purposes of austenitic/martensitic volume fraction determination is that the neutron source was not able to provide 100% reliability in production of neutrons. At various times during the ramps, the neutron beam would shut down, causing the test frame to pause the current operation. However in so doing, the data collection was unable to provide smooth and consistent data throughout the entire experimental procedure. As

such, flyers associated with these shutdowns were eliminated. Utilizing these assumptions, it was therefore possible to convert the neutron diffraction results into austenitic and martensitic volume fractions, as shown in Figs. 3.29b and 3.30b for the $\frac{a}{R} = 0.5$ specimen during cooling and heating, respectively.

Based on the neutron diffration data for the $\frac{a}{R} = 0.5$ specimen during both cooling and heating, it is difficult to determine if phase transformation reversal can be identified. In general it can be seen that at high temperatures, the austenitic volume fraction is approximately 1 (as expected), while at low temperature, the martensitic volume fraction is approximately 1. Based on Fig. 3.29b, it is found that the forward phase transformation initiates around 215 °C and complete around 190 °C, well in line with the data gathered from preliminary testing at TAMU on this material for the smooth cylindrical dogbone at the same load level, which is shown in Fig. 1.4. It is interesting to note that the phase transformation even at this scale within the notched region is a distributed phenomena. This matches well with the numerical results from Sec. 2.3, which indicates that the stress is not constant throughout this region of minimum cross-section. Furthermore, Sec. 2.3 indicates that the stress redistribution causes the stress in the center of the specimens to drop which causes completion of phase transformation to take longer. These neutron diffraction results support this conclusion in that, as shown in Fig. 3.29b, the austenitic volume fraction reduces quickly from 215 °C to 200 °C. However in contrast the reduction in austenitic volume fraction from 200 °C to 187°C is much more gradual, indicating that there is material along this plane of minimum cross section which is at significantly lower stress levels than other material in this plane.

As mentioned, one of the reasons why these neutron diffraction experiments were conducted on $Ni_{50.3}Ti_{29.7}Hf_{20}$ was due to the ability of this material to undergo complete thermal actuation cycles at temperatures above room temperature, which was not achievable for $Ni_{50.8}Ti_{49.2}$. Therefore it is useful to also consider the reverse transformation as shown in Fig. 3.30 for the $\frac{a}{R} = 0.5$ specimen. Similar to the cooling of this specimen, no clear reverse transformation is indicated in the neutron diffraction results. However, it should be noted that based on the results of Sec. 2.3, the magnitude of the phase transformation reversal is not expected to be significant and Fig. 2.17 indicates that
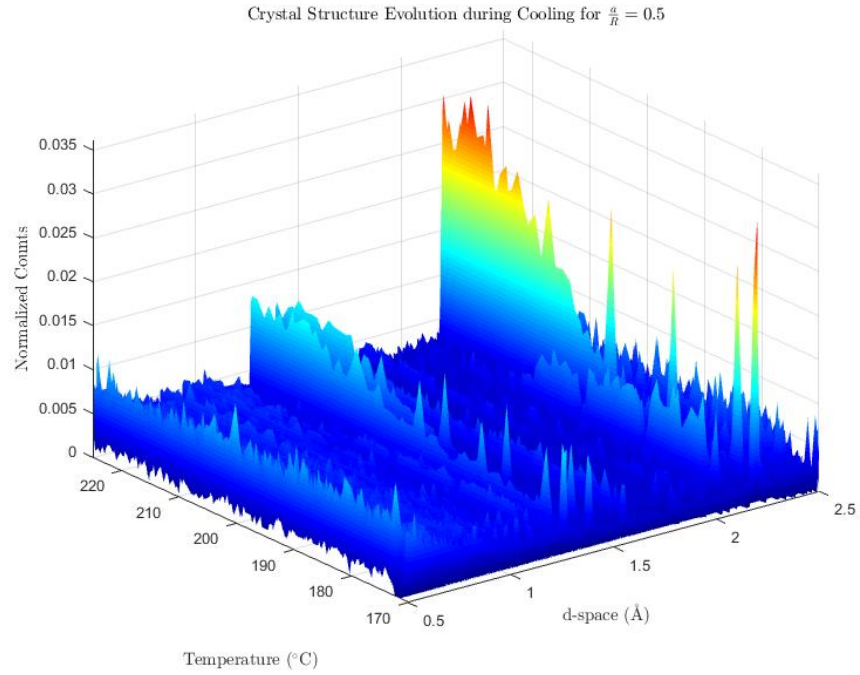
(a) Neutron diffraction patterns
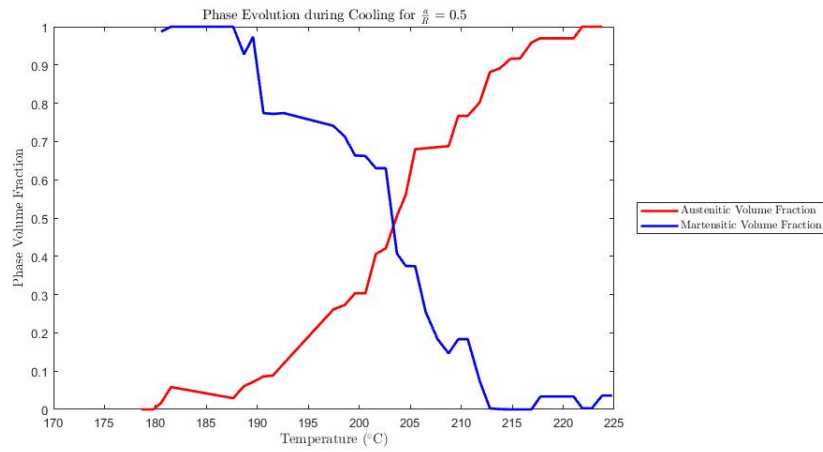
(b) Evolution of austenite and martensite

Figure 3.29: Neutron diffraction patterns and phase volume fraction evolution for $\frac{a}{R} = 0.5$ specimen during cooling.
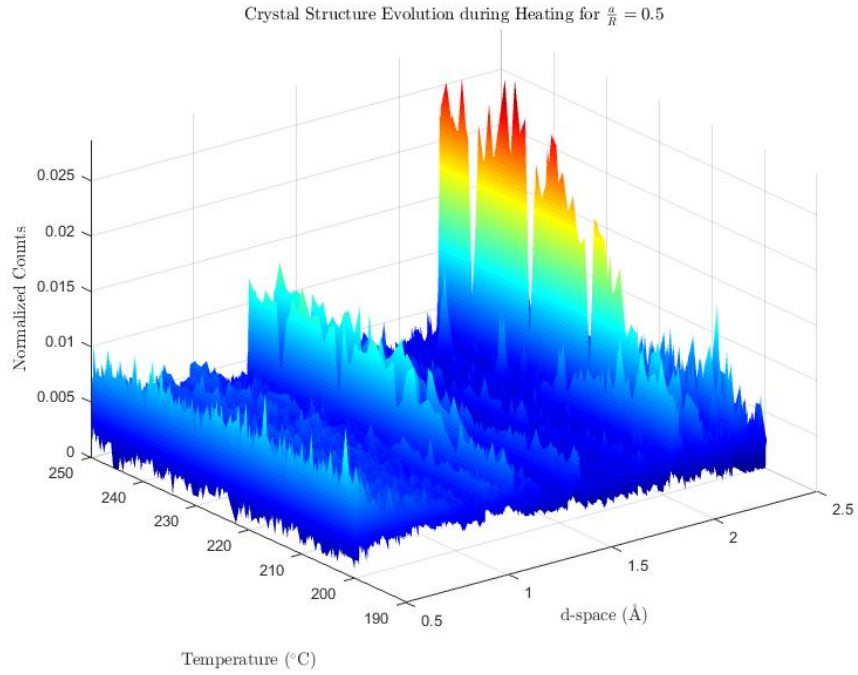
(a) Neutron diffraction patterns
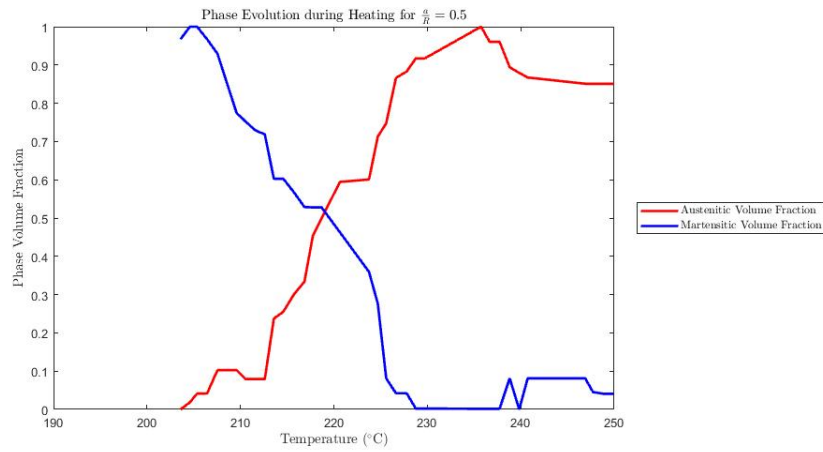
(b) Evolution of austenite and martensite

Figure 3.30: Neutron diffraction patterns and phase volume fraction evolution for $\frac{a}{R} = 0.5$ specimen during heating.

complete phase transformation is expected through the plane of minimum cross section prior to any phase transformation reversal. Therefore, in order to identify any phase transformation reversal, it is useful to consider notch acuities where such phase transformation reversal should be more pronounced, such as for the $\frac{a}{R} = 1.25$ specimen.

The results of cooling and heating for the $\frac{a}{R} = 1.25$ specimen are shown in Figs. 3.31 and 3.32, respectively. As mentioned, the primary reason for performing the neutron diffraction experiments is that it is desired to validated experimentally whether there is any pause and/or phase transformation reversal which can be identified experimentally. Although these results do not clearly identify any phase transformation reversal, it is possible to note some level of pause during both the forward and the reverse phase transformation. As shown in Fig. 3.31b, around 182 °C, it appears that during forward phase transformation (cooling) the martensitic volume fraction pauses. Similarly, the austenitic volume fraction also pauses around this same temperature. Furthermore, during reverse phase transformation (heating), Fig. 3.32b indicates that a similar pause in phase transformation is experienced around 200 °C.

An additional capability that these neutron diffraction experiments were able to capture is a comparison between the global phase transformation behavior throughout the entire notched cylindrical SMA specimen in comparison to the phase transformation happening locally within the plane of minimum cross-section. As mentioned, it was expected that forward transformation should occur throughout the entire specimen between 170 °C and 225 °C, and that reverse transformation should occur between 190 °C and 250 °C. This is clearly shown for a $\frac{a}{R} = 1.25$ specimen in Fig. 3.33 via the typical hysteresis curve for thermal actuation. The novelty of these results is that, based on the martensitic volume fraction measurements as shown in Figs. 3.31b and 3.32b, it is possible to determine the local evolution of the martensitic volume fraction in the plane of minimum cross-section in comparison to the global phase transformation behavior. Based on Fig. 3.33, it is clear that the plane of minimum cross-section is one of the last areas to undergo forward phase transformation into martensite, and is one of the first areas to undergo reverse phase transformation into austenite. Refering back to the phase diagram as shown in Fig. 1.3, this clearly
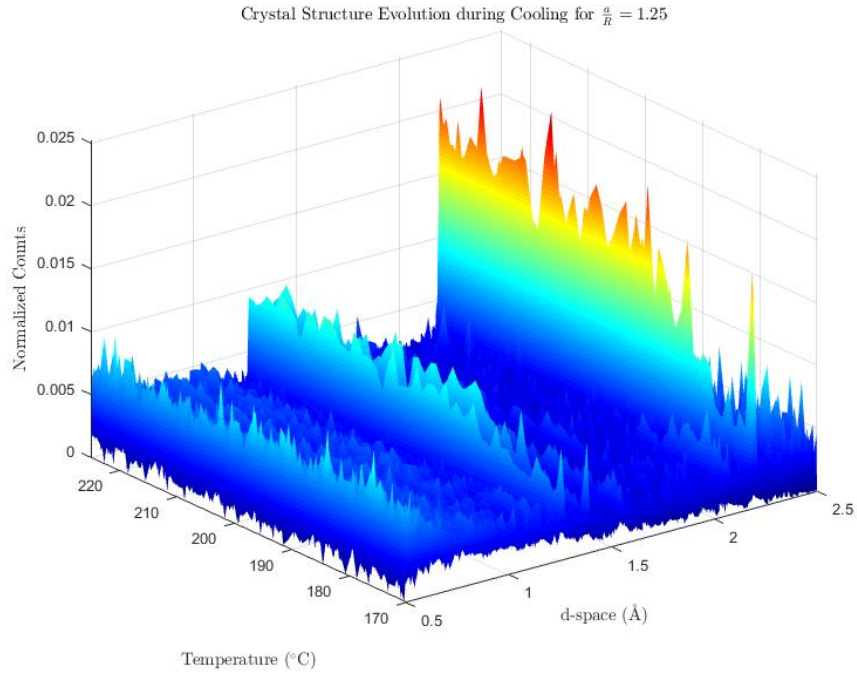
(a) Neutron diffraction patterns
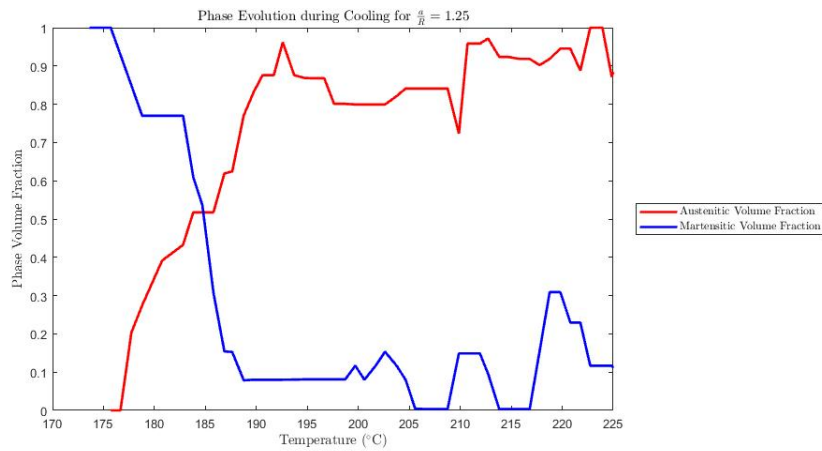
(b) Evolution of austenite and martensite

Figure 3.31: Neutron diffraction patterns and phase volume fraction evolution for $\frac{a}{R} = 1.25$ specimen during cooling.

indicates that the bulk of the plane of minimum cross-section is under relatively low stress. As such, this result suggests that the reduction in stress due to stress redistribution as shown in Ch. 2
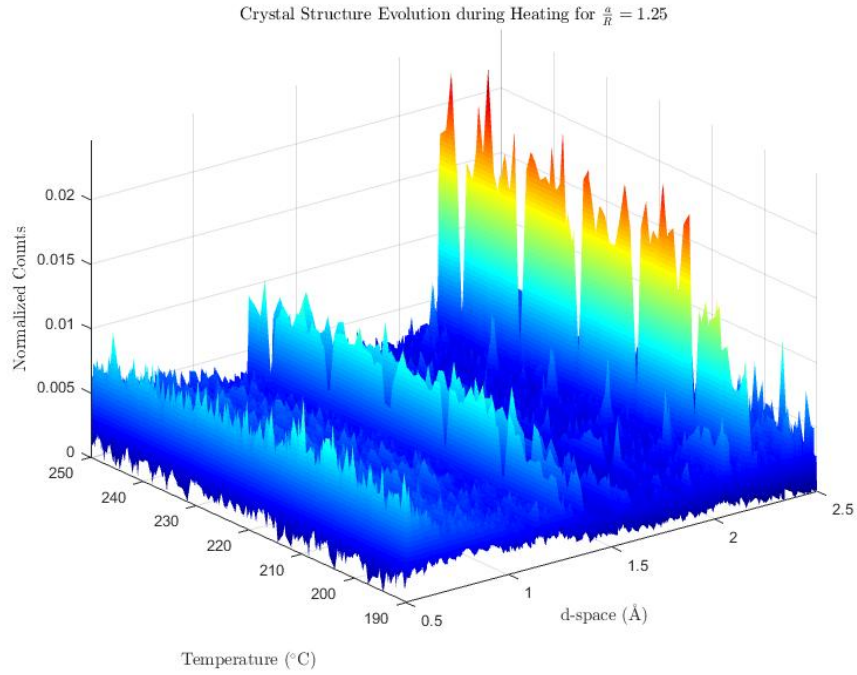
(a) Neutron diffraction patterns
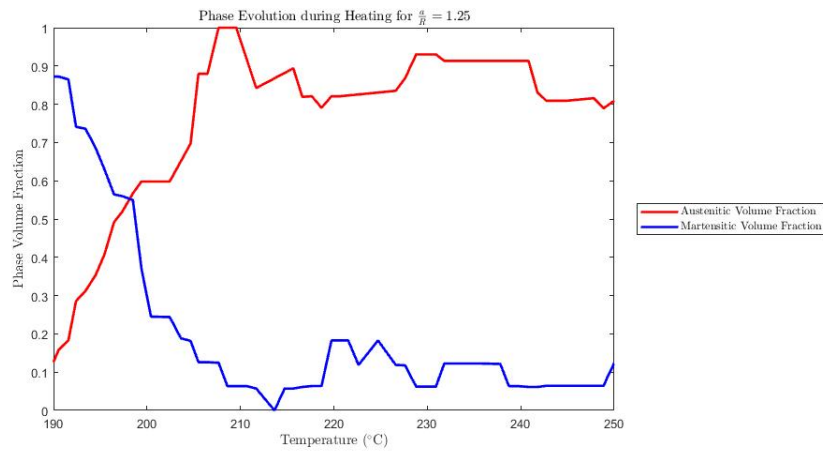
(b) Evolution of austenite and martensite

Figure 3.32: Neutron diffraction patterns and phase volume fraction evolution for $\frac{a}{R} = 1.25$ specimen during heating.

is supported based on experimental evidence. Therefore, these neutron diffraction results seem to support the numerical results presented in Ch. 2 in so far as a pause in the phase transformation

can be identified experimentally.
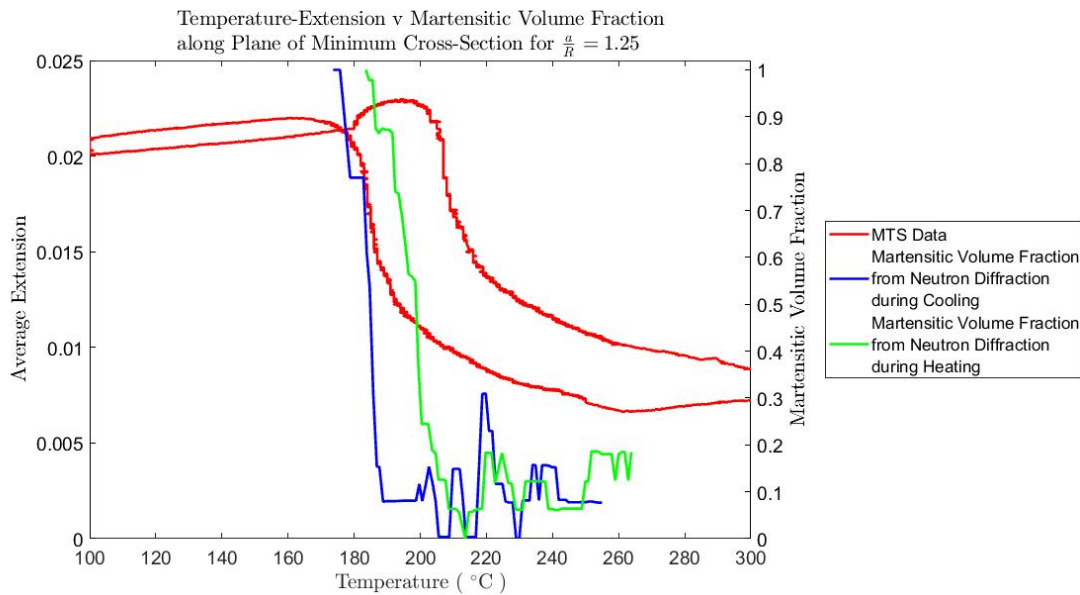
Figure 3.33: Hysteresis loop based on MTS extension and temperature compared with martensitic volume fraction for $\frac{a}{R} = 1.25$ specimen.

3.5 Conclusion

The combined use of experimental and numerical approaches can add extra value to any analysis. Some interesting numerical results were presented in Ch. 2 on the effect of stress redistribution during phase transformation in SMA notched cylindrical bars. In this chapter, various experimental methods were utilized in order to provide some level of experimental verification of the numerical results discussed. Through monitoring of surface strain response under both pseudoelastic and thermal actuation loading paths, it was possible to verify various surface level details of the simulations. Through these experimental results, proof was also given as to the strain/temperature response exhibited, including the non-linearities in the numerical results which suggest changes in the areas undergoing phase transformation. Furthermore, the SEM results presented suggest that for certain critical notch acuities, the stress redistribution and associated phase transformation reversal identified in Ch. 2 could lead to specimen failure initiating from inside the specimen, rather

than at the notch wall where the stresses are the highest.

Finally, a series of experiments were conducted at Oak Ridge National Laboratory which enabled crystallographic identification of the material in the plane of minimum cross-section. In these experiments, all specimens showed the same austenitic and martensitic peaks. A few characteristic d-space peak locations were selected in order to be able to identify the phase of the material. Through a careful analysis of these peaks, it was possible to track the evolution of the austenitic and martensitic volume fractions. Although the results are not as conclusive as the results from Ch. 2, these experiments do indicate that at least some pause in the phase transformation could be identified.

As the entire lifetime of a SMA component is studied, the numerical results presented in Ch. 2 and the experimental results presented in the current chapter are useful in understanding how the phase transformation affects a SMA component for each phase transformation cycle in the presence of stress concentrations. Utilizing this basis of understanding how the stress concentrations affect the stress redistribution due to phase transformation within a single cycle, it is now necessary to look at how these stress concentrations will grow throughout the entire lifetime of a SMA component.

4. CHARACTERIZATION OF DAMAGE EVOLUTION DURING ACTUATION FATIGUE [1]

The preceding chapters have analyzed the impact of stress redistribution in SMAs with stress concentrations during phase transformation in a single thermomechanical cycle. This preceding analysis has utilized notches in cylinders in order to generate the stress concentrations. As the entire lifetime of a SMA component is considered, however, the repeated phase transformation of an SMA component will lead to the formation of internal damage and eventual failure. This formation of internal damage will also lead to the generation of internal stress concentrations. Therefore, in order to understand how the stress will redistribute in a given phase transformation cycle, it is necessary to understand the evolution of internal damage throughout the entire lifetime of a SMA component. In the following chapter, a systematic study is conducted in order to ascertain the evolution of damage throughout the lifetime of a SMA component, specifically for the case of a SMA actuator, in which the SMA is subjected to repeated phase transformation due to thermal actuation.

4.1 Experimental Setup

In order to study the evolution of damage during actuation fatigue in SMAs, two different types of tests were performed. Specifically, the first type of test was performed by actuating various specimens, monitoring the strain response over the actuation fatigue lifetime, and then scanning various specimens which were stopped at a given predicted actuation fatigue lifetime by utilizing X-ray computed microtomography (μCT) in order to reveal the internal damage in the specimen. The second type of tests were performed by conducting partial unloading/loading cycles at fixed cyclic intervals throughout the actuation fatigue lifetime in order to monitor the evolution of the effective modulus for each phase of the specimen. Both types of tests were performed on $Ni_{50.3}Ti_{29.7}Hf_{20}$ dogbone shaped specimens as shown in Fig. 4.1. The gage section of the dogbone actuators was 40.5mm long, 2.7 mm wide, and 0.5mm thick. The phase transformation temperatures of these

---

[1]Portions of this chapter reprinted with permission from "Damage Evolution during Actuation Fatigue in Shape Memory Alloys" by Phillips, F.R., Wheeler, R., and Lagoudas, D.C., 2018, SPIE Smart Structures and Materials and Nondestructive Evaluation and Health Monitoring.
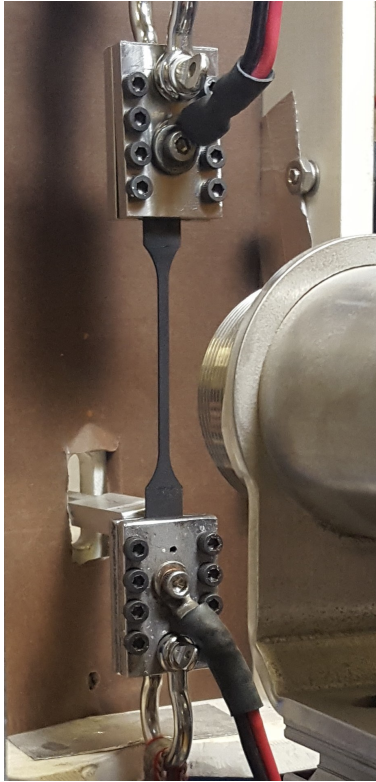
Figure 4.1: Actuation fatigue dogbone loaded within actuation fatigue load frame
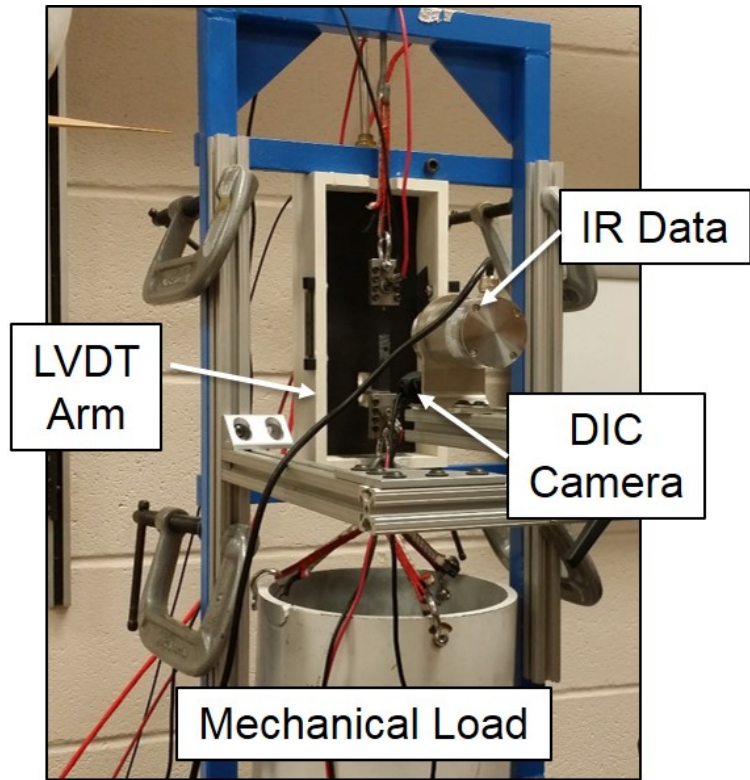
Figure 4.2: Actuation fatigue load frame

specimens are well above 100 °C, thereby allowing for thermal actuation via resistive heating and convective cooling with ambient air. Additional details on the experimental conditions are given below.

4.1.1 Strain Response and Imaging of Internal Damage Evolution

Actuation fatigue experiments have been conducted by loading fatigue dogbone specimens into a custom designed tensile fatigue frame as shown in Fig. 4.2. In this load frame, the top of the specimen is fixed to the top of the fatigue frame and a constant load is attached to the bottom of the specimen, thereby ensuring nominally isobaric loading conditions. An LVDT arm is attached to the bottom grip in order to measure the overall displacement of the specimen. Temperature is monitored via an infrared sensor. A camera is located close to the specimen in order to capture

images for digital image correlation (DIC). Thermal cycling is controlled via a Labview program in order to resistively heat or convectively cool the specimen, as well as to gather data as provided by the various sensors. More details on the experimental setup can be obtained from previous work [90, 92].

In order to determine the evolution of internal damage, actuation fatigue experiments were stopped at various points in the predicted actuation fatigue lifetimes of multiple specimens. The actuation fatigue lifetime predictions are based on the model of Chemisky et al. [94]. Specimens were stopped after 2%, 25%, 50%, 75%, and 90% of their fatigue life. All of these specimens were then imaged using X-ray μCT at the US Naval Research Laboratory using a Zeiss Xradia 520 Versa with a voxel size of 3 μm (a voxel in 3D is the equivalent of a pixel in 2D). For reference, a pre fatigue and a post fracture specimen were also imaged. The resulting images from the X-Ray μCT scans were processed through a custom MATLAB program in order to segment out void areas. The segmentation algorithm is discussed further in Appendix A. After segmentation, the images were recombined into 3D objects utilizing Dragonfly [103].

4.1.2 Effective Modulus Evolution

In traditional metals, the evolution of internal damage due to structural fatigue is frequently characterized as a function of the change of modulus in a specimen. This is typically accomplished by cyclic variation of a mechanical load and monitoring the strain response. However in the present study, it is desired to understand the evolution of damage due to actuation fatigue in shape memory alloys. Furthermore, austenite and martensite typically have a different effective modulus at the beginning of life. Therefore, in order to determine the evolution of the effective modulus during actuation fatigue, thermal actuation cycles were run repeatedly utilizing the same Labview program used for the standard actuation fatigue experiments. However every 20th thermal actuation cycle, upon reaching the maximum cycle temperature, the temperature was held while a mechanical unloading/loading cycle was completed in order to track the evolution of the austenitic effective modulus. Upon completion of this mechanical unloading/loading cycle in austenite, the temperature was lowered to allow phase transformation into martensite, and upon reaching the
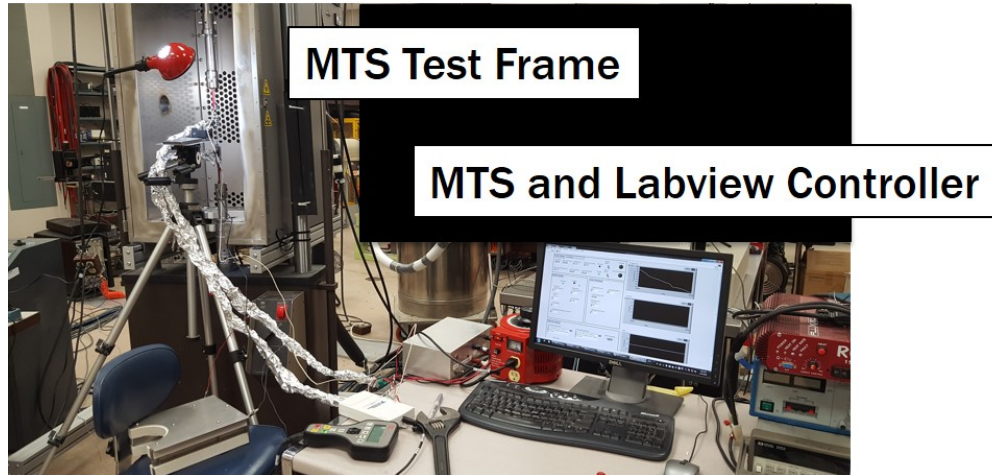
Figure 4.3: Test frame setup for monitoring the evolution of the effective modulus

minimum cycle temperature, the temperature was held constant while another mechanical unloading/loading cycle was completed to track the evolution of the martensitic effective modulus.

Due to the required cyclic mechanical unloading/loading, this test was conducted on a MTS 810 servohydraulic test frame, which allowed for determination and control of the load on the specimen. The test setup is shown in Fig. 4.3. The cyclic control and heating method was the same as described in Sec. 4.1.1. Temperature measurements were obtained from a thermocouple attached to the specimen. In order to determine the extension of the specimen gauge length, marks were placed at the top and bottom of the gauge length as shown in Fig. 4.4. From the location of these marks as captured in images obtained at the end points of the mechanical unloading/loading cycle(as described previously), the extensions were determined, which in turn allowed for determination of the effective modulus when coupled with load data from the MTS test frame.

4.2 Results and Discussion

The accumulation of damage during structural fatigue cycling is a well known phenomena across many material types. However the accumulation of damage due to actuation fatigue is not well understood in SMAs. It is well known that in SMAs there is a certain period of training for the shape memory response. As shown in Fig. 4.5, during this training period at the beginning of life, both the extension in the austenitic phase as well as the martensitic phase increase quickly at first.

Figure 4.4: Actuation fatigue dogbone loaded within test frame for monitoring the evolution of the effective modulus
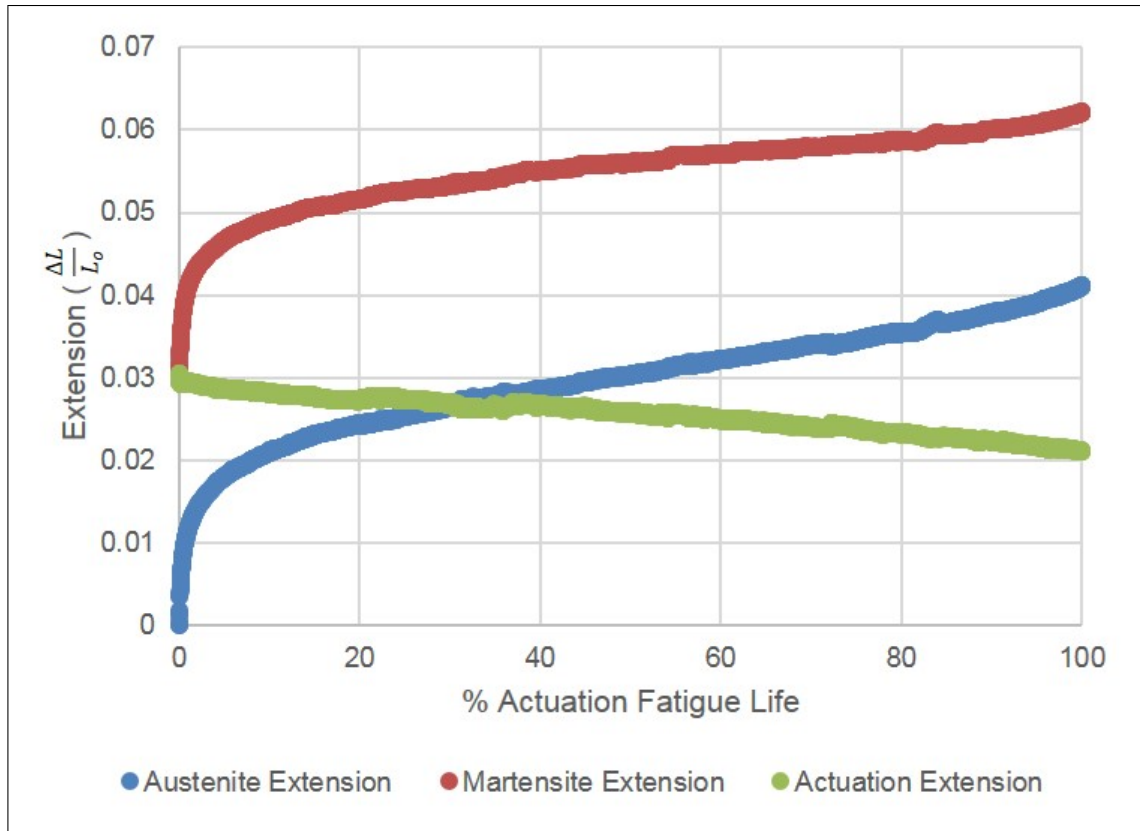
Figure 4.5: Evolution of austenite, martensite, and actuation extension over fatigue lifetime for $Ni_{50.3}Ti_{29.7}Hf_{20}$ subjected to 300 MPa uniaxial loading.

This is due to the formation of irrecoverable strain locally on the surface of the material. Indeed, DIC results from the surface of the component clearly show localization in the development of irrecoverable strain at 2% of the predicted actuation fatigue lifetime as shown in Fig. 4.6. This localization in strain continues throughout the actuation fatigue lifetime of the component and failure generally occurs in these areas of highest localized strain.

In order to understand why the strain is localizing in certain areas of the actuation fatigue specimens, a first step is to look at the surface of the material as a function of the actuation fatigue lifetime. Indeed some prior work has been done in terms of visualizing the surface of specimens subjected to actuation fatigue [84, 104]. These works have found that several surface cracks can be found on the surface of specimens that have failed due to actuation fatigue in comparison to specimens prior to actuation fatigue. However these optical results do not show the evolution of these
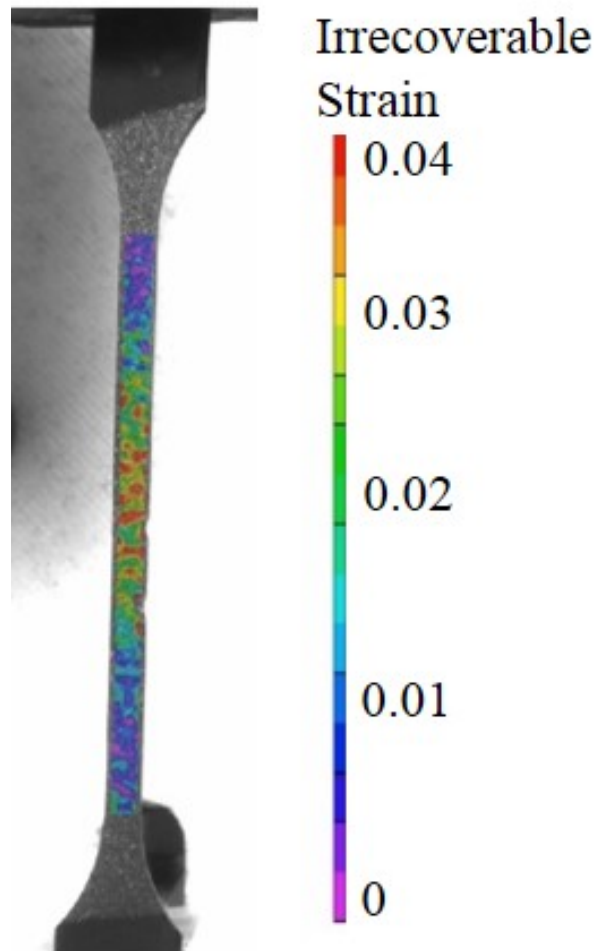
Figure 4.6: Irrecoverable strain in specimen after 2% actuation fatigue as measured via DIC.

surface cracks, nor do they indicate why the surface cracks identified do not lead to catastrophic failure in comparison to the cracks which do lead to ultimate failure. Furthermore, it has also been found that areas with higher amounts of surface cracks correspond to the areas of localized irrecoverable strain as measured via DIC. This makes sense since most materials will have a layer of oxide on the surface, which does not transform. Therefore in order to accommodate the large deformation associated with phase transformation in the center of the material, the oxide layer will tend to form cracks on the surface. Furthermore, analysis of the evolution of irrecoverable strain throughout the actuation fatigue lifetime of a SMA actuator tends to evolve quickly at the beginning of life, with a rapid reduction in irrecoverable strain accumulation after training (as shown in Fig. 4.5). As such, it is expected that surface crack formation will occur most rapidly at the beginning of the actuation fatigue lifetime and experience a rapid decrease in the level of surface crack formation as the actuation fatigue lifetime progresses. This has indeed been confirmed in an optical microscopy study conducted in conducted with this work, in which multiple surface cracks were found on actuation fatigue specimens aged to 25% of their lifetime (as compared to a pre fatigue specimen), but the level of surface cracks did not change significantly at 50% nor 90% of the actuation fatigue lifetime. Therefore, although ultimate failure generally starts from a surface crack, it is necessary to utilize alternative techniques in order to understand what is happening to a SMA actuator during actuation fatigue which will lead to ultimate failure.

In order to further explore this localization of irrecoverable strain as well as formation of surface cracks, the use of non-destructive evaluation methods can be very helpful. As described in Sec. 4.1.1, this has been accomplished utilizing X-Ray μCT to image the evolution of internal damage inside the specimens. The 3D reconstructions of the pre specimen, 2%, 50%, 90%, and post failure specimens are shown in Fig. 4.7. From a qualitative perspective, this figure indicates that the specimen imaged prior to actuation testing has minimal defects, as expected. However, as shown Fig. 4.7b, after only 2% actuation fatigue, immediately a large number of damage sites can be identified. This damage has grown slightly at 50% of the actuation fatigue life as shown in Fig. 4.7c. However at 90% of the actuation fatigue lifetime a significantly higher level of damage can

be observed. The level of damage appears to grow much higher in the post failure specimen.

(a) Prior to Actuation Testing

(b) 2% actuation fatigue

(c) 50% actuation fatigue

(d) 90% actuation fatigue

(e) Post actuation fatigue
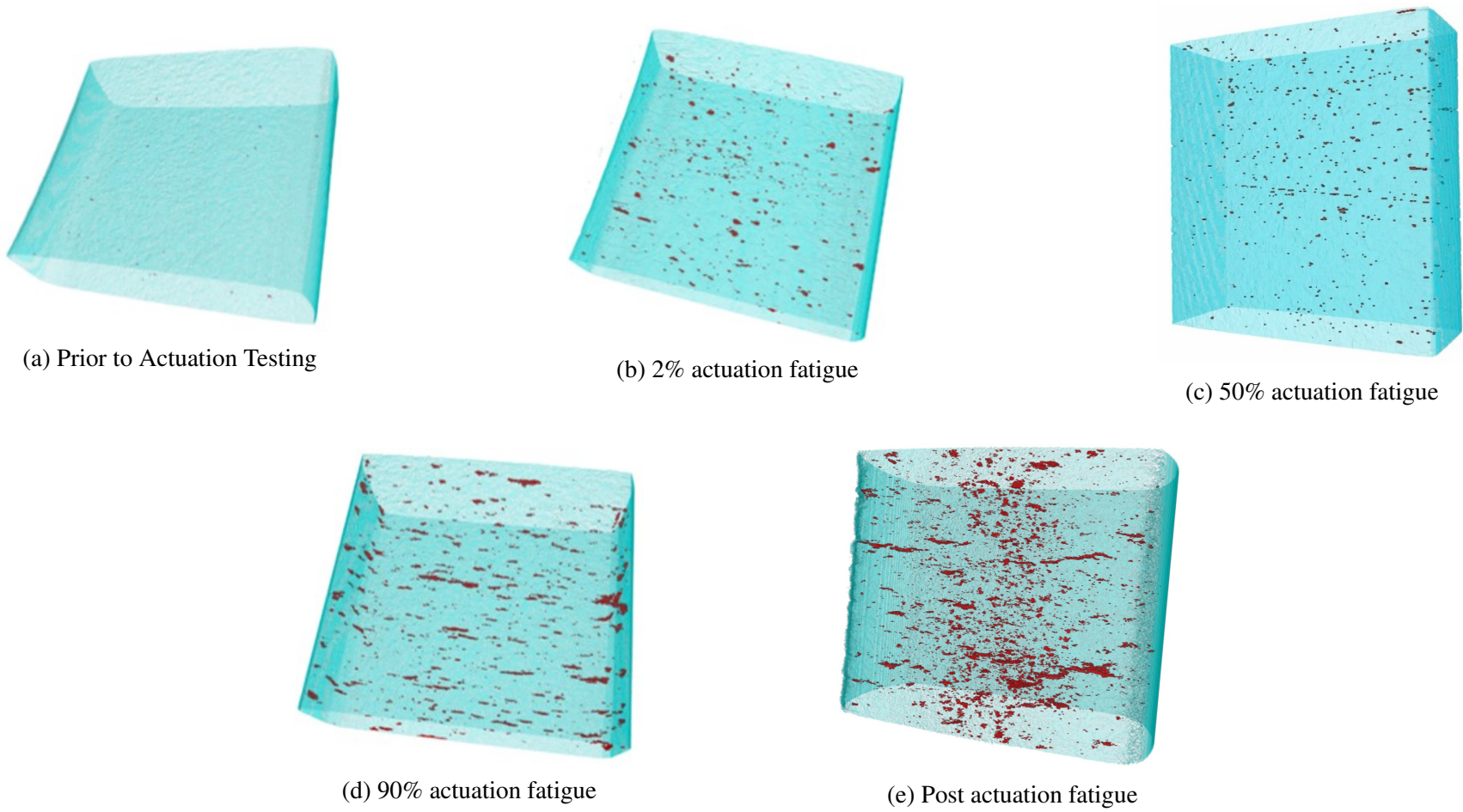
Figure 4.7: Location of internal damage from X-Ray μCT at various actuation fatigue lifetimes

In order to obtain a more quantitative perspective of what these X-ray μCT results are indicating, it was decided to determine a damage volume fraction based on the amount of damage in each specimen with respect to the total volume scanned. As shown in Fig. 4.8, damage clearly accumulates within the specimens in a non-linear manner. At the beginning of life (from 0% to 2%), the data indicates there is a rapid accumulation of damage. It should also be noted that this time period from 0% to 2% of the actuation fatigue lifetime coincides with the training period in the SMA as indicated by the near saturation of irrecoverable extension after 2% of the actuation fatigue lifetime. However, during this training period, it is noted that irrecoverable extension also grows quickly. It is therefore reasonable to conclude that the accumulation of irrecoverable strain is directly related to the accumulation of damage.

In contrast to the rapid accumulation of internal damage during the training period, X-ray μCT data from 2% to 75% shows a much more gradual progression in the accumulation of internal damage as shown in Fig. 4.8. It can also be noted that this gradual accumulation of internal damage is directly proportional to the accumulation of irrecoverable extension. Near end of life however, it can be seen that this accumulation of internal damage increases significantly, as indicated by the data points at 90% actuation life and at the end of life. It can also be noted that, as seen for the 90% specimen shown in Fig. 4.7d, these damage tend to grow in a lateral direction rather than along the axial direction of the specimens. Hence, as expected, the damage tend to coalesce transverse to the direction of the applied load.

While it is useful to know the evolution of damage during actuation fatigue, it is generally impractical to utilize X-ray μCT to determine the status of damage in a structural component while in use. Another more practical method would be to monitor the evolution of the effective modulus of the structural component. Utilizing the methodology described in Sec. 4.1.2, it has been found that there is indeed a significant change in effective modulus due to actuation fatigue. Fig. 4.9 shows the results of this study on the effective modulus. As shown, the effective modulus of austenite is initially higher than that of martensite, which is expected for most SMA material systems [2]. During cycling, it can be seen that the effective modulus of austenite and martensite
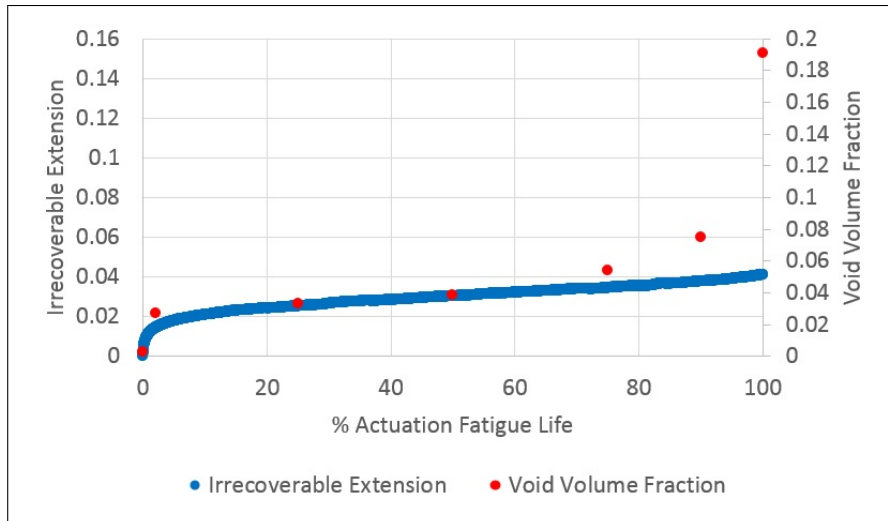
Figure 4.8: Evolution of irrecoverable strain and internal damage during actuation fatigue life.

both drop slowly over time. This slow drop over time is expected since the accumulation of damage volume fraction progresses slowly. Furthermore, since the material is known to be highly brittle due to precipitation hardening, the sudden failure while the effective modulus is still elevated is not surprising.

Comparing the evolution of the effective modulus to the accumulation of irrecoverable strain and evolution of internal damage in the material shows a strong agreement for all of these various characterization parameters through most of the lifetime of these SMA actuators. During the training phase, it was noted that irrecoverable extension accumulates quickly, which in turn should cause the rapid formation of internal damage in order to accommodate this overall extension. However as damage nucleate inside the specimen, there is reduction in material able to sustain the load, which in turn would tend to reduce the effective modulus of the material. After the initial training period, the accumulation of irrecoverable extension is slow and as such damage evolve much more slowly than during the training period. Consequently, the effective modulus can also be expected to evolve much more slowly.

As the actuators approach failure, the X-ray μCT data clearly indicates that the void volume fraction increases dramatically. When the reduction of load bearing material described above is
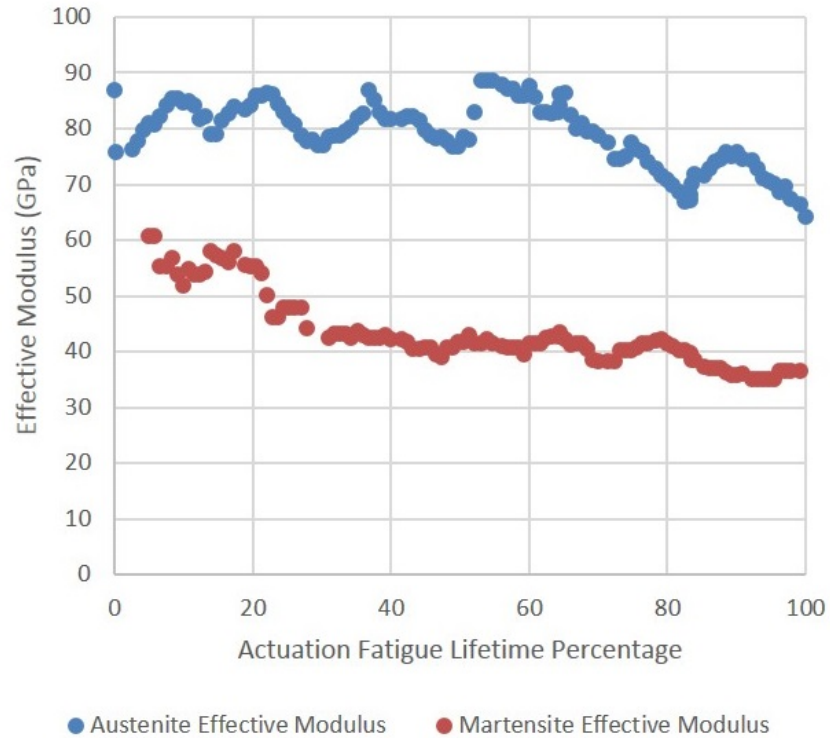
Figure 4.9: Evolution of the effective modulus of austenite and martensite during actuation fatigue lifetime.

coupled with the stress redistribution associated with the phase transformation in SMAs, this would lead to an even faster void formation near the end of the actuation fatigue lifetime. The stress redistribution experienced due to the phase transformation has been shown to lead to a number of unique phenomena in SMAs including a change in the method by which the phase transformation propagates when high stress concentrators are located near one another [105]. Furthermore, it has been shown by Jape et al. [47] that the phase transformation from austenite to martensite tends to promote fracture due to an increase in critical energy release rate. Therefore, when considered in the context of the damage as shown in Fig. 4.7d, it can be clearly seen that these damage sites will lead to many localized high stress concentrations near each other and that as such damage sites will tend to grow and coalesce more quickly during phase transformation. Therefore, the combined effects of less supporting material, stress redistribution during phase transformation, and variation in the critical energy release rate during phase transformation can help to explain why the actuation

fatigue lifetime in SMAs is generally found to be shorter than the structural fatigue lifetime.

4.3 Conclusion

Cyclic thermal actuation in shape memory alloys has been shown to lead to failure due to actuation fatigue. It has been experimentally determined that the accumulation of irrecoverable strain correlates directly with the evolution of internal damage and inversely with the effective modulus of a SMA actuator. Furthermore, this accumulation of internal damage progresses in a nonlinear manner, with rapid damage nucleation at the beginning of life, followed by a slow steady growth until an exponential increase near the end of life. Therefore, as additional applications are being considered for the use of SMA actuators, monitoring of the internal damage in a SMA component is necessary in order to accurately predict the remaining actuation lifetime of the SMA.

5. MODELING OF DAMAGE EVOLUTION DURING ACTUATION FATIGUE

The x-ray computed tomography data presented in Ch. 4 clearly demonstrates that the evolution of internal damage within a SMA specimen is non-linear. The non-linearity in damage evolution can have several implications, including changes to the effective elastic modulus and introduction of additional strain and stress due to inelastic phenomena. Therefore, in order to be able to accurately predict the evolution of SMA components of arbitrary geometry, it is therefore necessary to establish a damage accumulation model which accounts for this non-linearity in damage accumulation. In addition, it is also desired to use such a model in order to determine the actuation fatigue lifetime of the components. Additionally, as was demonstrated in Ch. 2 and Ch. 3, the phase transformation within each phase transformation cycle is directly linked to the existence of stress concentrations. By modeling the evolution of these stress concentrations throughout the actuation fatigue lifetime of a SMA actuator and combining this model with the variation in phase transformation due to stress concentrations, it is therefore further possible to obtain a better understanding of how phase transformations will progress within each thermal actuation cycle throughout the entire actuation fatigue lifetime of a SMA actuator.

5.1 Modeling of Damage Evolution

As mentioned in the Ch. 1, there are a number of models that currently exist for failure due to structural fatigue. Many of these models exhibit a non-linear damage accumulation, starting with a long slow damage growth from the beginning of life and then the internal damage increases exponentially near the end of life. However, for SMA actuation fatigue, there are very few models available that predict the evolution of damage during actuation fatigue. The 3D constitutive model of Chemisky et al. [94] proposes to evolve damage in a linear manner as a function of cycles to failure, similar to the model proposed by Miner [106]. Specifically, the linear damage evolution proposed by Chemisky et al. is of the form shown in Eq. 5.1.
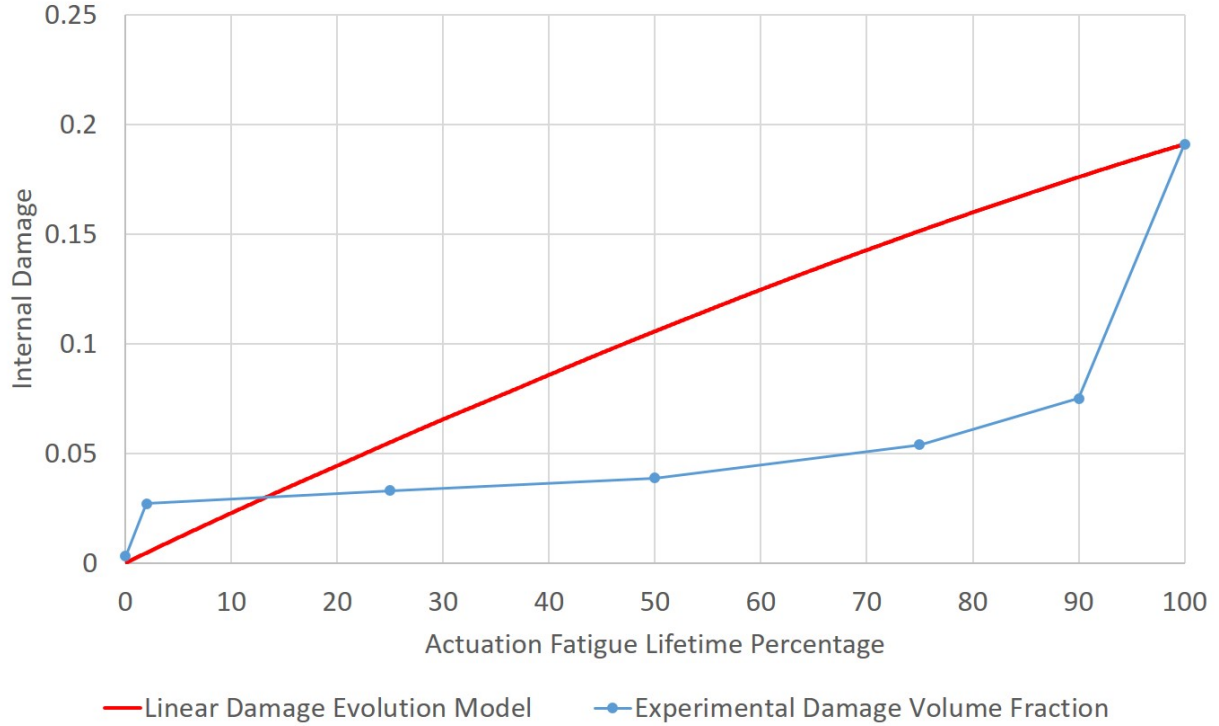
Figure 5.1: Comparison of Internal Damage Evolution as determined experimentally versus a linear damage evolution model.

$$\frac{\dot{d}}{d_{crit}} = \frac{\dot{N}}{N_f} \tag{5.1}$$

Unfortunately neither the structural fatigue models nor the linear damage accumulation model match the experimental results obtained in the previous section. Figure 5.1 shows a comparison between the linear damage evolution model (as posited by Chemisky et al. [94] and the experimental data. The figure clearly shows that the linear damage accumulation model overestimates the internal damage through much of the lifetime of the SMA actuator. Therefore, a new formulation is needed in order to accurately capture the evolution of internal damage in a SMA actuator.

5.1.1 Damage Evolution Formulation

In order to capture the non-linear behavior exhibited by the internal damage as determined experimentally, a compound function is proposed. The initial portion of the lifetime (from 0 to

50% of the life) resembles a logarithmic function, where as the end of the lifetime resembles an exponential function. As such, defining $\tilde{N}$ as the percentage of the actuation fatigue lifetime, a function for the internal damage d in the form of Eq. 5.2 is proposed.

$$d = c_1 log(c_2 \tilde{N}) + c_3 e^{c_4 \tilde{N}} \tag{5.2}$$

Utilizing the convention that $\dot{\tilde{N}}$ indicates a differentiation of $\tilde{N}$ with respect to time, the differential form of the damage equation with respect to time is

$$\dot{d} = \frac{c_1}{\tilde{N}}\dot{\tilde{N}} + c_3 c_4 \dot{\tilde{N}} e^{c_4 \tilde{N}} \tag{5.3}$$

As shown in Eq. 5.3, it is proposed that the incremental increase in damage is composed of two unique parts. For simplicity, the first portion of Eq. 5.3, $\frac{c_1}{\tilde{N}}\dot{\tilde{N}}$, can be considered as a damage nucleation term, while the second portion, $c_3 c_4 \dot{\tilde{N}} e^{c_4 \tilde{N}}$, represents damage growth and coalescence. To explain these components more clearly, it is necessary to consider how damage would form and propagate within the SMA. Consider first the damage nucleation term. It is will known that metallic materials will have various types of dislocations within their matrix. According to Callister [107], "A dislocation is a linear or one-dimensional defect around which some of the atoms are misaligned." Furthermore, dislocation slip is directly associated with the motion of these dislocations due to motion of the atomic planes. In addition, the dislocation motion can typically be constrained ("pinned") by a number of factors including grain boundaries, precipitates, strain hardening, etc.

Applying these concepts to SMAs, it can therefore be assumed that after solidification, SMAs will have a number of dislocations randomly distributed throughout the matrix, as shown schematically in Fig. 5.2.a. In this figure, it is schematically shown that dislocations are randomly scattered throughout various grains, where the grain boundaries are defined by the black lines. Recalling that the phase transformation in SMAs is directly associated with the propagation of a transformation front (habit plane) which will change the crystal structure of the atoms, it can therefore be

reasonably assumed that this transformation front will carry dislocations, as shown schematically in Fig. 5.2.b. For illustrative purposes, the phase transformation propagation front is indicated by the red lines and moving in the direction of the arrows. Due to the fact that the phase transformation progresses through each grain individually, it is therefore reasonable to conclude that after phase transformation has completed in each grain, the dislocations which have been carried due to the phase transformation front will therefore become pinned at the grain boundaries, as shown schematically in Fig. 5.2.c. Considering the fact that crack initiation takes place due to the accumulation of dislocations [1], and as illustrated schematically, that the dislocations are moving due to phase transformation, it is therefore proposed that crack nucleation is directly associated with the motion of dislocations to areas where they become pinned (such as at grain boundaries) and thus accumulate, leading to crack formation. Furthermore, since atomic motion will occur during every phase transformation, it is likely that the dislocation motion will occur during every phase transformation cycle. However, barring the introduction of new dislocations, there will be a constant decrease in dislocations available for motion as the number of phase transformation cycles increase. This is in direct agreement with the results of Dunand-Chatellet and Moumni [108], in which they found that there is a high level of acoustic events which occur within the first cycle, and much fewer acoustic events in subsequent phase transformation cycles, at least up until close to failure. Therefore, there will be the highest amount of dislocations moving to the pinning locations during the first transformation cycle and a constant reduction in this dislocation motion as the number of cycles increases, thereby meaning that crack nucleation will be highest in the initial transformation cycle and the rate of nucleation will decrease as number of cycles increases. Indeed according to Gall and Maier [42], there is an absence of dislocation activity after initial cycling.

With respect to the second term in Eq. 5.3, this term is physically representative of damage growth and coalesence. As the number of cycles increases, there is progressively less sites available to nucleate damage. However the existing damage locations will progressively grow in size. At first this damage growth is slow, however as these damage locations grow, eventually they will become so large that they will tend to coalesce. Such a mechanism for damage growth and coalescence has
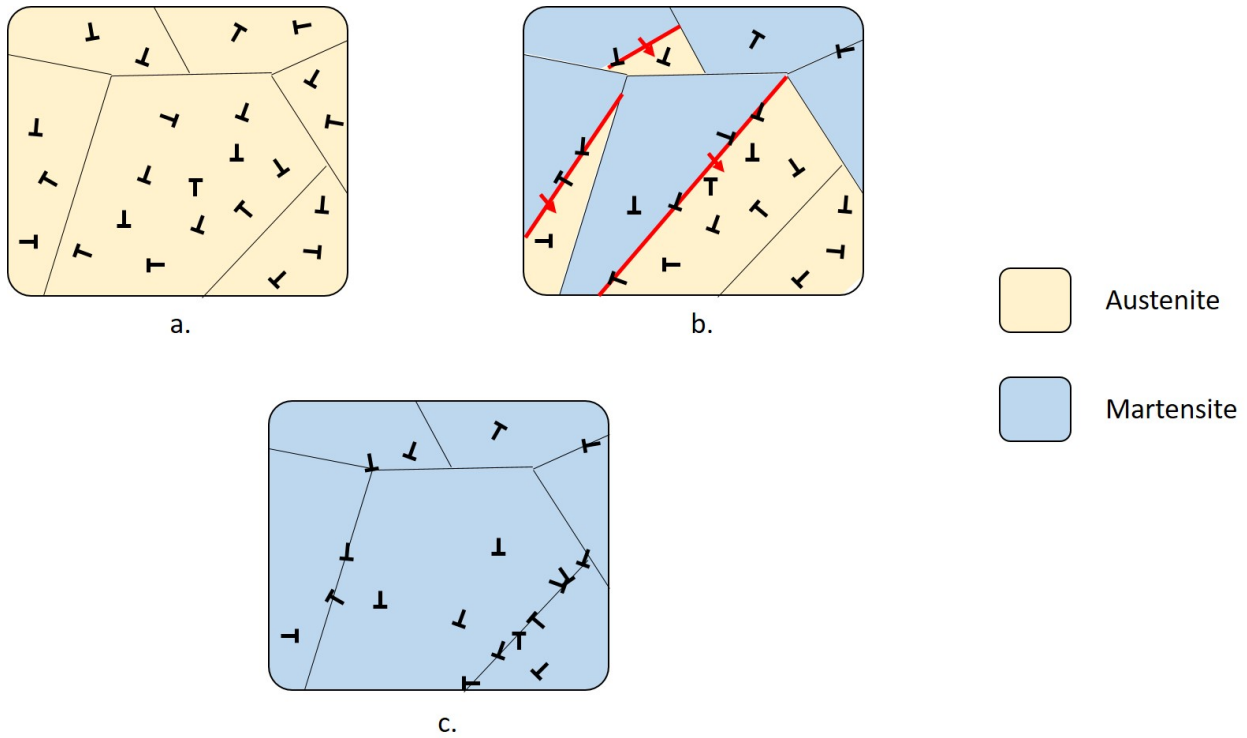
Figure 5.2: Motion of dislocations during phase transformation.

been seen across a number of materials [109] and indeed the modeling of fatigue in many materials follows such an exponential form [110–112]. Therefore, the second term of Eq. 5.3 is proposed in an exponential fashion in keeping with prior works.

In order to utilize the percentage of actuation fatigue lifetime, $\tilde{N}$ in the incremental damage accumulation model, it is necessary to postulate a functional form for the incremental percentage of actuation fatigue lifetime. From a modeling perspective, keeping track of a cycle number is not thermodynamically consistent, but rather the model should be related to some internal state variable which can be tracked. Furthermore, in order to keep in line with the model of Lagoudas et al. [95], it is necessary to relate the incremental percentage of actuation fatigue lifetime with the martensitic volume fraction in order to allow for derivation of the thermodynamic driving forces. One additional consideration which is utilized in the determination of a function for the incremental increase in the percentage of actuation fatigue lifetime is that it is assumed that damage only grows during forward transformation. This assumption is based on the work of Jape et al. [47], in which

100

they showed that the crack tip energy release rate increases during forward transformation until forward transformation is completed. In contrast, during reverse transformation, this crack tip energy release rate decreases. These numerical results indicate that cracks will tend to grow during forward transformation but not during reverse transformation. Experimental results on compact tension specimens have shown similar results, in that cracks have been shown to grow during cooling and close or remain constant during heating [113]. Therefore, damage is assumed to grow only during forward transformation. Furthermore, Jape et al. showed that the crack tip energy release rate increases in a nearly linear manner during forward transformation [47]. It is thus proposed that the incremental percentage of actuation fatigue lifetime (and thereby the internal damage evolution) implementation will increase only during forward transformation in a linear manner such that complete forward transformation (increasing the martensitic volume fraction from 0 to 1) leads to the equivalent damage increase from a complete thermal cycle. In this way, it is possible to account for varying load levels as a function of martensitic volume fraction, as well as for partial cycles. Taking all of these factors into consideration, it is proposed for the incremental percentage of actuation fatigue lifetime follows Eq. 5.4.

$$\dot{\tilde{N}} = \begin{cases} \frac{1.905\dot{\xi}(\xi-\xi_{min})}{N_f}, \dot{\xi} > 0 \\ 0, \dot{\xi} \leq 0 \end{cases} \tag{5.4}$$

In Eq. 5.4, the term N_f represents is number of cycles to failure. There have been several prior studies that have attempted to predict the actuation fatigue lifetime of SMAs using a number of different criterion. Some of the earliest work on actuation fatigue have shown a correlation between the applied actuation stress and the cycles to failure [68, 74]. Others have found that the level of TRIP may be a better predictor for actuation fatigue lifetime [79, 81, 91]. Another method for actuation fatigue lifetime prediction which has been utilized more recently is based on the actuation work [61, 67, 84]. All of these criterion have been able to predict the actuation fatigue lifetime for certain material compositions and heat treatments, however of all these methods, the actuation work method appears to be applicable across the widest range of materials after appropriate model

parameter calibration. Following the work of Calhoun et al. [67], the cycles to failure, N_f, is determined as a function of the actuation work, $\hat{\Phi}$, defined as $\hat{\Phi} = \sigma \epsilon^t$, and the calibration parameters, C^d and γ_d, such that

$$N_f = (\frac{\hat{\Phi}}{C^d})^{\gamma_d} \qquad (5.5)$$

It should be noted that this implementation is based on the uniaxial tensile loading. Therefore, in order to generalize the actuation fatigue lifetime prediction for 3 dimensional cases, the form of $\hat{\Phi}$ can be generalized such that it involves the double dot product of stress, σ and the maximum transformation strain $\mathbf{\Lambda}^t$ (in conjunction with the work of Chemisky et al. [94]), as shown in Eq. 5.6.

$$N_f = (\frac{\sigma : \mathbf{\Lambda}^t}{C^d})^{\gamma_d} \qquad (5.6)$$

It should be noted that in the definition of $\tilde{N}$, there is a term ξ_{min} which appears in the multiplication with the martensitic volume fraction, ξ. The term ξ_{min} is defined as the minimum martensitic volume fraction at a point during reverse phase transformation prior to the start of forward phase transformation. This term is used to acknowledge the fact that, as discussed, the crack tip energy release rate increases during forward transformation based on the work of Jape et al. [47]. However, in cases of partial cycling, the increase in crack tip energy release does not go from the crack tip energy release rate in full austenite to the crack tip energy release rate in full martensite, but rather the crack tip energy release rate oscillates between some intermediate values. Therefore, in order to accommodate partial cycling, the addition of this ξ_{min} term allows for cycling in cases where the phase transformation does not undergo complete reverse phase transformation. After substitution and simplification, it is possible to express $\dot{d}$ explicitly as a function of $\dot{\xi}$ as shown in Eq. 5.7, where f^d is defined in Eq. 5.8.

$$\dot{d} = f^d \dot{\xi} \qquad (5.7)$$

102

$$f^d = \begin{cases} \frac{c_1}{\tilde{N}} \frac{1.905\xi}{N_f} + c_3 c_4 \frac{1.905\xi}{N_f} e^{c_4 \tilde{N}}, \dot{\xi} > 0 \\ 0, \dot{\xi} \leq 0 \end{cases} \tag{5.8}$$

A further assumption of the model is that damage either remains constant or grows, that is $\dot{d} \geq$ 0. As a direct consequence of this non-negative damage accumulation restriction, it is therefore possible to impose restrictions on the values of c_1, c_3, and c_4 based on Eq. 5.3 in conjunction with the definition of $\tilde{N}$, defined as the percentage of actuation fatigue lifetime. Starting with the assumption damage does not reduce and then substituting in Eq. 5.3 leads to:

$$\dot{d} \geq 0 \tag{5.9}$$

$$\frac{c_1}{\tilde{N}} \dot{\tilde{N}} + c_3 c_4 \dot{\tilde{N}} e^{c_4 \tilde{N}} \geq 0 \tag{5.10}$$

After rearrangement to find c_1 it is found that

$$c_1 \geq -\tilde{N} c_3 c_4 e^{c_4 \tilde{N}} \tag{5.11}$$

Recalling the $\tilde{N}$ varies from 0 (beginning of life) to 1 (end of life), it is therefore possible to place restrictions on the possible values of c_1. Specifically, at the beginning of life, $\tilde{N} = 0$, which therefore limits the acceptable values of c_1 such that

$$c_1 \geq 0 \tag{5.12}$$

The restriction on c_1 clearly implies that c_1 cannot be negative. From a thermodynamic perspective, this restriction makes sense because damage cannot be negative. In the case where c_1 is 0, this would lead to no rapid initial damage nucleation (in conjunction with the logarithmic term assumed in Eq. 5.2), but rather the damage would be controlled by the exponential growth terms, in agreement with many other damage accumulation models in the literature for classical materials.

Moving on to c_3 and c_4, it is possible to rearrange Eq. 5.10 in order to get a relation between these values.

$$c_3 c_4 e^{c_4 \tilde{N}} \geq -\frac{c_1}{\tilde{N}} \qquad (5.13)$$

Solving explicitly for c_3 as a function of c_1 and c_4, it is found that

$$c_3 \geq -\frac{c_1}{\tilde{N} c_4 e^{c_4 \tilde{N}}} \qquad (5.14)$$

Recalling that this constant value of c_3 must be applicable for the entire actuation fatigue lifetime, it is therefore useful to examine the most restrictive case based on the percentage of actuation fatigue lifetime. As such, for $\tilde{N} = 1$, this leads to

$$c_3 \geq -\frac{c_1}{c_4 e^{c_4}} \qquad (5.15)$$

From an implementation perspective, this restriction on the possible values of c_3 is necessary similarly in order to maintain a non-negative growth of damage. For cases when the value of c_3 is negative (but still greater than this restriction), this leads to an exponential decay in the damage growth rate. Specifically, in the case where c_3 is exactly equal to the right hand side of Eq. 5.15, the damage growth rate at the end of the actuation fatigue life is 0. For the case when $c_3 = 0$, this means that the exponential term is 0 and damage only accumulates in accordance with the logarithmic term. For positive values of c_3, this means that the damage will exponentially grow at the end of life.

Based on the experimental damage data from Ch. 4, it is expected that the values of c_1 and c_3 should be positive, which is an acceptable result given the restrictions on the values of these parameters utilizing the assumption that damage growth is non-negative. Indeed, utilizing a least squares fitting method, the values of c_1, c_3, and c_4 are determined in order to match the experimental damage accumulation curve. The resulting values for c_1, c_3, and c_4, as well as the additional damage accumulation parameters are shown in Table 5.1. As shown in Fig. 5.3, comparing the resulting

Table 5.1: Damage Evolution Parameters

Parameter	Value
c_1	$3.159 x 10^{-3}$
c_3	$2.752 x 10^{-6}$
c_4	10.87
D_{crit}	0.191
C^d	3231.3
γ_d	-0.672

damage evolution curve from this non-linear damage accumulation curve to the experimental data shows a much closer fit to the experimental data than the linear damage evolution curve assumed by prior works.

Since an experimentally derived damage evolution curve has been obtained, it is now possible to utilize this non-linear damage evolution model within the global framework of a SMA constitutive model and determine the actuation fatigue lifetime based on the evolution of damage up to the damage at the end of the fatigue lifetime, d_{crit}, as determined experimentally.

5.1.2   Inclusion of Damage into Existing Constitutive Model

The proposed damage evolution model has been utilized to augment the constitutive model developed by Lagoudas et al. [95]. In this model, the total Gibbs free energy, G, is additively decomposed into 3 contributions composed of an austenitic thermoelastic contribution, G^A, a martensitic thermoelastic contribution, G^M, and a mixing term due to the interaction between austenite and martensite, G^{mix} as shown in Eq. 5.16.

$$
\begin{aligned}
G(\sigma, T, \epsilon^t, \xi, g^t) &= (1 - \xi)G^A(\sigma, T) + \xi G^M(\sigma, T) \\
&\quad + G^{mix}(\sigma, \epsilon^t, g^t)
\end{aligned}
\tag{5.16}
$$

In this model, the austenitic and martensitic contributions to the total Gibbs free energy are assumed to be of the form in Eq. 5.17, replacing γ with A or M for austenite or martensite respec-
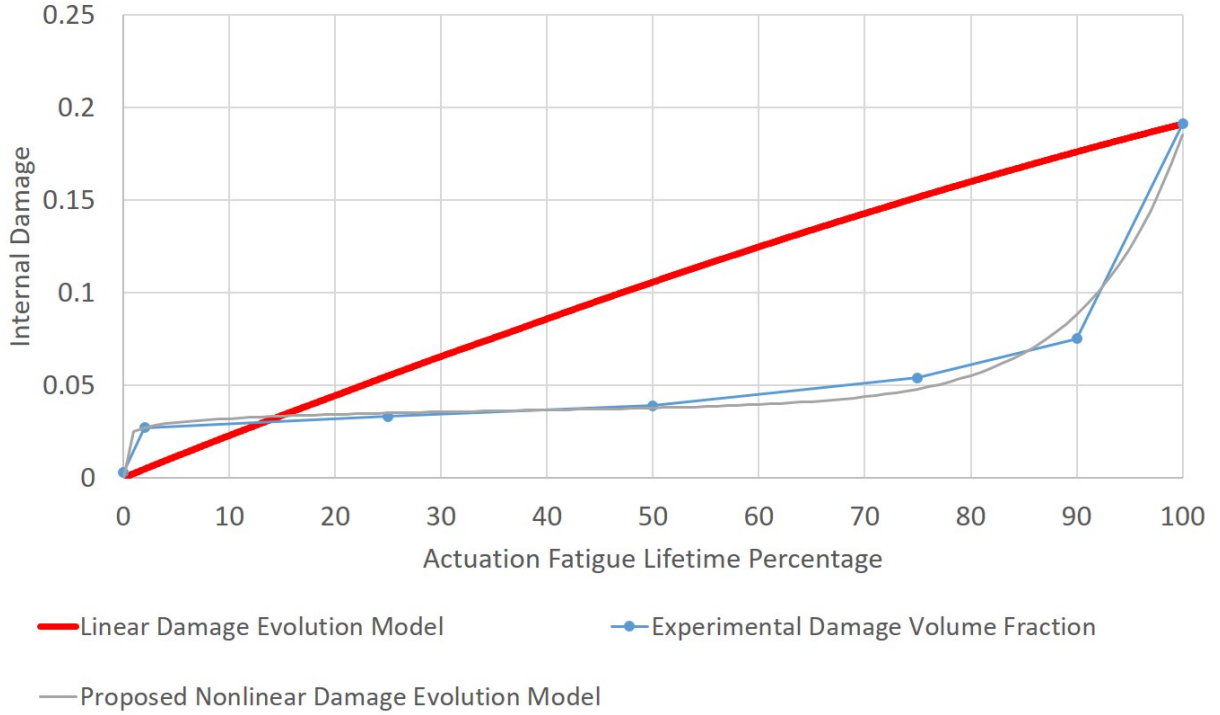
Figure 5.3: Comparison of Internal Damage Evolution as determined experimentally versus a linear model and the proposed non-linear damage evolution model.

tively. [1].

$$
\begin{aligned}
G^\gamma(\sigma, T) \;=\; & -\frac{1}{2\rho}\sigma : \mathbf{S}^\gamma \sigma - \frac{1}{\rho}\sigma : \alpha(T - T_0) \\
& + c^\gamma[(T - T_0) - T\ln(\frac{T}{T_0})] - s_0^\gamma T + u_0^\gamma
\end{aligned}
\tag{5.17}
$$

However there is currently no explicit introduction of damage in any of the portions of this model. Therefore, it is hereby proposed to augment the elastic portions of the austenitic and martensitic contributions to the total Gibbs free energy with a dependence on the current state of damage. Taking the elastic portion of the Gibbs free energy for austenite and martensite, and following the addition of damage into the SMA constitutive model of Chemisky et al [94], the

---

[1]The operation denoted by (-:-) indicates the inner product of two second-order tensors

elastic portion of the Gibbs free energy for austenite and martensite is modified as shown in Eq. 5.18.

$$G_{el}^{\gamma}(\sigma, d) = -\frac{1}{2\rho(1-d)}\sigma : \mathbf{S}^{\gamma}\sigma \tag{5.18}$$

Thus, the modified austenitic and martensitic Gibbs free energy can be written as

$$
\begin{aligned}
G^{\gamma}(\sigma, T, d) &= -\frac{1}{2\rho(1-d)}\sigma : \mathbf{S}^{\gamma}\sigma - \frac{1}{\rho}\sigma : \alpha(T - T_0) \\
&\quad + c^{\gamma}[(T - T_0) - T\ln(\frac{T}{T_0})] - s_0^{\gamma}T + u_0^{\gamma}
\end{aligned}
\tag{5.19}
$$

No change is proposed to the energy of mixing, which is given as

$$G^{mix}(\sigma, \epsilon^t, g^t) = -\frac{1}{\rho}\sigma : \epsilon^t + \frac{1}{\rho}g^t \tag{5.20}$$

The definition of the evolution equations for the transformation strain, ϵ^t and hardening energy, g^t follow the definitions presented by Lagoudas et al. [95]. Once the evolution laws for the internal state variables are defined, in order to ensure that the proposed model is thermodynamically consistent, it is necessary to ensure satisfaction of the conservation laws as well as the laws of thermodynamics. Utilizing conservation of mass, linear momentum, and angular momentum, it is possible to write the first law of thermodynamics in local form as

$$\rho\dot{u} = \sigma : \dot{\epsilon} - div(\mathbf{q}) + \rho r \tag{5.21}$$

where ρ is the density, u is the internal energy, $\mathbf{q}$ is the heat flux vector, and r is the rate of internal heat generation.

Moving to the second law of thermodynamics, the local form can be written in the form of the Clausius-Planck inequality [114].

$$\rho \dot{s} + \frac{1}{T} div(\mathbf{q}) - \frac{\rho r}{T} \geq 0 \qquad (5.22)$$

Multiplying Eq. 5.22 by T leads to

$$\rho \dot{s} T + div(\mathbf{q}) - \rho r \geq 0 \qquad (5.23)$$

Comparing Eq. 5.23 with Eq. 5.21, it is now possible to eliminate the $div(\mathbf{q})$ term as well as drop some terms which cancel, leading to the form of the second law of thermodynamics as shown in Eq. 5.24.

$$\rho \dot{s} T - \rho \dot{u} + \sigma : \dot{\epsilon} \geq 0 \qquad (5.24)$$

It is now useful to recall the relationship between the Gibbs free energy G and the internal energy u which are related through the *Legendre transformations*, as defined in Eq. 5.25.

$$G = u - \frac{1}{\rho} \sigma : \epsilon - sT \qquad (5.25)$$

Taking the time rate of change of Eq. 5.25, and re-arranging such the $\dot{u}$ is on the left side of the equality gives

$$\dot{u} = \dot{G} + \frac{1}{\rho}(\dot{\sigma} : \epsilon + \sigma : \dot{\epsilon}) - \dot{s}T - s\dot{T} \qquad (5.26)$$

Substituting Eq. 5.26 into Eq. 5.24 and after simplification yields

$$- \rho \dot{G} - \dot{\sigma} : \epsilon - \rho s \dot{T} \geq 0 \qquad (5.27)$$

If the chain rule is now applied in order to determine $\dot{G}$, based on the internal state variables as determined from Eqs. 5.19 and 5.20, it is possible to expand Eq. 5.27 into [2]

---

[2]The notation $\partial_T G$ indicates the partial derivative of G with respect to T

$$- \rho(\partial_\sigma G : \dot{\sigma} + \partial_T G \dot{T} + \partial_{\epsilon^t} G : \dot{\epsilon^t} + \partial_\xi G \dot{\xi} + \partial_{g^t} G \dot{g}^t + \partial_d G \dot{d}) - \dot{\sigma} : \epsilon - \rho s \dot{T} \geq 0 \qquad (5.28)$$

Following the Coleman and Noll procedure [115], it is possible to determine the following relations for the total infinitesimal strain and specific entropy, as shown in Eqs. 5.29 and 5.30, respectively.

$$\epsilon = -\rho \partial_\sigma G = \frac{1}{(1-d)} \mathbf{S}\sigma + \alpha(T - T_0) + \epsilon^t \qquad (5.29)$$

$$s = \frac{1}{\rho}\sigma : \alpha + c \ln(\frac{T}{T_0}) + s_0 \qquad (5.30)$$

At this point, the remaining dissipative terms in the second law of thermodynamics after cancellation of terms following the Coleman and Noll procedure are given in Eq. 5.31.

$$- \rho(\partial_{\epsilon^t} G : \dot{\epsilon^t} + \partial_\xi G \dot{\xi} + \partial_{g^t} G \dot{g}^t + \partial_d G \dot{d}) \geq 0 \qquad (5.31)$$

The first three remaining dissipative terms represent the *generalized thermodynamical forces* as defined by Qidwai and Lagoudas [116]. These generalized thermodynamical forces are written as

$$- \rho \partial_\xi G = p^\xi; \qquad -\rho \partial_{\epsilon^t} G = \sigma; \qquad -\rho \partial_{g^t} G = -1 \qquad (5.32)$$

Due to the definition of p^ξ as a partial of the Gibbs free energy with respect to the martensitic volume fraction, ξ, and due to the addition of damage into the Gibbs free energy as defined in Eq. 5.19, therefore there will be an additional term in the p^ξ generalized thermodynamical force beyond that shown in Lagoudas et al [95]. Thus the p term becomes

$$p^\xi = \frac{1}{2(1-d)}\sigma : \Delta S \sigma + \sigma : \Delta\alpha(T - T_0) - \rho\Delta c[(T - T_0) - T\ln(\frac{T}{T_0})] + \rho\Delta sT - \rho\Delta u_0 \quad (5.33)$$

In addition to these generalized thermodynamical forces based on the first three terms of Eq. 5.31, it is here also necessary to define a fourth generalized thermodynamical force in order to account for the damage term. Therefore, based Eq. 5.31 this fourth generalized thermodynamic force is in direct relation to the partial derivative of the Gibbs free energy, G with respect to damage, d and can be written as shown in Eq. 5.34.

$$p^d = -\rho\partial_d G = \frac{1}{2(1-d)^2}\sigma : \mathbf{S}\sigma \quad (5.34)$$

which leads to the following form of the second law of thermodynamics.

$$(\sigma : \mathbf{\Lambda}^t + p^\xi - f^t + p^d f^d)\dot{\xi} = \pi^t\dot{\xi} \geq 0 \quad (5.35)$$

In this final form of the second law of thermodynamics, π^t denotes the *total thermodynamic force* conjugate to ξ. From this point, the *total thermodynamic force* is used in order to define when transformation is expected to occur in accordance with the model of Lagoudas et al. [95].

5.2 Results

For preliminary verification of the model described in the preceding section, the model has been implemented into a MATLAB program for rapid prediction of the effects of cyclic loading on the behavior of an SMA. Utilizing the modified constitutive model developed in the previous section, it is now shown how this model captures the damage behavior of the SMA. The material parameters used for the simulations are shown in Table 5.2, in addition to the damage parameters previously shown in Table 5.1.

Based on these parameters, it is possible to predict the evolution of damage within a SMA subjected to cyclic thermal actuation. For a SMA actuator subjected to a constant 400 MPa load,

Table 5.2: Material Parameters

Parameter	Value
E_A	80 GPa
E_M	60 GPa
A_S	200 °C
A_F	215 °C
M_S	175 °C
M_F	155 °C
C_A	$7 \frac{MPa}{°C}$
C_M	$7 \frac{MPa}{°C}$
α_A	$2.2x10^{-5}$
α_M	$2.2x10^{-5}$
H_{min}	0
H_{sat}	0.028
k	0.0172 MPa^{-1}
$\bar{\sigma}_{crit}$	120 MPa

the damage accumulation predicted is shown in Fig. 5.4. Due to the direct impact of damage on the elastic portion of the total Gibbs free energy, the evolution in damage in turn has a direct impact on the effective modulus as well as the elastic strain as shown in Figs. 5.5 and 5.6, respectively.

In addition to demonstrating a good fit between the evolution of damage as determined from the numerical and experimental results, it is also useful to demonstrate that the proposed model is capable of predicting the actuation fatigue lifetime of SMA actuators under multiple loading conditions. Such a comparison is provided in Table 5.3. As can be seen, the proposed implementation is capable of predicting the actuation fatigue lifetime not only for constant load conditions, but is also capable of predicting the actuation fatigue lifetime for SMA actuators subjected to variable loading conditions. Furthermore, the model is shown to be able to predict the actuation fatigue lifetime with a better match to experimental results in most cases as compared to previous work which utilized the fatigue life indication parameter method as discussed by Wheeler [87].

After initial confirmation of the suitability of the proposed model to capture the evolution of internal damage, the full model has also been implemented into a user material subroutine (UMAT) for use in the finite element modeling software ABAQUS. Utilizing the UMAT developed based
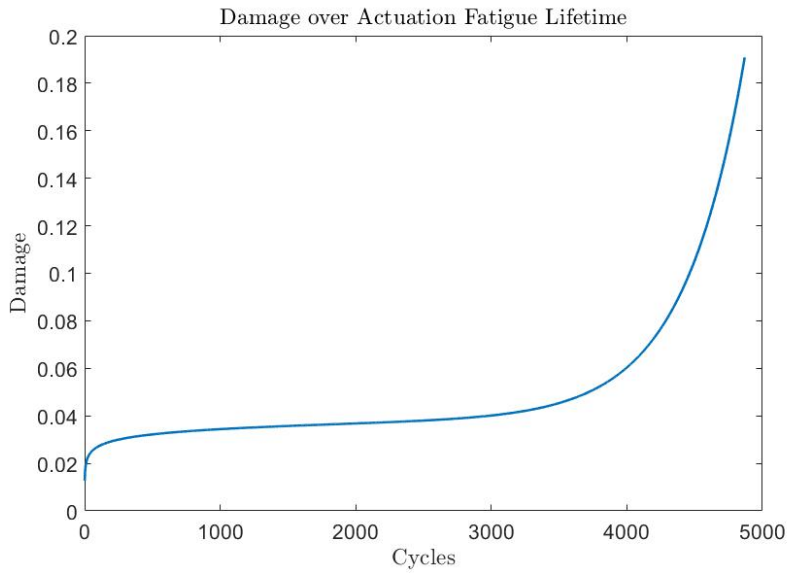
Figure 5.4: Evolution of damage during actuation fatigue lifetime in a SMA actuator subjected to 400 MPa tensile load.
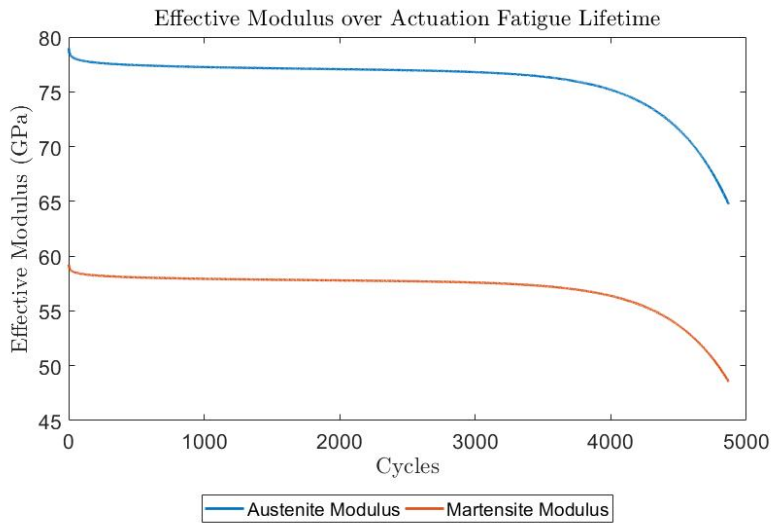
Figure 5.5: Evolution of effective modulus during actuation fatigue lifetime in a SMA actuator subjected to 400 MPa tensile load.
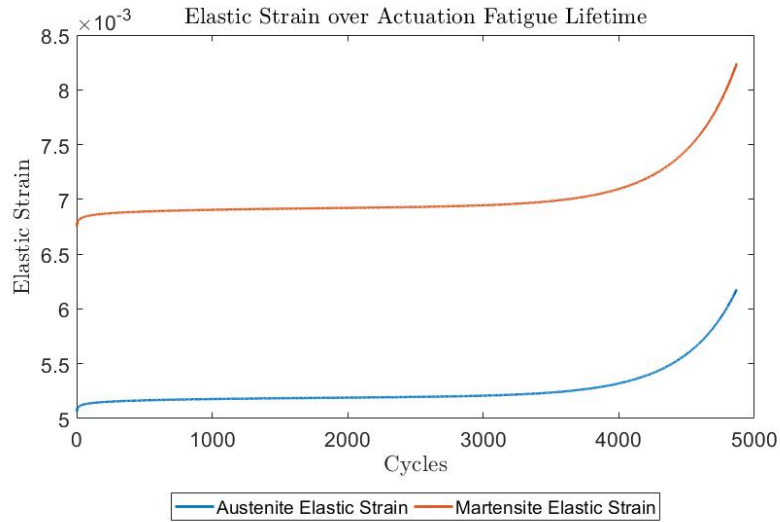
Figure 5.6: Evolution of elastic strain during actuation fatigue lifetime in a SMA actuator subjected to 400 MPa tensile load.

Table 5.3: Comparison of predicting and experimental actuation fatigue lifetimes for multiple loading conditions

Load Path	Min Stress (MPa)	Max Stress (MPa)	Experimental Cycles to Failure	Predicted Cycles to Failure	Prior Work
Constant	200	200	21258	19116	23432
Constant	300	300	9742	7826	8126
Constant	400	400	4889	4869	4581
Linear	300	400	6605	6521	6357
Linear	300	500	5263	5567	4787

Figure 5.7: Uniaxial truss element actuation fatigue modeling test specimen

on the Lagoudas et al. model from 2012 [95], the necessary modifications to this UMAT were completed in order to include damage based on the equations derived in Sec. 5.1.2. In terms of implementation, the UMAT assumes that the local damage from the previous time increment applies to the current time increment, and the local damage is updated as an additional subfunction at the end of the UMAT. For verification that the implementation of the damage model in the UMAT was correctly completed, two test cases were run. These test cases were for a simple 1 element uniaxial truss as shown in Fig. 5.7.

The uniaxial truss element was simulated first in order to verify that the UMAT would run properly. As mentioned, the damage model was implemented into the UMAT through modification of an existing UMAT based on the SMA constitutive model from Lagoudas et al. [95]. Therefore, after the necessary modifications for the damage model were introduced, this simple uniaxial truss model verified that the model could still run properly, and that the quantities of interest for the damage model were properly captured. Specifically, in order to utilize the implementation in order to determine actuation fatigue life for arbitrary shapes and loading paths, it was necessary to determine the evolution of damage throughout the entire specimen. For the uniaxial truss element, this means that the damage at all points should evolve in the same manner. Therefore, in order to allow for modeling of the uniaxial truss element under conditions of interest, and in order to be compara-
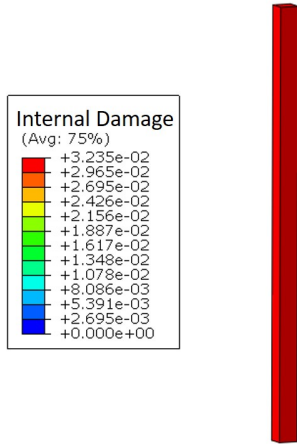
Figure 5.8: Uniaxial truss element damage after 1200 thermal actuation cycles subject to 400 MPa
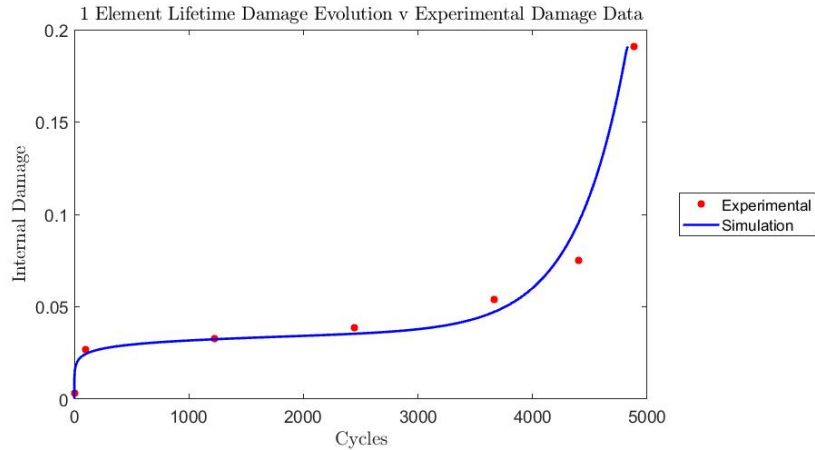
Figure 5.9: Evolution of damage in uniaxial truss element specimen over entire actuation fatigue lifetime subject to 400 MPa

ble with the experimental results gathered in Ch. 4 as well as in other actuation fatigue works, the top side of the specimen was fixed, while a pressure load was applied to the bottom face, resulting in a stress of 400 MPa throughout the specimens. After application of the load, the temperature was cycled from 300 °C to 150 °C, as such mimicking the experimental actuation fatigue cycling conducted at 400 MPa. Indeed this was captured correctly in that the damage throughout the entire specimen evolved in the exact same way, as shown in Fig. 5.8 after 1200 cycles. Similarly, it was necessary to ensure that damage evolved in the expected non-linear manner, which is captured for the entire actuation fatigue lifetime in Fig. 5.9.

5.3 Coupling Damage Evolution with Stress Redistribution

Over the preceding chapters, it has been discussed how the stress redistributes in the presence of a stress concentration due to phase transformation within a single phase transformation cycle for a SMA (based on Ch. 2 and Ch. 3), as well as how damage (stress concentrators) will tend to nucleate and grow during actuation fatigue (based on Ch. 4 and Ch. 5). Based on these results, it is now possible to predict the behavior of a SMA actuator within each phase transformation

cycle throughout the actuation fatigue lifetime of the SMA component. In order to demonstrate this capability within a practical engineering application, it is possible to consider the effect of a notch within a flat plate as could be found in many engineering structures. To this end, a notched flat plate has been modeled under constant axial loading conditions while the plate is thermally actuated. The notched plate under consideration is shown in Fig. 5.10. In this notched plate, the plate is 0.5 mm thick, the plate area has a width of 10 mm, and the notch has a radius of 1.5 mm, with a 0.5 mm offset from the edge, leading to a width of 8 mm along the plane of minimum width. The plate is fixed at the bottom and loaded along the top surface to 50 MPa while at 300 °C. The temperature is then thermally cycled from 300 °C down to 150 °C and back up to 300 °C.

Figure 5.10: Notched plate utilized to study combined effects of stress redistribution and damage evolution during cyclic thermal actuation.

As was shown in the notched cylinders studied in Ch. 2, the presence of the notch in the notched plate is also expected to lead to a multiaxial state of stress eminating from the notch which acts as a stress concentration. Zooming in on the area close to the notch, the presence of a complex stress field is indeed present as evidenced in austenite in Fig. 5.11. Furthermore, also in agreement with Ch. 2, it is also shown in Fig. 5.11 that the von Mises stress redistributes as a function of

phase transformation during forward phase transformation. The unique addition in this chapter is that now the evolution of damage can also be studied as a function of the phase transformation, as shown in the bottom row of Fig. 5.11 for the first thermal actuation cycle.

	Austenite	During Phase Transformation	Martensite
Stress			
Temperature			
Damage			
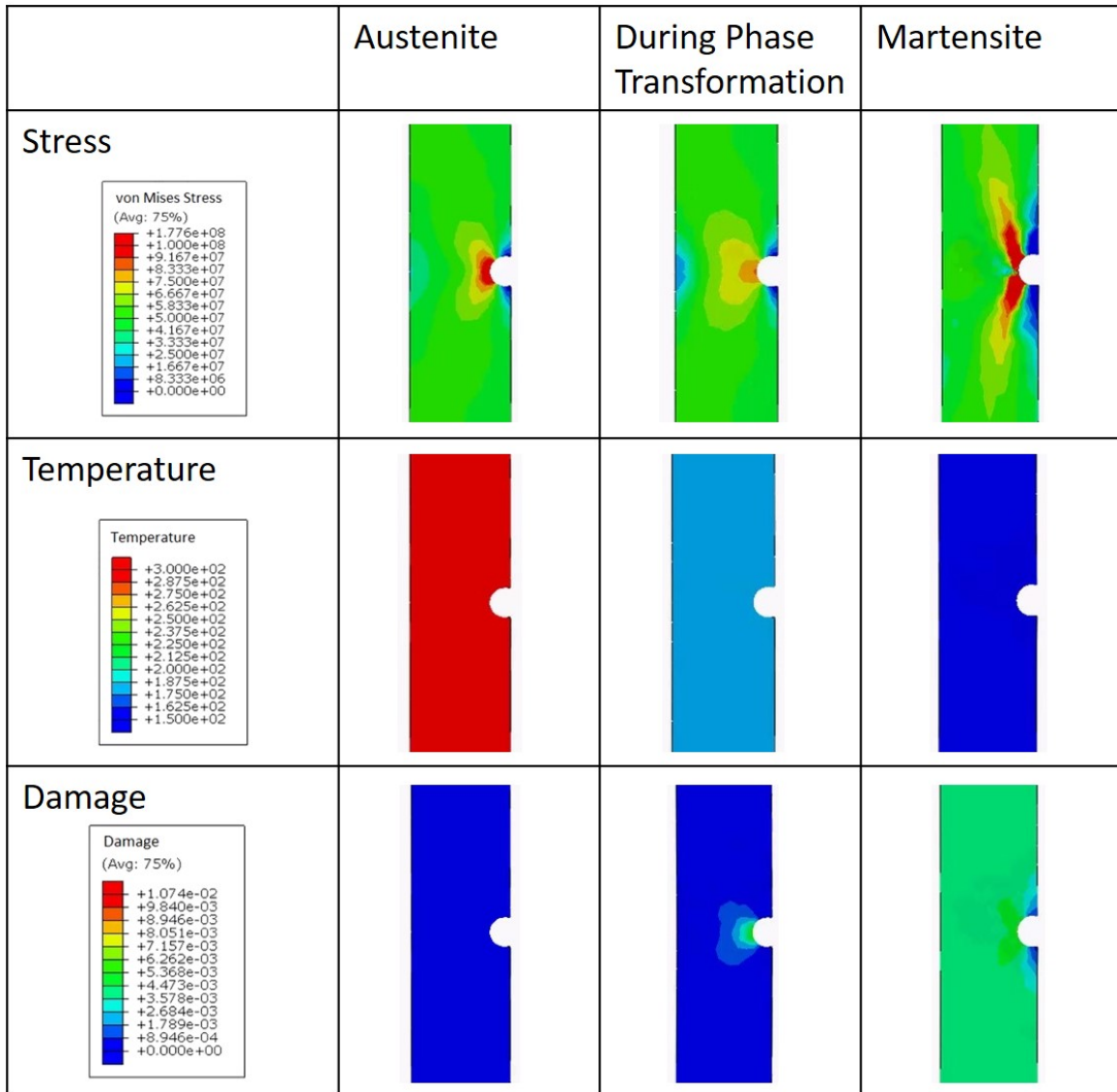
Figure 5.11: Evolution of temperature, von Mises stress, and internal damage during the first thermal actuation cycle of a notched plate subjected to 50 MPa at the outer surface

Furthermore, it is also possible to study the evolution of the stress and damage as a function of repeated thermal actuation, which would be a primary goal of this work. As shown in Fig.

5.12, it is indeed possible to capture this evolution of damage over multiple thermal actuation cycles. The data clearly indicates that the damage is highest along the notch wall in the plane of minimum width. This is expected and does match with the location at which failure is shown to occur experimentally for this type of notched plate, as was shown by Wheeler et al. [117].
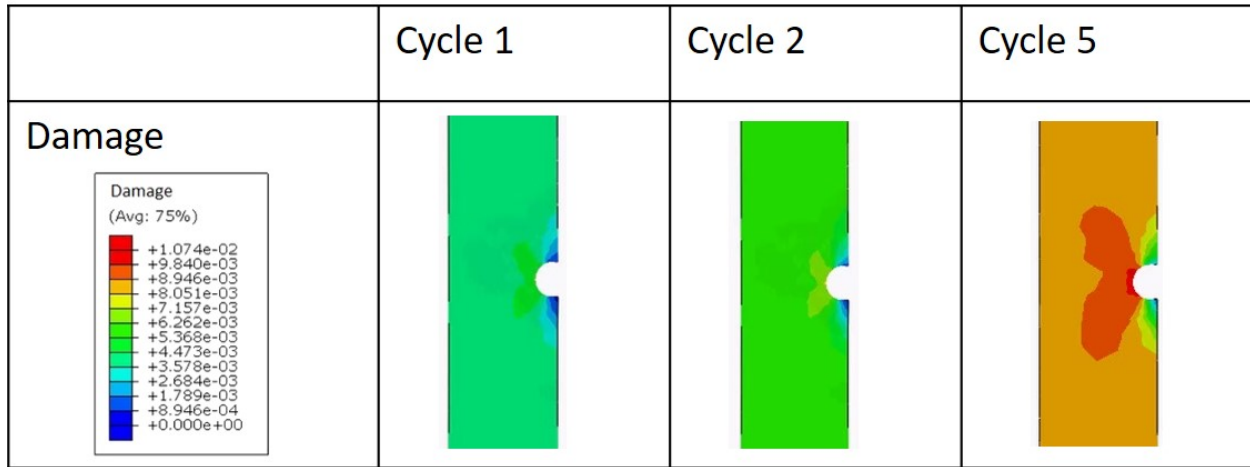
Figure 5.12: Evolution of internal damage in notched plate over 5 actuation cycles

5.4 Conclusion

The fracture of SMA structures subjected to actuation fatigue is a key area of research which requires careful analysis in order to enable the use of SMAs in a number of new applications. Based on the X-ray μCT scans performed, the accumulation of damage progresses in a non-linear manner in SMA actuators as a function of actuation fatigue lifetime. As such, an internal damage evolution model has been developed and introduced into a SMA constitutive model. Utilizing this non-linear damage evolution model implemented within the SMA constitutive model has enabled the prediction of the actuation fatigue lifetime of a SMA component, and the predicted fatigue lifetime shows a close match to experimental results for a variety of both constant and variable loading conditions. The developed model can hence be utilized to predict the actuation fatigue lifetime of a SMA actuator. The power of this model is in the flexibility to determine the actuation fatigue

lifetime of a SMA actuator under varying mechanical loading conditions. In turn, this ability to handle varying mechanical loading conditions will allow for the analysis of SMA components in structures where-in the loading conditions are beyond the standard isothermal or isobaric loading conditions, as will be experienced in most practical applications.

6. SUMMARY AND CONCLUSION

Considerable interest exists in the use of Shape Memory Alloys (SMAs) across a number of different industries, including the aerospace, biomedical, oil and gas, automotive, and civil industries. The primary reason for this interest is due to the thermomechanically induced phase transformation which these alloys exhibit. However considerable work remains to be performed in order to truly understand how these materials behave and why they do what they do. It is important to understand the behavior of these alloys both during each individual phase transformation cycle as well as throughout the lifetime of these alloys.

In this work, various phenomena related to the lifetime of a SMA component have been analyzed, starting first with the effect of a stress concentration in a single phase transformation cycle and then looking at how such stress concentrations evolve during the actuation fatigue lifetime of a SMA component. Specifically, the effect of the phase transformation on the stress redistribution during a single phase transformation cycle has been analyzed, followed by analysis of the damage evolution throughout the entire lifetime of a SMA actuator. Both the single phase transformation cycle and the full lifetime of a SMA actuator have been analyzed through a combination of numerical and experimental techniques. The numerical methods used allow for a wide range of analysis to be conducted and for the development of various models to attempt to phenomenologically capture the behavior of SMAs. In addition, the experimental studies conducted serve as validation points for some of the numerical results obtained. The careful, collaborative use of both types of analysis methods is required in order to explore a wide range of possible material phenomena through numerical methods, while ensuring that at least part of the results obtained numerically are validated experimentally with what actually occurs in the material.

6.1   Simulation of Stress Redistribution in Notched Cylindrical Shape Memory Alloys

During phase transformation, it is well known that the stress within the phase transforming material will change. This is no different for SMAs. However the novelty for SMAs is that the

phase transformation is thermomechanically induced. Therefore, as the stress changes within a SMA during phase transformation, it is therefore not unexpected that the stress redistribution could have an effect on the phase transformation. However the extent to which this stress redistribution affects the phase transformation is interesting, particularly for SMAs with stress concentrations.

Utilizing notched cylindrical SMA bars, it has been shown that the stress redistribution has a significant impact on the phase transformation, regardless of the thermomechanical path utilized to induce phase transformation. For both the pseudoelastic (isothermal) as well as the thermal actuation (isobaric) loading paths, it has been shown that the phase transformation propagation is highly dependent on the size of the notch acuity, defined as the ratio of the radius of the plane of minimum cross section, a, to the radius of the notch, R. Analysis of a range of notch acuity for specimens under thermal actuation found that for notch acuities below 0.4 ($\frac{a}{R} < 0.4$) the phase transformation initially goes through the plane of minimum cross-section and then propagates above/below this plane. For notch acuities greater than 2.5 ($\frac{a}{R} > 2.5$), the phase transformation initially propagates from the notch wall at the plane of minimum cross-section in a spherical pattern, leading to shielding of stress in the rest of the plane of minimum cross-section and therefore causing the rest of this plane to transform last.

For intermediate notch acuities ($0.4 < \frac{a}{R} < 2.5$), a mixture of these phase transformation propagation patterns exist. The mixture in phase transformation propagation patterns actually leads to some very interesting behavior for these specimens, including phase transformation reversal. While under constant load, the simulations showed that cooling of the specimens lead to forward phase transformation, which in turn lead to stress redistribution as the phase transformation progress. However due to the stress redistribution, the stress in certain regions near the central axis reduce so far that they start to experience reverse phase transformation even though the temperature continues to drop. Indeed it was shown that for the $\frac{a}{R} = 1.25$ specimen, the stress redistribution due to phase transformation can lead to phase transformation reversal of up to 18% along the central axis on the plane of minimum cross section.

Another impact of the stress redistribution for specimens in this intermediate range of notch

acuities is a strong variation in the triaxiality ratio. As has been shown, the triaxiality in the these specimens can change drastically during phase transformation due to the stress redistribution. The phase transformation and associated stress redistribution have been shown to cause certain areas to go into compressive hydrostatic states of stress (due to the spherical phase transformation propagation pattern), while other areas go into extremely high tensile hydrostatic states of stress. The effect of the stress redistribution during phase transformation is clearly very significant.

6.2 Experimental Validation of the Effect of Stress Redistribution during Phase Transformation in Notched Cylindrical Shape Memory Alloy Bars

The results presented in Ch. 2 provide some interesting insight into the possible mechanisms at play during phase transformation in SMAs with stress concentrations. However some level of experimental proof is necessary in order to be able to claim that the phenomena presented are truly occurring within SMA material. It has therefore been shown experimentally that the surface level strain measurements do correspond well between the numerical and experimental results for both pseudoelastic as well as thermal actuation loading paths. These surface level measurements were made through the collaborative use of digital image correlation (DIC), laser extensometry, as well as optical extensometry.

Furthermore, the use of a scanning electron microscope (SEM) allowed for investigation of the fracture surface of the SMA notched cylindrical bars. It has been shown that for a notch acuity of 2.5 ($\frac{a}{R} = 2.5$), the fracture appears to initiate at the notch wall and subsequently propagate inwards through the remainder of the material. This SEM experimental observation is in agreement with the numerical results which indicate that the during forward phase transformation, the spherical phase transformation propagation pattern will tend to localize stress at the notch wall, thereby causing an excessively high stress near the wall which would therefore serve as a fracture initiation site. In contrast, for a notched cylindrical SMA bar with a notch acuity of 0.5 ($\frac{a}{R} = 0.5$), the SEM micrographs suggest that fracture initiated in the center of the specimen. When comparing to the numerical simulations, the fracture in the center of the specimen could be tied back to an increase in the triaxiality of the specimen along the central axis of the specimen.

Finally, a series of experiments were also conducted at Oak Ridge National Laboratory, in which notched cylindrical SMA bars were exposed to a neutron beam in order to utilize neutron diffraction to determine the crystal structure of the notched cylindrical SMA bars through the plane of minimum cross-section as a function of temperature. The preceding methods do not allow for live determination of the phase of the material during testing as DIC and extensometry measurements only provide surface level details and SEM was performed post-mortem. However the neutron diffraction experiments were conducted in-situ during thermal cycling. Although the neutron diffraction experiments do not clearly identify phase transformation reversal, the results do suggest that for the $\frac{a}{R} = 1.25$ specimen, the phase transformation appears to pause during cooling, which is another phenomena that was identified in the numerical simulation results. Therefore, to the extent possible with the various experimental techniques utilized, it was possible to validate experimentally a portion of the numerical results presented for notched cylindrical SMA bars.

6.3 Characterization of Damage Evolution during Actuation Fatigue

Most SMA applications will require the SMA to undergo cyclic phase transformation. As such, it is important to understand how the SMAs will behave throughout their lifetime. When SMAs are used in a number of applications, it is likely that the phase transformation will be thermally induced. However the motion of the atoms within a SMA while it is undergoing cyclic phase transformation will eventually lead to failure due to actuation fatigue.

In studying the actuation fatigue lifetime of SMAs, it is possible to observe the fact that the elastic and transformation behavior evolve as a function of the number of thermal actuation cycles. This study has shown that this evolution is indeed a very local behavior, in that the local strains evolve differently at each material point. Furthermore, surface level observations identified the formation of cracks throughout the surface of the material, which can help explain the localized strain variations is identified through DIC.

The key contribution of this work to the understanding of the evolution of damage in SMAs during actuation fatigue is through the quantification of internal damage through the use of X-Ray Computed MicroTomography (X-Ray μCT). Multiple actuation fatigue specimens were cycled to

various predicted actuation fatigue lifetimes (2%, 25%, 50%, 75%, 90%) and imaged with X-Ray μCT in order to determine how the internal damage changed as a function of these lifetimes. For reference, a pre and a post failure specimen were also imaged. The data shows a highly non-linear evolution in internal damage, with a quick rise at the beginning of life, followed by a slow and steady increase, until an exponential increase in internal damage near the end of life.

Further validation of this damage evolution was determined through analysis of the evolution of the effective elastic modulus for SMA specimens subjected to actuation fatigue. The data shows the the effective modulus is nearly constant through approximately 70% of the actuation fatigue lifetime, and then shows a decrease until the end of life.

6.4 Modeling of Damage Evolution during Actuation Fatigue

Based on the X-ray μCT results presented in Ch. 4 as well as a survey of the existing actuation fatigue damage models, it was determined that a new model able to capture the non-linear damage evolution was needed. As such a new formulation for the damage evolution is introduced, incorporating two non-linear terms. The first term accounts for the rapid growth of damage at the beginning of the actuation fatigue lifetime due to the motion of dislocations as a function of phase transformation. It is proposed that the phase transformation propagation fronts carry dislocations which were introduced into the material during forming and processing. In turn as these dislocations pill up, they tend to nucleate the damage identified at an early actuation fatigue lifetime as shown through the X-Ray μCT results. However as all these dislocations pill up, there is progressively less dislocations able to move, thereby reducing the damage nucleation rate, leading into the slow growth in damage throughout the intermediate portion of the actuation fatigue lifetime. Once damage has nucleated within the material, it will tend to slowly grow within the material until the damage locations tend to coalesce. This growth and coalescence rate tends to behave exponentially, particularly near the end of the actuation fatigue lifetime.

Using this proposed damage nucleation and growth model, an existing SMA phenomenological constitutive model was modified in order to account for this damage growth. This required the re-derivation of the model, starting with a modified Gibbs free energy function. Based on the mod-

ified Gibbs free energy, a thermodynamically consistent procedure was utilized to determine four generalized thermodynamical forces which govern the dissipation of energy in accordance with the second law of thermodynamics. This modified SMA constitutive model was then implemented into various simulation software in order to validate the model. Comparison of the model results for the predicted lifetime of a SMA component to the experimentally obtained lifetime shows good agreement for both static as well as linearly changing loads.

6.5   Conclusion

In conclusion, it has been shown that the entire lifetime of a SMA component subjected to fatigue must be carefully analyzed in order to understand what is happening within a single phase transformation cycle, and how the damage formed within each phase transformation cycle can lead to further changes in the internal microstructure. In turn this change in the internal stress fields due to damage formation will lead to changes in the evolution of the phase transformation and a thorough understanding of the interplay between phase transformation, stress redistribution, and damage evolution must be established in order to properly model the entire lifetime of a SMA component. This work has made careful use of combined numerical and experimental methods in order to produce far more interesting results than an individual method alone. It is this careful, combined use of numerics and experiments to understand the behavior of a SMA component throughout its lifetime which will allow for the use of SMAs in a more widespread manner throughout a number of industries.

6.5.1   Future Work

The presented work has been able to successfully address a number of issues related to SMAs. However, it also highlights a number of open items that need to be addressed. One such item that requires further investigation is the interaction between damage and plasticity during repeated thermal actuation. Multiple researchers have seen that SMA behavior evolves as a function of the number of cycles a SMA undergoes. This evolution is frequently modeled through a combination of the generation of internal stresses as well as the introduction of transformation induced plas-

ticity (TRIP). However this work has clearly shown that the formation of damage is one of the contributing factors to the evolution of SMA behavior throughout the actuation fatigue lifetime. At the same time, results showing high levels of TRIP cannot be thoroughly accounted for due to the presence of damage (literature has shown it is possible to achieve more than 30% TRIP during the actuation fatigue lifetime). Therefore, there must be an interplay between TRIP generation and damage accumulation which should be further explored.

Another area which bears further exploration based on the X-Ray CT results presented in this work is the connection between damage formation and the two way shape memory effect (TWSME). Typically TWSME is induced in a SMA after some level of training, and it is generally agreed that the training introduces stresses in the material which promote this TWSME. However the present results show that damage accumulates quickly within the SMA during initial cycling. Therefore, it would be worth investigating the extent to which the stresses introduced by damage lead to the two way shape memory effect.

A further area of research from this work which bears further consideration is the combination of stress redistribution with the accumulation of damage. As shown in Ch. 2, phase transformation leads to the stress redistribution. In notched cylindrical SMA bars, this can have profound impacts on the thermomechanical response of the SMA. However these results were all presented within a single thermal cycle. As SMAs are introduced into additional thermal actuation based applications, it will be necessary to attach them to the structure, typically through the use of holes, rivets, screws, or other such stress concentrators. When the SMAs undergo phase transformation around these stress concentrators, the stresses will therefore redistribute. Therefore, under repeated phase transformation, the damage accumulation around these stress concentrators will need to properly accounted for in order to ensure safe usage of SMA actuators.

REFERENCES

[1] E. Hornbogen, "Review thermo-mechanical fatigue of shape memory alloys," *Journal of materials science*, vol. 39, no. 2, pp. 385–399, 2004.

[2] D. Lagoudas, ed., *Shape Memory Alloys: Modeling and Engineering Applications*. New York: Springer-Verlag, 2008.

[3] K. Otsuka and C. M. Wayman, eds., *Shape Memory Materials*. Cambridge: Cambridge University Press, 1999.

[4] A. Ölander, "An electrochemical investigation of solid cadmium-gold alloys," *American Chemical Society*, vol. 54, pp. 3819–3833, 1932.

[5] A. Greninger and V. Mooradian, "Strain transformation in metastable beta copper-zinc and beta copper-ti alloys," *AIME Transactions*, vol. 128, pp. 337–369, 1938.

[6] G. Kurdjumov and L. Khandros, "First reports of thermoelastic behavior of the martensitic phase of au-cd alloys," *Doklady Akademii Nauk SSSR*, vol. 66, pp. 211–213, 1949.

[7] L. Chang and T. Read, "Behavior of elastic properties of aucd," *Trans Met Soc AIME*, vol. 191, p. 47, 1951.

[8] W. Buehler, "Nitinol re-examination," *White Oak Laboratory Alumni Association Leaf*, vol. 8, 2006.

[9] W. J. Buehler, J. Gilfrich, and R. Wiley, "Effect of low-temperature phase changes on the mechanical properties of alloys near composition tini," *Journal of applied physics*, vol. 34, no. 5, pp. 1475–1477, 1963.

[10] G. Kauffman and I. Mayo, "The story of nitinol: the serendipitous discover of the memory metal and its applications," *Chem Educator*, vol. 2, pp. 1–21, 1997.

[11] J. Jani, M. Leary, A. Subic, and M. Gibson, "A review of shape memory alloy research, applications, and opportunities," *Materials and Design*, vol. 56, pp. 1078–1113, 2014.

[12] R. B. Zider and J. F. Krumme, "Eyeglass frame including shape-memory elements," Sept. 20 1988. US Patent 4,772,112.

[13] A. Hautcoeur and A. Eberhardt, "Eyeglass frame with very high recoverable deformability," June 17 1997. US Patent 5,640,217.

[14] D. J. Leo, C. Weddle, G. Naganathan, and S. J. Buckley, "Vehicular applications of smart material systems," in *Smart Structures and Materials 1998: Industrial and Commercial Applications of Smart Structures Technologies*, vol. 3326, pp. 106–117, International Society for Optics and Photonics, 1998.

[15] D. Stoeckel, "Shape memory actuators for automotive applications," *Materials & Design*, vol. 11, no. 6, pp. 302–307, 1990.

[16] C. Bil, K. Massey, and E. J. Abdullah, "Wing morphing control with shape memory alloy actuators," *Journal of Intelligent Material Systems and Structures*, vol. 24, no. 7, pp. 879–898, 2013.

[17] J. Van Humbeeck, "Non-medical applications of shape memory alloys," *Materials Science and Engineering: A*, vol. 273, pp. 134–148, 1999.

[18] L. M. Schetky, "Shape memory alloy applications in space systems," *Materials & Design*, vol. 12, no. 1, pp. 29–32, 1991.

[19] M. M. Kheirikhah, S. Rabiee, and M. E. Edalat, "A review of shape memory alloy actuators in robotics," in *Robot Soccer World Cup*, pp. 206–217, Springer, 2010.

[20] M. Sreekumar, T. Nagarajan, M. Singaperumal, M. Zoppi, and R. Molfino, "Critical review of current trends in shape memory alloy actuators for intelligent robots," *Industrial Robot: An International Journal*, vol. 34, no. 4, pp. 285–294, 2007.

[21] L. Sun, W. M. Huang, Z. Ding, Y. Zhao, C. C. Wang, H. Purnawali, and C. Tang, "Stimulus-responsive shape memory materials: a review," *Materials & Design*, vol. 33, pp. 577–640, 2012.

[22] L. Petrini and F. Migliavacca, "Biomedical applications of shape memory alloys," *Journal of Metallurgy*, vol. 2011, 2011.

[23] L. Machado and M. Savi, "Medical applications of shape memory alloys," *Brazilian journal of medical and biological research*, vol. 36, no. 6, pp. 683–691, 2003.

[24] L. Van Langenhove and C. Hertleer, "Smart clothing: a new life," *International journal of clothing science and technology*, vol. 16, no. 1/2, pp. 63–72, 2004.

[25] D. Hartl and D. Lagoudas, "Aerospace applications of shape memory alloys," *Proceedings of the Insitiution of Mechanical Engineers, Part G*, vol. 221, pp. 535–552, 2007.

[26] J. Kudva, "Overview of the darpa smart wing project," *Journal of Intelligent Material Systems and Structures*, vol. 15, pp. 261–267, 2004.

[27] J. Kudva, K. Appa, M. C., A. Jardine, G. Sendeckyj, T. Harris, A. McGowan, and R. Lake, "Design, fabrication, and testing of the darpa/wright lab 'smart wing' wind tunnel model," *in proceedings: 38th AIAA Structures, Structural Dynamics and Materials Conference. Kissimmee, FL*, 1997.

[28] A. Jardine, J. Kudva, C. Martin, and K. Appa, "Shape memory alloy tini actuators for twist control of smart wing designs," *in proceedings: SPIE Smart Structures and Materials: Smart Structures and integrated systems*, vol. 2717, 1996.

[29] A. Jardine, J. Flanagan, K. Appa, and J. Kudva, "Smart wing shape memory alloy actuator design and performance," *in proceedings: SPIE Smart Structures and Materials: Industrial and Commerical Applications of Smart Structures Technologies*, vol. 3044, 1997.

[30] D. Pitt, J. Dunne, E. White, and E. Garcia, "Sampson smart inlet sma powered adaptive lip design and static test," *in proceedings: 19th AIAA Applied Aerodynamics Conference, Anaheim, CA*, 2001.

[31] J. Mabe, R. Cabell, and G. Butler, "Design and control of a morphing chevron for takeoff and cruise noise reduction," *in proceedings: 26th AIAA Aeroacoustics Conference, Monterey, CA, U.S.A*, 2005.

[32] J. Mabe, F. Calkins, and G. Butler, "Boeing's variable geometry cehvron, morphing aerostructure for jet noise reduction," *in proceedings: 47thAIAA/ASME/ASCE/AHS/ASC Structures, Structural Dynamics, and Materials Conference, Newport, Rhode Island*, 2006.

[33] D. Hartl, B. Volk, D. Lagoudas, F. Calkins, and J. Mabe, "Thermomechanical characterization and modeling of ni60ti40 sma for actuated chevrons," *in proceedings: ASME 2006*

International Mechanical Engineering Congress and Exposition, Chicago, IL, pp. 281–290, 2006.

[34] D. J. Hartl and D. C. Lagoudas, "Characterization and 3-d modeling of ni60ti sma for actuation of a variable geometry jet engine chevron," in *Sensors and Smart Structures Technologies for Civil, Mechanical, and Aerospace Systems 2007*, vol. 6529, p. 65293Z, International Society for Optics and Photonics, 2007.

[35] T. Turner, R. Buehrle, R. Cano, and G. Fleming, "Modeling, fabrication, and testing of a sma hybrid composite jet enginer chevron concept," *Journal of Intelligent Matreial Systems and Structures*, vol. 17, pp. 483–497, 2006.

[36] N. Caldwell, E. Gutmark, and R. Ruggeri, "Heat transfer model for blade twist actuator system," *Journal of thermophysics and heat transfer*, vol. 21, no. 2, pp. 352–360, 2007.

[37] H. Prahlad and I. Chopra, "Design of a variable twist tilt-rotor blade using shape memory alloy (sma) actuators," in *Smart Structures and Materials 2001: Smart Structures and Integrated Systems*, vol. 4327, pp. 46–60, International Society for Optics and Photonics, 2001.

[38] K. Madangopal, "The self accommodating martensitic microstructure of niti shape memory alloys," *Acta materialia*, vol. 45, no. 12, pp. 5347–5365, 1997.

[39] S. Miyazaki, K. Otsuka, H. Sakamoto, and K. Shimizu, "The fracture of cu-al-ni shape memory alloy," *Transactions of the Japan Institute of Metals*, vol. 22, pp. 244–252, 1981.

[40] Y. Xu, R. Wang, and Z. Wang, "In-situ investigation of stress-induced martensitic transformation in the ti-ni shape memory alloy during deformation," *Materials Letters*, vol. 24, pp. 355–358, 1995.

[41] H. Yin, Y. He, Z. Moumni, and Q. Sun, "Effects of grain size on tensile fatigue life of nanostructured niti shape memory alloy," *IJF*, vol. 88, pp. 166–177, 2016.

[42] K. Gall and H. Maier, "Cyclic deformation mechanisms in precipitated niti shape memory alloys," *Acta Materialia*, vol. 50, pp. 4643–4657, 2002.

[43] J. Khalil-Allafi, A. Dlouhy, and G. Eggeler, "Ni4ti3-precipitation during aging of niti shape

memory alloys and its influence on martensitic phase transformations," *Acta Materialia*, vol. 50, pp. 4255–4274, 2002.

[44] T. Baxevanis, A. Cox, and D. Lagoudas, "Micromechanics of precipitated near-equiatomic ni-rich niti shape memory alloys," *Acta Mechanica*, vol. 225, pp. 1167–1185, 2014.

[45] S. Gollerthan, M. Young, A. Baruj, J. Frenzel, W. Schmahl, and G. Eggeler, "Fracture mechanics and microstructure in niti shape memory alloys," *Acta Materialia*, vol. 57, pp. 1015–1025, 2009.

[46] T. Baxevanis and D. Lagoudas, "Fracture mechanics of shape memory alloys: review and perspectives," *International Journal of Fracture*, vol. 191, pp. 191–213, 2015.

[47] S. Jape, T. Baxevanis, and D. Lagoudas, "Stable crack growth during thermal actuation of shape memory alloys," *Shape Memory and Superelasticity*, vol. 2, pp. 104–113, 2016.

[48] G. Mirone, "Role of stress triaxiality in elastoplastic characterization and ductile failure prediction," *Engineering Fracture Mechanics*, vol. 74, pp. 1203–1221, 2007.

[49] A. Benzerga, J. Besson, and A. Pineau, "Anisotropic ductile fracture: Part i: Experiments," *Acta Materialia*, vol. 52, pp. 4623–4638, 2004.

[50] B. Kondori and A. Benzerga, "Effect of stress triaxiality on the flow and fracture of mg alloy az31," *Metallurgical and Materials Transactions A*, vol. 45, pp. 3292–3307, 2014.

[51] J. Olsen, Z. Zhang, H. Lu, and C. van der Eijk, "Fracture of notched round-bar niti-specimens," *Engineering Fracture Mechanics*, vol. 84, pp. 1–14, 2012.

[52] Y. Bao and T. Wierzbicki, "On fracture locus in the equivalent strain and stress triaxiality space," *International Journal of Mechancial Sciences*, vol. 46, pp. 81–98, 2004.

[53] P. Bridgman, ed., *Studies in Large Plastic Flow and Fracture*. Harvard University Press, 1964.

[54] G. A. Webster, P. F. Aplin, B. J. Cane, B. F. Dyson, and M. S. Loveday, *A Code of Practice for Notched Bar Creep Rupture Testing: Procedures and Interpretation of Data for Design*, pp. 295–330. Dordrecht: Springer Netherlands, 1992.

[55] R. Becker, A. Needleman, O. Richmond, and V. Tvergaard, "Void growth and failure in

notched bars," *Journal of the Mechanics and Physics of Solids*, vol. 36, no. 3, pp. 317–351, 1988.

[56] Y. Chang, H. Xu, Y. Ni, X. Lan, and H. Li, "Research on representative stress and fracture ductility of p92 steel under multiaxial creep," *Engineering Failure Analysis*, vol. 59, pp. 140–150, 2016.

[57] R. Skelton, S. Wee, and G. Webster, "Cyclic stress–strain behaviour of circumferentially notched cylindrical bars at high temperature," *Materials at High Temperatures*, vol. 18, no. 3, pp. 139–152, 2001.

[58] G. Eggeler, H. E., Y. A., A. Heckmann, and M. Wagner, "Structural and functional fatigue of niti shape memory alloys," *Materials Science and Engineering: A*, vol. 378, pp. 24–33, 2004.

[59] T. Ataalla, M. Leary, and A. Subic, "Functional fatigue of shape memory alloys," in *Sustainable Automotive Technologies 2012*, pp. 39–43, Springer, 2012.

[60] K. Melton and O. Mercier, "Fatigue of niti thermoelastic martensites," *Acta Metallurgice*, vol. 27, pp. 137–144, 1979.

[61] B. O. Agboola, D. J. Hartl, and D. C. Lagoudas, "A study of actuation fatigue of shape memory alloy," in *ASME 2012 Conference on Smart Materials, Adaptive Structures and Intelligent Systems*, pp. 287–293, American Society of Mechanical Engineers, 2012.

[62] C. Calhoun, "Effect of ni3ti precipitates on actuation fatigue of ni60ti40 (wt.%) shape memory alloys," *Master of Science thesis, Texas A&M University*, 2011.

[63] A. Pelton, "Nitinol fatigue: a review of microstructures and mechanisms," *Journal of Materials Engineering and Performance*, vol. 20, no. 4-5, pp. 613–617, 2011.

[64] R. Wheeler, J. Santa-Cruz, D. Hartl, and D. Lagoudas, "Effect of processing and loading on equiatomic niti fatigue life and localized failure mechanisms," in *ASME 2013 Conference on Smart Materials, Adaptive Structures and Intelligent Systems*, pp. V002T02A010–V002T02A010, American Society of Mechanical Engineers, 2013.

[65] D. A. Miller, *Thermomechanical characterization of plastic deformation and transformation*

fatigue in shape memory alloys. PhD thesis, Texas A & M University, 2000.

[66] R. W. Wheeler, D. J. Hartl, Y. Chemisky, and D. C. Lagoudas, "Characterization and modeling of thermo-mechanical fatigue in equiatomic niti actuators," in *ASME 2014 Conference on Smart Materials, Adaptive Structures and Intelligent Systems*, pp. V002T02A009–V002T02A009, American Society of Mechanical Engineers, 2014.

[67] C. Calhoun, R. Wheeler, T. Baxevanis, and D. Lagoudas, "Actuation fatigue life prediction of shape memory alloys under the constant-stress loading condition," *Scripta Materialia*, vol. 95, pp. 58–61, 2015.

[68] G. Scire Mammano and E. Dragoni, "Functional fatigue of ni-ti shape memory wires under various loading conditions," *International Journal of Fatigue*, vol. 69, pp. 71–83, 2014.

[69] R. W. Wheeler, D. J. Hartl, Y. Chemisky, and D. C. Lagoudas, "Modeling of thermo-mechanical fatigue and damage in shape memory alloy axial actuators," in *Behavior and Mechanics of Multifunctional Materials and Composites 2015*, vol. 9432, p. 94320K, International Society for Optics and Photonics, 2015.

[70] H. Tobushi, T. Hachisuka, T. Hashimoto, and S. Yamada, "Cyclic deformation and fatigue of a tini shape-memory alloy wire subjected to rotating bending," *Journal of engineering materials and technology*, vol. 120, no. 1, pp. 64–70, 1998.

[71] J. M. Young and K. J. Van Vliet, "Predicting in vivo failure of pseudoelastic niti devices under low cycle, high amplitude fatigue," *Journal of Biomedical Materials Research Part B: Applied Biomaterials*, vol. 72, no. 1, pp. 17–26, 2005.

[72] S. Miyazaki, K. Mizukoshi, T. Ueki, T. Sakuma, and Y. Liu, "Fatigue life of ti–50 at.% ni and ti–40ni–10cu (at.%) shape memory alloy wires," *Materials Science and Engineering: A*, vol. 273, pp. 658–663, 1999.

[73] O. W. Bertacchini, D. C. Lagoudas, and E. Patoor, "Fatigue life characterization of shape memory alloys undergoing thermomechanical cyclic loading," in *Smart Structures and Materials 2003: Active Materials: Behavior and Mechanics*, vol. 5053, pp. 612–625, International Society for Optics and Photonics, 2003.

[74] M. Bigeon and M. Morin, "Thermomechanical study of the stress assisted two way memory effect fatigue in tini and cuznal wires," *Scripta Materialia*, vol. 35, pp. 1373–1378, 1996.

[75] S. Bhaumik, C. Saikrishna, K. Ramaiah, and M. Venkataswamy, "Understanding the fatigue behaviour of niticu shape memory alloy wire thermal actuators," in *Key Engineering Materials*, vol. 378, pp. 301–316, Trans Tech Publ, 2008.

[76] P. Pappas, D. Bollas, J. Parthenios, V. Dracopoulos, and C. Galiotis, "Transformation fatigue and stress relaxation of shape memory alloy wires," *Smart Materials and Structures*, vol. 16, no. 6, p. 2560, 2007.

[77] C. Maletta, E. Sgambitterra, F. Furgiuele, R. Casati, and A. Tuissi, "Fatigue of pseudoelastic niti within the stress-induced transformation regime: a modified coffin–manson approach," *Smart materials and structures*, vol. 21, no. 11, p. 112001, 2012.

[78] M. Karhu and T. Lindroos, "Microstructure analysis and damage patterns of thermally cycled ti–49.7 ni (at.%) wires," *Smart Materials and Structures*, vol. 21, no. 3, p. 035008, 2012.

[79] O. W. Bertacchini, *Characterization and modeling of transformation induced fatigue of shape memory alloy actuators*. PhD thesis, Texas A & M University, 2011.

[80] Z. Bo and D. C. Lagoudas, "Thermomechanical modeling of polycrystalline smas under cyclic loading, part iii: evolution of plastic strains and two-way shape memory effect," *International Journal of Engineering Science*, vol. 37, no. 9, pp. 1175–1203, 1999.

[81] L. J. Rong, D. A. Miller, D. C. Lagoudas, *et al.*, "Thermo-mechanical fatigue and transformation behavior of tinicusma," in *Materials Science Forum*, vol. 394, pp. 329–332, Trans Tech Publications Ltd., Zurich-Uetikon, Switzerland, 2001.

[82] D. Lagoudas, D. Miller, L. Rong, and P. Kumar, "Thermomechanical fatigue of shape memory alloys," *Smart Materials and Structures*, vol. 18, no. 8, p. 085021, 2009.

[83] D. C. Lagoudas, O. W. Bertacchini, and E. Patoor, "Surface crack development in transformation induced fatigue of sma actuators," in *Residual Stress and Its Effects on Fatigue and Fracture*, pp. 209–222, Springer, 2006.

[84] J. R. Schick, "Transformation induced fatigue of ni-rich niti shape memory alloy actuators," *Master of Science thesis, Texas A&M University*, 2011.

[85] A. McKelvey and R. Ritchie, "Fatigue-crack growth behavior in the superelastic and shape-memory alloy nitinol," *Metallurgical and Materials Transactions A*, vol. 32, pp. 731–743, 2001.

[86] A. R. Pelton, X.-Y. Gong, and T. Duerig, "Fatigue testing of diamond-shaped specimens," *Medical Device Materials*, pp. 199–204, 2004.

[87] R. Wheeler, *Actuation Fatigue Characterization Methods and Lifetime Predictions of Shape Memory Alloy Actuators*. PhD thesis, Texas AM University, 2017.

[88] O. Bertacchini, D. Lagoudas, and E. Patoor, "Thermomechanical transformation fatigue of tinicu sma actuators under a corrosive environment - part i: Experimental results," *International Journal of Fatigue*, vol. 31, pp. 1571–1578, 2009.

[89] N. Nayan, D. Roy, V. Buravalla, and U. Ramamurty, "Unnotched fatigue behavior of an austenitic ni-ti shape memory alloy," *Materials Science and Engineering: A*, vol. 497, pp. 333–340, 2008.

[90] R. Wheeler, J. Santa-Cruz, D. Hartl, and D. Lagoudas, "Effect of processing and loading on equiatomic niti fatigue life and localized failure mechanisms," in *Mechanics and Behavior of Active Materials, Conference on Smart Materials, Adaptive Structures and Intelligent Systems*, American Society of Mechanical Engineers, 2013.

[91] D. C. Lagoudas and P. B. Entchev, "Modeling of transformation-induced plasticity and its effect on the behavior of porous shape memory alloys. part i: constitutive model for fully dense smas," *Mechanics of Materials*, vol. 36, no. 9, pp. 865–892, 2004.

[92] C. Calhoun, *Actuation Fatigue in Shape Memory Alloys*. PhD thesis, Texas AM University, 2012.

[93] K. Smith, P. Watson, and T. Topper, "A stress-strain function for the fatigue of metals," *J. Mater.*, vol. 5, no. 4, pp. 767–778, 1970.

[94] Y. Chemisky, D. J. Hartl, and F. Meraghni, "Three-dimensional constitutive model for struc-

tural and functional fatigue of shape memory alloy actuators," *International Journal of Fatigue*, vol. 112, pp. 263–278, 2018.

[95] D. Lagoudas, D. Hartl, Y. Chemisky, L. Machado, and P. Popov, "Constitutive model for the numerical analysis of phase transformation in polycrystalline shape memory alloys," *International Journal of Plasticity*, vol. 32-33, pp. 155–183, 2012.

[96] K. An, "Vdrive-data reduction and interactive visualization software for event mode neutron diffraction," *ORNL Report No. ORNL-TM-2012-621, Oak Ridge National Laboratory, Oak Ridge, TN*, 2012.

[97] K. An, H. D. Skorpenske, A. D. Stoica, D. Ma, X.-L. Wang, and E. Cakmak, "First in situ lattice strains measurements under load at vulcan," *Metallurgical and Materials Transactions A*, vol. 42, no. 1, pp. 95–99, 2011.

[98] O. Benafan, R. Noebe, S. A. Padula II, D. Gaydosh, B. Lerch, A. Garg, G. Bigelow, K. An, and R. Vaidyanathan, "Temperature-dependent behavior of a polycrystalline niti shape memory alloy around the transformation regime," *Scripta Materialia*, vol. 68, no. 8, pp. 571–574, 2013.

[99] O. Benafan, S. Padula, H. Skorpenske, K. An, and R. Vaidyanathan, "Design and implementation of a multiaxial loading capability during heating on an engineering neutron diffractometer," *Review of Scientific Instruments*, vol. 85, no. 10, p. 103901, 2014.

[100] O. Benafan, A. Garg, R. Noebe, H. Skorpenske, K. An, and N. Schell, "Deformation characteristics of the intermetallic alloy 60niti," *Intermetallics*, vol. 82, pp. 40–52, 2017.

[101] D. E. Nicholson, M. A. Bass, J. H. Mabe, O. Benafan, S. A. Padula, and R. Vaidyanathan, "Heating and loading paths to optimize the performance of trained shape memory alloy torsional actuators," in *ASME 2016 Conference on Smart Materials, Adaptive Structures and Intelligent Systems*, pp. V001T02A008–V001T02A008, American Society of Mechanical Engineers, 2016.

[102] O. Benafan, *Deformation and Phase Transformation Processes in Polycrystalline NiTi and NiTiHf High Temperature Shape Memory Alloys*. PhD thesis, University of Central Florida,

2012.

[103] "Dragonfly." Objects Research Systems (ORS) Inc, 2016. http://www.theobjects.com/dragonfly.

[104] B. Agboola, D. Hartl, and D. Lagoudas, "A study of actuation fatigue of shape memory alloys," in *ASME 2012 Conference on Smart Materials, Adaptive Structures, and Intelligent Systems*, American Society of Mechanical Engineers, 2012.

[105] F. R. Phillips and D. C. Lagoudas, "Effect of stress redistribution during thermal actuation of shape memory alloys in notched cylindrical bars," *Journal of Intelligent Material Systems and Structures*, 2018, in press.

[106] M. Miner *et al.*, "Cumulative fatigue damage," *Journal of applied mechanics*, vol. 12, no. 3, pp. A159–A164, 1945.

[107] W. Callister, *Materials Science And Engineering: An Introduction*. John Wiley & Sons, 2007.

[108] C. Dunand-Châtellet and Z. Moumni, "Experimental analysis of the fatigue of shape memory alloys through power-law statistics," *International journal of fatigue*, vol. 36, no. 1, pp. 163–170, 2012.

[109] L. Coffin, "The cyclic straining and fatigue of metals," *Trans Metall Soc AIME*, vol. 215, p. 794, 1959.

[110] L. Xue, "A unified expression for low cycle fatigue and extremely low cycle fatigue and its implication for monotonic loading," *International Journal of Fatigue*, vol. 30, no. 10-11, pp. 1691–1698, 2008.

[111] F. R. Shanley, "A proposed mechanism of fatigue failure," in *Colloquium on Fatigue/Colloque de Fatigue/Kolloquium über Ermüdungsfestigkeit*, pp. 251–259, Springer, 1956.

[112] A. Seweryn, A. Buczyński, and J. Szusta, "Damage accumulation model for low cycle fatigue," *International Journal of fatigue*, vol. 30, no. 4, pp. 756–765, 2008.

[113] C. Hayrettin, S. Jape, T. Baxevanis, I. Karaman, S. Ozguc, and D. Lagoudas, "Experimental evidence on stable crack growth in shape memory alloys during thermal cycles under stress,"

in preparation.

[114] A. Paglietti, "The mathematical formulation of the local form of the second principle of thermodynamics," in *Institut Henri Poincare, Annales*, vol. 27, pp. 207–219, 1977.

[115] B. D. Coleman and W. Noll, "The thermodynamics of elastic materials with heat conduction and viscosity," *Archive for rational mechanics and analysis*, vol. 13, no. 1, pp. 167–178, 1963.

[116] M. Qidwai and D. Lagoudas, "On thermomechanics and transformation surfaces of poly-crystalline niti shape memory alloy material," *International journal of plasticity*, vol. 16, no. 10-11, pp. 1309–1343, 2000.

[117] R. Wheeler, C. Ottmers, B. Hewling, and D. Lagoudas, "Actuator lifetime predictions for ni60ti40 shape memory alloy plate actuators," *in proceedings: SPIE Smart Structure and Materials + Nondestructive Evluation and Health Monitoring*, p. 98000E, 2016.

APPENDIX A

X-RAY COMPUTED MICROTOMOGRAPHY SEGMENTATION SCRIPT

The following Matlab script was utilized to analyze the stack of .tif images output from the x-ray computed microtomography scans. The general flow is as follows:

- First general input information is given to the program. This general information is required in order to determine where the images are located, what file to save the results into, and some numerical values in order to aid in the segmentation procedure.

- The entire stack of images is then pulled into the program and various variables are initialized.

- The number of images under consideration for each loop is then trimmed to only those images around the current image of interest.

- An averaged image of all the images close to the current image is generated. This averaged image is used for comparison to the current image of interest in the segmentation procedure.

- The boundary of the specimen in the image is established.

- The current image of interest is compared to the averaged image, and pixels in the current image above a certain threshold of difference to the averaged image are considered as defects.

- These defective sites in the current image of interest are compared to the previous and next image in order to minimize false positives.

- The various images generated during the image processing are saved and the data is printed out and saved for future processing.

Matlab Code

```matlab
1  clear;clc
2
3  %%%%%%%%%%%%%%%%%%%%%%%%%%%%%%%%%%%%%%%%%%%%%%%%%%%%%%%%%%%%%%%%%%%%%
4  %Parameters for thresholding and saving
5  boundary_edge_exclusion=15;
6  folderpath='E:\Research\fatigue\xray\500_11_25percentTifs\threshold\';
7  threshold_value=28;
8  min_pixel_value=125;
9  Gx_strength=20;
10 Gy_strength=20;
11 ROI_check=0;
12 image_initial_exclude=15;
13 image_final_exclude=15;
14 defect_info_file='25per_defect_v7.txt';
15 start_image=75;
16 end_image=1000;
17 num_image_for_avg=30;
18
19 %%%%%%%%%%%%%%%%%%%%%%%%%%%%%%%%%%%%%%%%%%%%%%%%%%%%%%%%%%%%%%%%%%%%%%%
20 %Initial Image pull
21 images=image_pull(start_image,start_image);
22
23 [r,c]=size(images);
24 tot_num_image=end_image-start_image;
25 %%%%%%%%%%%%%%%%%%%%%%%%%%%%%%%%%%%%%%%%%%%%%%%%%%%%%%%%%%%%%%%%%%%%%%
26 %Initialize interior point sum and defect point sum for final comparison
27 interior_points_image(1:tot_num_image)=0;
28 defect_points_image(1:tot_num_image)=0;
29 image_thresh_enlarge(1:r,1:c)=0;
```

```matlab
30  interior_points_image2(1:tot_num_image)=0;

31  defect_points_image2(1:tot_num_image)=0;

32  defect_points_multilayer(1:tot_num_image)=0;

33

34  fprintf('%7s %9s %10s %9s %10s %17s \n','Image','Defects','Interior','...
        Defects2','Interior2','Defects_multi');

35

36  %%%%%%%%%%%%%%%%%%%%%%%%%%%%%%%%%%%%%%%%%%%%%%%%%%%%%%%%%%%%%%%%%%%%%%%%%

37  %Processing Loop

38

39  loop_counter=0;

40  for image_num=image_initial_exclude:(tot_num_image-image_final_exclude)

41      loop_counter=loop_counter+1;

42

43      clearvars -except images image tot_num_image loop_counter len width...
            folderpath boundary_edge_exclusion threshold_value ...
                image_thresh_enlarge...

45          min_pixel_value Gx_strength Gy_strength ROI_check r c top_r left_c...
                ...

46          image_initial_exclude defect_info_file image_num prev_spec_boundary...
                ...

47          image_final_exclude interior_points_image defect_points_image ...

48          prev_spec_interior2 interior_points_image2 defect_points_image2 ...

49          defects_cur defects_prev defect_points_multilayer start_image ...
                end_image ...

50          num_image_for_avg init_boundary init_boundary2 init_specimen ...
                init_specimen2

51

52      if loop_counter==1

53          image=image_pull(start_image+image_initial_exclude,start_image+...
                image_initial_exclude+num_image_for_avg);

54      elseif loop_counter==2

55          image_copy=image;
```

```
56          clear image image_thresh_enlarge
57
58          top_r_found=0;
59          bot_r_found=0;
60          left_c_found=0;
61          right_c_found=0;
62          for i=1:r
63              for j=1:c
64                  if init_boundary(i,j)==1
65                      top_r=i;
66                      top_r_found=1;
67                      break
68                  end
69              end
70              if top_r_found==1;
71                  break
72              end
73          end
74          for i=1:r
75              for j=1:c
76                  if init_boundary(r-i,j)==1
77                      bot_r=r-i;
78                      bot_r_found=1;
79                      break
80                  end
81              end
82              if bot_r_found==1
83                  break
84              end
85          end
86
87          for i=1:c
88              for j=1:r
```

```matlab
89              if init_boundary(j,i)==1
90                  left_c=i;
91                  left_c_found=1;
92                  break
93              end
94          end
95          if left_c_found==1
96              break
97          end
98      end

100     for i=1:c
101         for j=1:r
102             if init_boundary(j,c-i)==1
103                 right_c=c-i;
104                 right_c_found=1;
105                 break
106             end
107         end
108         if right_c_found==1
109             break
110         end
111     end


114     len=bot_r-top_r+101;
115     width=right_c-left_c+101;

117     for k=1:num_image_for_avg
118         for i=1:len
119             for j=1:width
120                 image(i,j,k)=image_copy(top_r-50+i,left_c-50+j,k+1);
121             end
```

```matlab
122                 end
123             end
124
125         new_image=image_pull(start_image+image_num+num_image_for_avg+1,...
                    start_image+image_num+num_image_for_avg+1);
126         for i=1:len
127             for j=1:width
128                 image(i,j,num_image_for_avg+1)=new_image(top_r-50+i,left_c...
                        -50+j);
129             end
130         end
131     else
132         for i=1:num_image_for_avg
133             image(:,:,i)=image(:,:,i+1);
134         end
135
136         new_image=image_pull(start_image+image_num+num_image_for_avg+1,...
                    start_image+image_num+num_image_for_avg+1);
137         for i=1:len
138             for j=1:width
139                 image(i,j,num_image_for_avg+1)=new_image(top_r-25+i,left_c...
                        -25+j);
140             end
141         end
142     end
143
144     [r,c,num_image]=size(image);
145     image_double=double(image(:,:,(num_image+1)/2));
146
147     if loop_counter==2
148         image_thresh_enlarge(1:r,1:c,1:tot_num_image)=0;
149     end
150 %Average image generation
```

144

```matlab
151     avg_image(1:r,1:c)=0;
152     for i=1:r
153         for j=1:c
154             avg_image(i,j)=median(image(i,j,:));
155         end
156     end
157
158     avg_image_uint8=uint8(avg_image);
159
160 %Determine if pixel location within specimen
161     [Gx_image,Gy_image]=imgradientxy(image_double);
162     specimen_boundary(1:r,1:c)=0;
163
164     for i=1:r
165         for j=1:c
166             if sqrt((i-r/2)^2+(j-c/2)^2)<(round(r/2)-5)
167                 if image_double(i,j)>min_pixel_value
168                     if Gx_image(i,j)>Gx_strength
169                         specimen_boundary(i,j)=1;
170                     elseif Gx_image(i,j)<((-1)*Gx_strength)
171                         specimen_boundary(i,j)=1;
172                     elseif Gy_image(i,j)>Gy_strength
173                         specimen_boundary(i,j)=1;
174                     elseif Gy_image(i,j)<((-1)*Gy_strength)
175                         specimen_boundary(i,j)=1;
176                     end
177                 end
178             end
179         end
180     end
181
182     specimen_boundary2(1:r,1:c)=0;
183     for i=1:c
```

```matlab
        for j=1:r
            if specimen_boundary(j,i)==1
                specimen_boundary2(j:(j+2),i)=1;
                break
            end
        end
        for j=1:r-1
            if specimen_boundary(r-j,i)==1
                specimen_boundary2((r-j-2):(r-j),i)=1;
                break
            end
        end
    end

    for i=1:r
        for j=1:c
            if specimen_boundary(i,j)==1
                specimen_boundary2(i,j:(j+2))=1;
                break
            end
        end
        for j=1:c-1
            if specimen_boundary(i,c-j)==1
                specimen_boundary2(i,(c-j-2):(c-j))=1;
                break
            end
        end
    end


    col_start_found=0;
    for i=1:c
        for j=1:r
```

```matlab
217             if specimen_boundary2(j,i)==1
218                 col_start=i;
219                 col_start_found=1;
220                 break
221             end
222         end
223         if col_start_found==1
224             break
225         end
226     end
227
228     col_end_found=0;
229     for i=1:c
230         for j=1:r
231             if specimen_boundary2(j,max(c-i,1))==1
232                 col_end=c-i;
233                 col_end_found=1;
234                 break
235             end
236         end
237         if col_end_found==1
238             break
239         end
240     end
241
242     row_start(1:c)=0;
243     row_end(1:c)=0;
244
245     for i=col_start:col_end
246         for j=1:r
247             if specimen_boundary2(j,i)==1
248                 row_start(i)=j;
249                 break
```

```matlab
                end
            end
        end

    for i=col_start:col_end
        for j=1:r
            if specimen_boundary2(max(1,(r-j)),i)==1
                row_end(i)=r-j;
                break
            end
        end
    end

    %Determine pixels inside specimen
    specimen_interior(1:r,1:c)=0;
    for i=col_start:col_end
        if row_start(i)>0
            if row_end(i)>0
                for j=row_start(i):row_end(i)
                    specimen_interior(j,i)=1;
                end
            else
                break
            end
        else
            break
        end
    end

    specimen_interior2(1:r,1:c)=0;
    for i=col_start:col_end
        if row_start(i)>0
            if row_end(i)>0
```

```matlab
                for j=row_start(i):row_end(i)
                    specimen_interior2(j,i)=1;
                    for k=1:boundary_edge_exclusion
                        if specimen_boundary2(min(r,(j+k)),i)==1
                            specimen_interior2(j,i)=0;
                            break
                        elseif specimen_boundary2(max(1,(j-k)),i)==1
                            specimen_interior2(j,i)=0;
                            break
                        elseif specimen_boundary2(j,min(c,(i+k)))==1
                            specimen_interior2(j,i)=0;
                            break
                        elseif specimen_boundary2(j,max(1,(i-k)))==1
                            specimen_interior2(j,i)=0;
                            break
                        end
                    end
                end
            else
                break
            end
        else
            break
        end
    end

    specimen_interior_255=specimen_interior.*255;
    specimen_interior2_255=specimen_interior2.*255;

    if ROI_check==1
        figure;imshowpair(avg_image,specimen_boundary,'montage');
        figure;imshowpair(avg_image,specimen_boundary2,'montage');
        figure;imshowpair(avg_image,specimen_interior,'montage');
```

149

```
316          figure;imshowpair(avg_image,specimen_interior2,'montage');
317          break
318      end
319
320      if loop_counter==1
321          init_boundary=specimen_boundary;
322          init_boundary2=specimen_boundary2;
323          init_interior=specimen_interior;
324          init_interior2=specimen_interior2;
325      end
326
327  %Highlighting of differences to average
328      image_sub(1:r,1:c)=0;
329      for i=1:r
330          for j=1:c
331              if specimen_interior(i,j)==0
332                  image_sub(i,j)=0;
333              else
334                  image_sub(i,j)=abs(image_double(i,j)-avg_image(i,j));
335              end
336          end
337      end
338
339  %Normalize images
340      image_max=max(max(image_sub(:,:)));
341      norm_factor=255/image_max;
342      image_norm(:,:)=image_sub(:,:).*norm_factor;
343
344  %Threshold Images
345      image_thresh(1:r,1:c)=255;
346
347      for i=2:r-1
348          for j=2:c-1
```

```matlab
                for s=-1:1
                        for t=-1:1
                                if image_norm(i+s,j+t)<threshold_value
                                        image_thresh(i,j)=0;
                                        break
                                end
                        end
                end
        end
    end

%Increase threshold spot size to account for size criterion
    image_thresh_enlarge2(1:r,1:c)=0;

    for i=1:r
        for j=1:c
            if specimen_interior(i,j)==1
                if image_thresh(i,j)>0.5
                    if image(i,j)>min_pixel_value
                        for s=-2:2
                            for t=-2:2
                                image_thresh_enlarge(i+s,j+t,image_num)=1;
                            end
                        end
                    end
                end
            end
            if specimen_interior2(i,j)==1
                if image_thresh(i,j)>0.5
                    if image(i,j)>min_pixel_value
                        for s=-2:2
                            for t=-2:2
                                image_thresh_enlarge2(i+s,j+t)=1;
```

151

```matlab
                              end
                          end
                      end
                  end
              end
          end

    %check if defect on previous images
    if (image_num-image_initial_exclude)>1
        defects_prev2=defects_prev;
        defects_prev=defects_cur;
        defects_cur=image_thresh_enlarge2;

        for i=1:r
            for j=1:c
                if defects_prev(i,j)==1
                    real_defect=0;
                    for m=1:3
                        for n=1:3
                            if defects_cur(i+m,j+n)==1
                                real_defect=1;
                                break
                            elseif defects_cur(i+m,j-n)==1
                                real_defect=1;
                                break
                            elseif defects_cur(i-m,j+n)==1
                                real_defect=1;
                                break
                            elseif defects_cur(i-m,j-n)==1
                                real_defect=1;
                                break
                            elseif defects_prev2(i+m,j+n)==1
```

```matlab
                                 real_defect=1;
                                     break
                                 elseif defects_prev2(i+m,j-n)==1
                                     real_defect=1;
                                     break
                                 elseif defects_prev2(i-m,j+n)==1
                                     real_defect=1;
                                     break
                                 elseif defects_prev2(i-m,j-n)==1
                                     real_defect=1;
                                     break
                                 end
                             end
                             if real_defect==1
                                 break
                             end
                         end
                         if real_defect==0
                             defects_prev(i,j)=0;
                         end
                     end
                 end
        end
    elseif (image_num-image_initial_exclude)==1
        defects_prev=defects_cur;
        defects_cur=image_thresh_enlarge2;
    else
        defects_cur=image_thresh_enlarge2;
    end

    image_thresh_enlarge_125=image_thresh_enlarge(:,:,image_num).*125;
    image_thresh_enlarge2_125=image_thresh_enlarge2(:,:).*125;
```

```matlab
448        specimen_out=uint8(specimen_interior_255-image_thresh_enlarge_125);

449        specimen_out2=uint8(specimen_interior2_255-image_thresh_enlarge2_125);

450

451        %Save images

452        if image_num<10

453            image_num_str=strcat('00',num2str(image_num));

454        elseif image_num<100

455            image_num_str=strcat('0',num2str(image_num));

456        else

457            image_num_str=num2str(image_num);

458        end

459

460        if image_num<10

461            image_num_str_min1=strcat('00',num2str(image_num-1));

462        elseif image_num<101

463            image_num_str_min1=strcat('0',num2str(image_num-1));

464        else

465            image_num_str_min1=num2str(image_num-1);

466        end

467

468        bound_defect=max(specimen_boundary2,image_thresh_enlarge2);

469

470        %Save threshold image

471        filename=strcat('threshold_',image_num_str,'.tif');

472        pathname=[folderpath filename];

473        imwrite(image_thresh_enlarge(:,:,image_num),pathname);

474

475        %Save specimen boundary image

476        filename2=strcat('boundary_',image_num_str,'.tif');

477        pathname=[folderpath filename2];

478        imwrite(specimen_boundary,pathname);

479

480        %Save specimen boundary image
```

```matlab
481     filename2=strcat('boundary2_',image_num_str,'.tif');

482     pathname=[folderpath filename2];

483     imwrite(specimen_boundary2,pathname);

484

485     %Save specimen

486     filename=strcat('specimen_',image_num_str,'.tif');

487     pathname=[folderpath filename];

488     imwrite(specimen_out,pathname);

489

490     %Save specimen2

491     filename=strcat('specimen2_',image_num_str,'.tif');

492     pathname=[folderpath filename];

493     imwrite(specimen_out2,pathname);

494

495     %Save specimen boundary and defects

496     filename=strcat('boundary_defect_',image_num_str,'.tif');

497     pathname=[folderpath filename];

498     imwrite(bound_defect,pathname);

499

500     %Save threshold2 image

501     filename=strcat('threshold2_',image_num_str,'.tif');

502     pathname=[folderpath filename];

503     imwrite(image_thresh_enlarge2,pathname);

504

505     %Save multilayer threshold image

506     if (image_num-image_initial_exclude)>1

507         filename=strcat('threshold2_multilayer_',image_num_str_min1,'.tif')...
            ;

508         pathname=[folderpath filename];

509         imwrite(defects_prev,pathname);

510     end

511

512 %Add total interior points and total defect points
```

```matlab
513     interior_points_image(image_num)=sum(sum(specimen_interior));
514     defect_points_image(image_num)=sum(sum(image_thresh_enlarge(:,:,...
            image_num)));
515
516     interior_points_image2(image_num)=sum(sum(specimen_interior2));
517     defect_points_image2(image_num)=sum(sum(image_thresh_enlarge2));
518
519     if (image_num-image_initial_exclude)>1
520         defect_points_multilayer(image_num)=sum(sum(defects_prev));
521     else
522         defect_points_multilayer(image_num)=sum(sum(image_thresh_enlarge2))...
            ;
523     end
524
525     fprintf('%7i %9i %10i %9i %10i %17i \n',image_num,defect_points_image(...
            image_num),interior_points_image(image_num),defect_points_image2(...
            image_num),interior_points_image2(image_num),...
            defect_points_multilayer(image_num));
526 end
527
528 %Save stats to file
529 fileID=fopen(defect_info_file,'w');
530 fprintf(fileID,'%7s %9s %10s %20s %9s %10s %20s %9s %20s \r\n','Image','...
        Defects','Interior','Defect Percentage','Defects_2','Interior_2','...
        Defect Percentage_2','Defects Multilayer','Multilayer Defect Percentage...
        ');
531 for k=1:tot_num_image
532     if defect_points_image(k)==0
533         image_defect_percent(k)=0;
534     else
535         image_defect_percent(k)=(defect_points_image(k)/...
                interior_points_image(k))*100;
536     end
```

```matlab
537     if defect_points_image2(k)==0
538         image_defect_percent2(k)=0;
539     else
540         image_defect_percent2(k)=(defect_points_image2(k)/...
                interior_points_image2(k))*100;
541     end
542     if defect_points_multilayer(k)==0
543         image_multilayer_percent2(k)=0;
544     else
545         image_multilayer_percent2(k)=(defect_points_multilayer(k)/...
                interior_points_image2(k))*100;
546     end
547     fprintf(fileID,'%7i %9i %10i %20f %9i %10i %20f %9i %20f \r\n',k,...
            defect_points_image(k),interior_points_image(k),...
            image_defect_percent(k),defect_points_image2(k),...
            interior_points_image2(k),image_defect_percent2(k),...
            defect_points_multilayer(k),image_multilayer_percent2(k));
548 end
549
550 interior_point_sum=sum(interior_points_image);
551 defect_point_sum=sum(defect_points_image);
552 total_defects_percentage=(defect_point_sum/interior_point_sum)*100;
553 fprintf(fileID,'\r\n \r\n %24s \n \t %5.2f \n','Total Defect Percentage',...
        total_defects_percentage);
554 fclose(fileID);
```